Sapienza Università di Roma

"Vito Volterra" Doctoral School in Astronomical, Chemical,
Earth, Mathematical and Physical Sciences

PhD Thesis in Earth Sciences

XXXIII Cycle

Frictional, transport properties, and microstructures of simulated basalt faults

Piercarlo Giacomel

A Dissertation in Fault Mechanics

submitted in fulfillment of the

Requirements for the Degree of

Doctor of Philosophy

February 2021

Supervisor:

Prof. Dr. Cristiano Collettini

Dipartimento di Scienze della Terra

Università di Roma "La Sapienza"

P.le Aldo Moro 5, 00185 Roma (Italy)

Co – Supervisors:

Dr. Elena Spagnuolo

Istituto Nazionale di Geofisica e Vulcanologia

Via di Vigna Murata, 605, 00143 Roma (Italy)

Prof. Dr. Giulio Di Toro

Dipartimento di Geoscienze

Università degli Studi di Padova

Via Gradenigo, 6, 35131 Padova (Italy)

Revised by:

Dr. Takehiro Hirose

Kochi Institute for Core Sample Research,

Japan Agency for Marine-Earth Science and Technology

200 Monobe Otsu, Nankoku, Kochi, 783-8502 Japan

Dr. Carolina Giorgetti

Laboratory of Experimental Rock Mechanics (LEMR) -

Civil Engineering Institute (IIC) – School of Architecture,

Civil and Environmental Engineering (ENAC) - EPFL

(École Polytechnique Federale de Lausanne, Switzerland)

GC C1 408 (Bâtiment GC)

Station 18, CH-1015 Lausanne Switzerland

Preface

The main chapters of the dissertation are the result of the partnership between Sapienza University of Rome and INGV (National Institute of Geophysics and Volcanology) Rome.

I collected, analyzed, and interpreted the data and wrote each dissertation chapter under the supervision of Prof. Cristiano Collettini, Dr. Elena Spagnuolo, and Prof. Giulio Di Toro. I performed friction experiments and permeability measurements in cooperation with Dr. Elena Spagnuolo, MSc. Roberta Ruggieri, Dr. Marco M. Scuderi, Dr. Christopher W.A. Harbord, and Dr. Stefano Aretusini.

Chapter 2 is currently under review for the journal Tectonophysics with the following author list and title:

> Giacomel, P., Ruggieri, R., Scuderi, M.M., Spagnuolo, E., Di Toro, G., and Collettini, C. Frictional strength, stability, and healing properties of basalt-built experimental faults.

Chapter 3 has been peer-reviewed and published with the following citation:

> Giacomel, P., Spagnuolo, E., Nazzari, M., Marzoli, A., Passelegue, F., Youbi, N., & Di Toro, G. (2018). Frictional Instabilities and Carbonation of Basalts Triggered by Injection of Pressurized H_2O-and CO_2-Rich Fluids. *Geophysical research letters*, 45(12), 6032-6041.

Chapter 4 contains preliminary results with the following author list:

> Giacomel, P., Spagnuolo E., Scuderi, M.M., Aretusini, S., Harbord, C.W.A., Di Toro, G., and Collettini, C. On the stability of sliding: hydromechanical responses of basalt rock-on-rock contacts to fluid pressure stimulation.

"Where shall I begin, please your Majesty?" he asked.

"Begin at the beginning" the King said, gravely,

"and go on till you come to an end: then stop".

"Alice's Adventures in Wonderland" (1865)

Charles L. Dodgson (Lewis Carroll)

Table of contents

Abstract

Earthquakes induced by anthropic activities are a major concern for the success of the industrial operations associated with in-situ underground wastewater injection, oil and gas withdrawals, geothermal energy exploitation, and geological carbon sequestration. Over the last few decades, basalt rocks have drawn heightened attention from the geo-energy industry and the scientific community because of their widespread occurrence in the oceanic lithosphere and their efficiency to act as carbon sinks, thus contributing to locally reduce the CO_2 anthropogenic emissions. Given the direct implications for earthquake nucleation, propagation, and arrest in basaltic-dominated environments, understanding the frictional, mechanical, and transport properties of basalts-bearing faults and fractures has become of paramount importance.

To gain better insights on the mechanical behavior of basalt-hosted faults, notably the earthquake nucleation phase, friction experiments were performed using the biaxial deformation machine BRAVA and the rotary-shear apparatus SHIVA, both installed at the National Institute of Geophysics and Volcanology (INGV, Rome), Italy. Whereas, to characterize the transport properties of basalt cores and simulated faults, hydraulic transmissivity was measured on the permeameter and before and after friction tests on SHIVA.

Three main scientific topics were addressed using an experimental approach: 1) the frictional strength, stability, and healing properties of basalt-built experimental faults (i.e., simulated gouge and bare rock surfaces) under room-dry and water saturated conditions, by integrating the mechanical data with fault microstructures (Chapter 2); 2) the frictional instabilities and carbonation processes of simulated initially bare rock surfaces with different degree of alteration, triggered by injection of pressurized H_2O, pure CO_2, CO_2- rich water, and Argon (Chapter 3); 3) the hydromechanical properties changes of simulated initially bare rock surfaces and their influence on the fault slip behavior during water pressurization (Chapter 4). The accurate stress paths analysis from rotary-shear tests involving hollow bare rock surfaces in Ch.4 required the development of an experimentally-derived model accounting for the cylindrical geometry of SHIVA samples, that modifies the fluid pressure contribution on the effective normal stress acting on the laboratory fault, (Appendix 1). All the tests were performed at ambient temperature, which may mimic the temperature conditions in low enthalpy geo-energy sites in basalts.

In this dissertation, overall, I demonstrate that the static friction coefficient of basalts is in the range of $\mu \sim 0.6 - 0.8$, at conditions ranging from room-dry to supra-hydrostatic, regardless of the

alteration state of basalts and the fluid chemistry during short-term laboratory experiments (< 60 min). Therefore, basalts are inherently frictionally strong and the high healing rates testify their ability to regain shear strength during the interseismic period. Secondly, I show that fault structure controls their frictional stability: while simulated gouge are more prone to host earthquake nucleation (i.e., velocity weakening behavior) when deformation becomes localized along well-developed shear zones formed in response to cataclasis and gain size reduction, bare rock surfaces show the opposite behavior, transitioning to velocity strengthening behavior promoted by dilatancy processes coupled with gouge production during shearing. Finally, I illustrate that changes in coupled hydromechanical properties during fluid pressurization can dominate over the effects of second-order frictional changes predicted by the rate-and state-friction laws. In this regard, I observed that hydromechanical weakening effects become more pronounced the lower the fault transmissivity. This evidence provides an effective mechanism for inducing fault weakening and ultimately, to bring about earthquake slip also in velocity-strengthening basalt fault patches.

Riassunto

I terremoti indotti dalle attività antropiche costituiscono una discriminante per il successo delle attività industriali quali l'iniezione di acque reflue, l'estrazione di petrolio e gas naturale, lo sfruttamento di energia geotermica e lo stoccaggio geologico di anidride carbonica. Negli ultimi anni, i basalti hanno catturato l'attenzione dell'industria del settore energetico e della comunità scientifica, a causa della loro vasta diffusione nella litosfera oceanica e della loro capacità di mineralizzare la CO_2 "trasformandola in roccia" (New York Times 9/2/2015). Tale proprietà, consente di fatto di sottrarre a lungo termine l'anidride carbonica presente in atmosfera, contribuendo pertanto alla riduzione locale delle emissioni di CO_2 di origine antropogenica. Comprendere le proprietà di attrito, meccaniche e idrologiche di faglie e fratture in basalto ha assunto pertanto un'importanza fondamentale, per le dirette implicazioni riguardanti l'enucleazione dei terremoti, la loro propagazione e l'arresto in ambienti geologici dominati dai basalti.

Per meglio comprendere le proprietà meccaniche di faglie e fratture in basalto, e in particolare la fase di enucleazione dei terremoti, esperimenti di attrito sono stati realizzati mediante l'apparato biassiale BRAVA e l'apparato di tipo rotativo SHIVA, entrambi installati presso l'Istituto Nazionale di Geofisica e Vulcanologia (INGV, Roma). Invece, per caratterizzare le proprietà di trasporto delle carote di basalto e delle faglie sperimentali, la trasmissività idraulica è stata misurata mediante il permeametro, prima e dopo gli esperimenti di attrito su SHIVA.

Sono stati trattati tre principali argomenti seguendo un approccio sperimentale per caratterizzare: 1) le proprietà di resistenza di attrito, stabilità e di healing delle faglie sperimentali in basalto (ovvero, faglie polverizzate e superfici di faglia) in condizioni di umidità atmosferica e in condizioni sature d'acqua, integrando i dati meccanici con quelli microstrutturali (Capitolo 2); 2) le instabilità dell'attrito ed i processi di carbonatazione delle superfici di faglia sperimentali aventi diversi gradi di alterazione, cagionati dall'iniezione di fluidi ricchi in H_2O, CO_2, misture H_2O-CO_2, e Argon (Capitolo 3); 3) le variazioni delle proprietà idromeccaniche delle superfici di faglia sperimentali e la loro influenza sul loro comportamento durante l'iniezione di acqua in pressione (Capitolo 4). Per quanto concerne i cilindri cavi descritti nel capitolo 4, l'analisi accurata dello stato di sforzo negli esperimenti di tipo rotativo, ha richiesto lo sviluppo di un modello basato sui dati sperimentali che tenesse conto della geometria cilindrica dei campioni montati su SHIVA, la quale modifica il modo in cui la pressione di fluido influisce sullo sforzo normale efficace agente sulla faglia (Appendice 1). Tutti i test sono stati realizzati a temperatura ambiente, che può emulare le condizioni di temperatura di un sito energetico a bassa entalpia.

In questa tesi, complessivamente si osservano valori del coefficiente di attrito statico intorno a $\mu \sim 0.6 - 0.8$, a diverse condizioni che spaziano dall'umidità atmosferica a quelle sovra-idrostatiche, indipendentemente dello stato di alterazione dei basalti e della composizione chimica del fluido iniettato durante gli esperimenti a breve termine (< 60 min). Pertanto, le faglie in basalto sono considerate "forti", e gli elevati tassi di healing testimoniano la loro abilità di riguadagnare la resistenza al taglio durante il periodo intersismico. Secondariamente, metto in evidenza come la struttura delle faglie controlli le proprietà di rate and state e la stabilità delle stesse: mentre le polveri sono più propense ad enucleare terremoti (ovvero possiedono un comportamento di indebolimento con l'aumento di velocità: velocity weakening) quando, a seguito di processi cataclastici con riduzione della granulometria, la deformazione diventa localizzata lungo zone di deformazione ben sviluppate, al contrario, le superfici di faglia passano a un comportamento di incremento dell'attrito con l'aumentare della velocità (velocity strengthening), a seguito di processi di dilatanza che accompagnano la produzione di detrito durante lo scivolamento. Infine, si è osservato che i cambiamenti nelle proprietà idromeccaniche durante la pressurizzazione di fluido possono diventare dominanti rispetto agli effetti prodotti dai cambiamenti di attrito di secondo ordine predetti dalle leggi di rate. A tale riguardo, ho rilevato un più pronunciato indebolimento idromeccanico, laddove la trasmissività idraulica della faglia è minore. Questa osservazione fornisce un efficace meccanismo per l'indebolimento delle faglie e in ultima istanza, portare all'enucleazione di terremoti anche nelle porzioni faglie in basalto caratterizzate da un comportamento "velocity strengthening".

1. General introduction

In the last few decades, a numerous number of conventional and unconventional energy technologies have been developed to meet the growing energetic demand and the pressing necessity to mitigate global warming. Many of these methods require the injection/extraction of fluids into in-situ underground formations. It has been long known since the Rangely field-scale fluid injection experiment (*Raleigh*, 1976), that modulating the fluid pressure on faults can control the seismicity rate in a field area. *Townend and Zoback* (2000) demonstrated from deep borehole measurements the critically stressed nature of the Earth's crust, implying that faults are close to reactivation at the current resolved stress levels nearly everywhere within plate interiors (*Zoback and Zoback*, 1989). Therefore, such operations have the potential for inducing seismicity also in stable continental regions of the Earth's brittle crust (e.g., *McGarr et al.*, 2002; *Davies et al.*, 2013; *Ellsworth*, 2013; *Grigoli et al.*, 2017, and references therein). Examples of human-induced earthquakes related to industrial operations are spread worldwide and comprise notable cases such as the enhanced geothermal system (EGS) stimulation in Switzerland (*Haering et al.*, 2008; *Deichmann and Giardini*, 2009), France (*Majer et al.*, 2007), and Korea (*Ellsworth et al.*, 2019; *Lee et al.*, 2019); the wastewater injection sites associated with oil and gas production in the central America (*Keranen et al.*, 2014; *Weingarten et al.*, 2015), Canada (*Atkinson et al.*, 2016; *Bao and Baton*, 2016), and Italy (*Improta et al.*, 2015); the gas extraction in the largest Europe's natural gas field in the Netherlands (*van Thienen-Visser and Breunese*, 2015). Such case studies hosted earthquakes with magnitude (M_w) up to 5.5. Due to the relative abundance of basalts in several areas of the lithospheric crust and their fast reactivity with CO_2-rich water leading to long-term disposal of manmade CO_2 emissions, the exploitation of these mafic rocks from the geo-energy industry has recently become increasingly appealing in the framework of geothermal energy and in-situ carbon sequestration. In fact, basaltic rocks are one of the most common constituents in the brittle crust: ~ 10% of the continental surface area, ~ 70% of the Earth's surface, and the majority of the ocean floor are covered by basalts. Furthermore, some landmasses above sea level in correspondence of mid-ocean ridges are almost entirely made of basalts (e.g., Iceland: ~ 90%) (*Goldberg et al.*, 2008; *McGrail et al.*,

2006). In this region, specifically in the Husmuli area, wastewater reinjection has led to the increase in microseismicity rates, culminating in two seismic episodes of Mw 4 that was widely felt by local population (*Juncu et al.*, 2018). Fault reactivation associated with such geo-energy industrial activities has become a topical issue in the recent years because of *a)* the increasing public concern motivated by the earthquake-related ground shaking that possibly induces structural damage to surface structures and nuisance to the local human communities; and *b)* the integrity and stability of the injection sites potentially causing economic loss and environmental pollution.
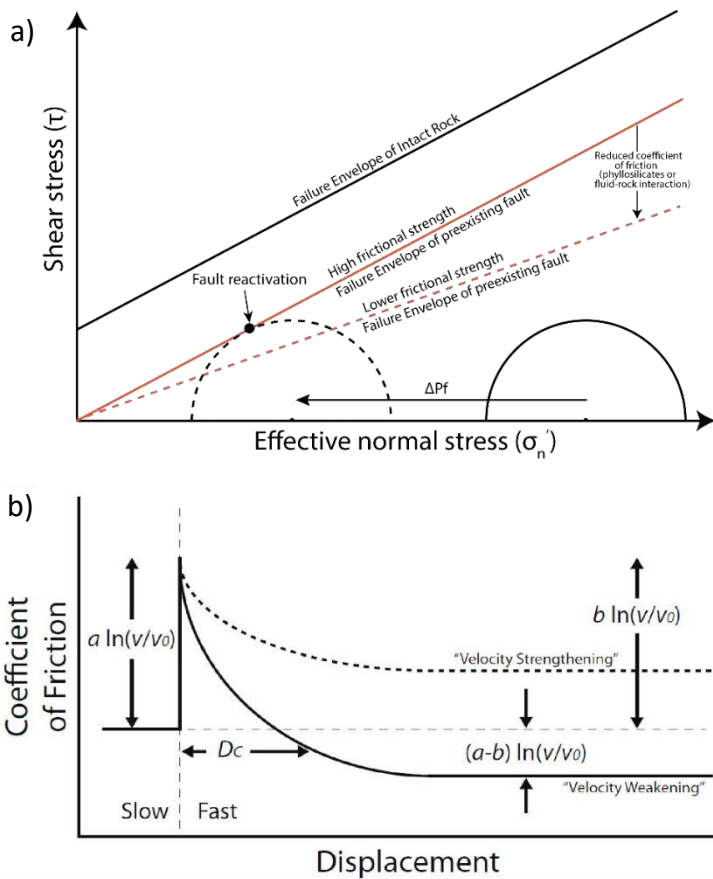
Because of this, fault reactivation and injection-induced seismicity may pose a serious threat for the success of the above industrial operations without a preliminary careful seismic site risk assessment. This requires an in-depth knowledge of the fault slip behavior during fluid pressurization and, in the context of basalt-hosted injection sites, of the structures formed during the emplacement of basaltic lava flows such as cooling joints and fractures, which can act as preexisting weakness planes inside the intact rock and thus affect the nucleation of slip instabilities (*Hutton et al.*, 1994). This is evidenced in structural field studies on exhumed basalt fault zones analogs, like those conducted by *Walker et al.* (2012), that revealed the presence of widespread reactivated joint planes. Columnar (cooling) joints are nearly ubiquitous in subaerial lava flows and typically characterize the dense, impermeable, flow-interior in continental basalt flood sequences that can be therefore selected as potential caprocks for in-situ geo-energy applications (e.g., *Goldberg et al.*, 2010). However, the reactivation of pervasive preexisting jointed units may lead to a rapid fault zone development (*Walker et al.*, 2012), that could undermine the integrity and stability of such caprocks in active volcano-tectonically systems. In these environments, slip instabilities nucleating at shallow depth in volcanic-rich gouge layers are also documented. Clear examples include the Hawaiian (*Delinger and Morgan*, 2014; *Klein et al.*, 1987; *Lockwood et al.*, 1987 among many others) and Etnean (e.g., *Alparone et al.*, 2013; *Azzaro et al.*, 2017; *Branca et al.*, 2011) basaltic volcanoes, where deformation along the flanks and in the summit areas of rift zones and volcanic edifices is accommodated via shallow landslides and/or seismic faulting, often characterized by surface ruptures (e.g., *Villani et al.*, 2020). In some cases, synmagmatic fault zones containing volcanic-rich gouge, such as those formed along

the margins of the volcanic domes (e.g., Mt. Saint Helens: *Iverson et al.*, 2006; *Moore et al.*, 2008), well preserve the primary mineral constituents of the host-rock; whereas in other occurrences these fault zones are intensively altered and/or mineralized (e.g., *Walker et al.*, 2013), or may localize shear at the interface between lava flows and clay-rich deposits (*Groppelli and Tibaldi*, 1999). Therefore, unravelling the mechanical behavior of variably altered (clay-rich) basalts is critical to gain better insights on the shallow earthquakes and landslides occurring in volcano-tectonic environments. Even more so, when deformation is localized within shear zones cutting the flanks of the volcanic edifices, as it is documented that shear zones might also affect densely urbanized areas, with clear implications for their geological hazard.

From a physical point of view, as fluid is injected into underground formations, pore fluid pressure into preexisting fault set will increase, reducing the effective normal stress that holds the fault in place, according to the effective stress law $\sigma'_n = \sigma_n - P_f$ (*Terzaghi*, 1925). It is commonly accepted that injection pressure would raise the fault to reactivation when it meets the Coulomb's criterion:

Eq. (1.1) $$\tau = \mu \, (\sigma_n - Pf)$$

where τ is the fault shear strength, μ the coefficient of friction of the fault, σ_n the normal stress acting on the fault, and P_f is the fluid pressure (*Hubbert and Rubey*, 1959). Eq. (1.1) and Figure 1.1a show that preexisting faults, when optimally oriented (*Sibson*, 1986) reactivate at lower stress levels than those required to bring intact rock to failure. Early laboratory experiments have largely demonstrated that the coefficient of friction is mostly independent on the rock type, with μ in the range of 0.6 - 0.85 (*Byerlee*, 1978). Besides the presence of phyllosilicates, the frictional strength may be also influenced by the fluid-rock interaction causing physicochemical fault weakening. A clear example are the seismic sequences hosted in the Italian Central Apennine area where CO_2 pressurization has reactivated fault zones both due to elevated pore fluid pressures and the frictional weakening of the tectonic faults (*Chiodini et al.*, 2004; *Miller et al.*, 2004; *Collettini et al.*, 2008).

a)

Shear stress (τ)

Failure Envelope of Intact Rock

Reduced coefficient of friction (phyllosilicates or fluid-rock interaction)

High frictional strength
Failure Envelope of preexisting fault

Fault reactivation

Lower frictional strength
Failure Envelope of preexisting fault

ΔPf

Effective normal stress (σ_n')

b)

Coefficient of Friction

$a \ln(v/v_0)$

$b \ln(v/v_0)$

"Velocity Strengthening"

← D_c →

$(a-b) \ln(v/v_0)$

"Velocity Weakening"

Slow | Fast

Displacement

Figure 1.1. (a) Mohr- Coulomb diagram showing the failure envelope necessary to bring intact rock to failure (solid black line) and to reactivate frictionally strong preexisting faults (orange line). The orange dashed line represents the possible reduction in static friction coefficient due to the presence of phyllosilicate/clay minerals that may have replaced primary mineral constituents of basalts and/or the result of fluid-rock interaction during the tests. Injection of pressurized fluids reduces the effective normal stress of the fault by shifting the Mohr circle to the left up to meet the Coulomb's criterion for fault reactivation (*Hubbert and Rubey*, 1959). **(b)** Typical velocity step increases and second-order friction response, with the associated friction constitutive parameters: when a-b < 0, the fault is "velocity weakening", whereas when a-b > 0 the fault is "rate-strengthening".

The Coulomb criterion described in Eq. (1.1) dictates the condition for fault slip but does not address the question of how faults will fail upon fluid pressurization, i.e., the stability of sliding. Fault friction stability is commonly described in the framework of empirically derived rate-and-state friction law (*Dieterich*, 1979; *Ruina*, 1983; *Marone*, 1998). Upon fault reactivation, a second- order friction effect occurs, that determines either an increase or a decrease in friction coefficient μ (Figure 1.1b). If μ increases upon a step increase in velocity, the fault exhibits a velocity strengthening behavior that fosters fault rupture arrest and/or aseismic creep. Conversely, when μ decreases as sliding velocity increases, the fault is velocity weakening and depending on the relationship between the elastic stiffness of the loading medium surrounding the fault and the friction constitutive parameters (*Rice and Ruina*, 1983), it has the potential to nucleate seismic ruptures. In the framework of rate- and state-dependent friction constitutive laws, the propensity of a fault patch to recover frictional strength during the interseismic periods of the seismic cycle can be experimentally quantified through slide- hold-slide experiments via the time dependence of static friction coefficient,

i.e., the healing rate (*Dieterich*, 1972; *Marone and Saffer*, 2015). The healing rate is dependent on processes involving both the growth of asperity contact area (*Dieterich and Kilgore*, 1996) and the quality of frictional contacts (e.g., *Tullis*, 1988; *Li et al.*, 2011). Overall, frictionally strong faults are velocity weakening and characterized by high healing rates, although recent experimental studies have demonstrated that such frictional properties are strongly affected by fault structure heterogeneities (*Carpenter et al.*, 2014; *Tesei et al.*, 2014), with possible implications for seismicity. However, in order to fully capture the fault slip behavior during fluid pressurization and to envision the stress path leading to the onset of dynamic instability, a further issue needs to be addressed, that is to which extent the coupled hydromechanical properties affect fault weakening during fluid pressure stimulations. In fact, at stresses approaching the Coulomb's reactivation envelope, the mechanical effect of fluid pressure can overcome or not second-order variations in μ predicting the friction stability, resulting in the observed fault slip behavior, as recognized at various scales from the laboratory (e.g., *Scuderi et al.*, 2017) to the large field scale (e.g., *Guglielmi et al.*, 2015; *Cappa et al.*, 2019).

Notwithstanding the widespread occurrence of basalts in the Earth's crust, to our knowledge the frictional and transport properties of basalt faults to date have been poorly investigated. This thesis aims to provide better insights on the basalt fault mechanics to mitigate the seismic risk during fluid injection operations, by answering the following questions:

1) How does fault structure affect the frictional strength, stability, and healing properties of basalt faults?

2) To which extent seismic slip events are influenced by fluid-rock interaction during fluid pressurization, hence by the geochemical composition of the injected fluid and the degree of alteration of basalt-hosted faults?

3) How does the coupled hydromechanical evolution control the fault slip behavior during fluid pressurization?

Each question has been addressed separately in the three main chapters of this thesis in which I present my own research developed during the PhD. Friction experiments were carried out on the BRAVA (Chapter 2) and SHIVA apparatuses (Chapters 2, 3, 4), hosted at the High Pressure – High Temperature laboratory of INGV-Rome (Italy). Transport properties of both basalt cores and laboratory faults were quantified using the permeameter and before and at the end of SHIVA tests (Chapter 4).

In chapter 2, I investigate the role of basalt fault structure, defined by simulated fault gouge and bare rock surfaces, on the physical properties of slip within a volume of wear debris material and along sharp joint planes. Here I study the frictional strength, stability, and healing properties for the single cases, by integrating mechanical data with microstructural data. Frictional properties were examined at room-dry and water saturated conditions for normal stresses between 5 to 30 MPa, slip velocities from 0.1 to 300 μm/s (velocity step tests), and hold times from 30 to 3000 s (slide-hold-slide tests).

In chapter 3, I perform unconventional creep experiments at normal stresses from 10 to 20 MPa and constant shear stress of 5 MPa to better illuminate the onset of dynamic frictional instabilities when basalt surfaces with different degree of alteration are brought into contact and interact with fluid of different geochemical composition (i.e., distilled water, pure CO_2, CO_2-rich water, and Argon), at pressure conditions from sub-hydrostatic to supra-hydrostatic. In this study post-tested slipping surface and collected water were subjected to microanalytical and geochemical analysis, respectively, to capture any possible effect from the fluid-fault interaction throughout the tests.

In chapter 4, I conducted unconventional creep experiments at constant shear stress on two nearly critically stressed simulated fault types (~ 85 % of peak shear strength), defined by unaltered initially-bare, basalt surfaces that differ in starting hydraulic properties and accumulated displacement (4mm Vs. 50 mm). Faults were preloaded at normal stresses of ~ 11 MPa and pressurized with distilled water at sub-hydrostatic conditions. During the fluid

pressure stepwise increases of ΔP_f = 0.2 MPa/300 s, the coupled hydromechanical behavior is monitored to gain insights on the fault slip behavior associated with fluid pressurization. Pertaining to Chapters 3 and 4, in Appendix 1 I thoroughly describe the experimentally-derived geometrical model employed to correct the contribution of the fluid pressure on the effective normal stress, accounting for the cylindrical geometry and size of the hollow pair samples mounted on SHIVA. Specifically, I show the resolved stress state on the Mohr-Coulomb diagram before and after the geometrical correction, at pore fluid factors from subhydrostatic to suprahydrostatic regimes, and at dry-vacuum conditions as a benchmark.

REFERENCES

Alparone, S., Cocina, O., Gambino, S., Mostaccio, A., Spampinato, S., Tuvè, T., & Ursino, A. (2013). Seismological features of the Pernicana–Provenzana Fault System (Mt. Etna, Italy) and implications for the dynamics of northeastern flank of the volcano. *Journal of volcanology and geothermal research*, *251*, 16-26.

Atkinson, G. M., Eaton, D. W., Ghofrani, H., Walker, D., Cheadle, B., Schultz, R., ... & Liu, Y. (2016). Hydraulic fracturing and seismicity in the Western Canada Sedimentary Basin. *Seismological research letters*, *87*(3), 631-647.

Azzaro, R., G. Barberi, S. D'Amico, B. Pace, L. Peruzza, and T. Tuvè (2017), When probabilistic seismic hazard climbs volcanoes: the Mt. Etna case, Italy – Part 1: Model components for sources parameterization, *Nat. Hazards Earth Syst. Sci.*, *17*(11), 1981-1998, doi:10.5194/nhess-17-1981-2017.

Bao, X., & Eaton, D. W. (2016). Fault activation by hydraulic fracturing in western Canada. *Science*, *354*(6318), 1406-1409.

Branca, S., M. Coltelli, and G. Groppelli (2011), Geological evolution of a complex basaltic stratovolcano: Mount Etna, Italy, *Italian Journal of Geosciences*, *130*(3), 306-317.

Byerlee, J. (1978). Friction of rocks. In *Rock friction and earthquake prediction* (pp. 615-626). Birkhäuser, Basel.

Cappa, F., Scuderi, M. M., Collettini, C., Guglielmi, Y., & Avouac, J. P. (2019). Stabilization of fault slip by fluid injection in the laboratory and in situ. *Science advances*, *5*(3), eaau4065.

Carpenter, B. M., Scuderi, M. M., Collettini, C., & Marone, C. (2014). Frictional heterogeneities on carbonate-bearing normal faults: Insights from the Monte Maggio Fault, Italy. *Journal of Geophysical Research: Solid Earth*, *119*(12), 9062-9076.

Chiodini, G., Cardellini, C., Amato, A., Boschi, E., Caliro, S., Frondini, F., & Ventura, G. (2004). Carbon dioxide Earth degassing and seismogenesis in central and southern Italy. *Geophysical Research Letters*, *31*(7).

Collettini, C., Cardellini, C., Chiodini, G., De Paola, N., Holdsworth, R.E., Smith, S. A.F., 2008. Fault weakening due to CO2 degassing in the Northern Apennines: short and long-term processes. Geological Society, London, Special Publications 299, 175–194.

Davies, R., Foulger, G., Bindley, A., & Styles, P. (2013). Induced seismicity and hydraulic fracturing for the recovery of hydrocarbons. Marine and Petroleum Geology, 45, 171–185. https://doi.org/10.1016/j.marpetgeo.2013.03.016

Deichmann, N., and D. Giardini (2009), Earthquakes induced by the stimulation of an enhanced geothermal system below Basel (Switzerland), *Seismol. Res. Lett.*, *80*(5), 784–798.

Denlinger, R. P., & Morgan, J. K. (2014). *Instability of Hawaiian volcanoes: Chapter 4 in Characteristics of Hawaiian volcanoes* (No. 1801-4, pp. 149-176). US Geological Survey.

Dieterich, J. H. (1972). Time-dependent friction in rocks. *Journal of Geophysical Research*, *77*(20), 3690-3697.

Dieterich, J. H. (1979). Modeling of rock friction: 1. Experimental results and constitutive equations. *Journal of Geophysical*

Research: Solid Earth, *84*(B5), 2161-2168.

Dieterich, J. H., & Kilgore, B. D. (1996). Imaging surface contacts: power law contact distributions and contact stresses in quartz, calcite, glass and acrylic plastic. *Tectonophysics*, *256*(1-4), 219-239.

Ellsworth, W. L. (2013). Injection-induced earthquakes. *Science*, *341*(6142).

Ellsworth, W. L., Giardini, D., Townend, J., Ge, S., & Shimamoto, T. (2019). Triggering of the Pohang, Korea, earthquake (M w 5.5) by enhanced geothermal system stimulation. *Seismological Research Letters*, *90*(5), 1844-1858.

Goldberg, D. S., Takahashi, T., & Slagle, A. L. (2008). Carbon dioxide sequestration in deep-sea basalt. *Proceedings of the National Academy of Sciences*, *105*(29), 9920-9925.

Grigoli, F., Cesca, S., Priolo, E., Rinaldi, A. P., Clinton, J. F., Stabile, T. A., ... & Dahm, T. (2017). Current challenges in monitoring, discrimination, and management of induced seismicity related to underground industrial activities: A European perspective. *Reviews of Geophysics*, *55*(2), 310-340.

Groppelli, G., & Tibaldi, A. (1999). Control of rock rheology on deformation style and slip-rate along the active Pernicana Fault, Mt. Etna, Italy. *Tectonophysics*, *305*(4), 521-537.

Guglielmi, Y., Cappa, F., Avouac, J. P., Henry, P., & Elsworth, D. (2015). Seismicity triggered by fluid injection–induced aseismic slip. *Science*, *348*(6240), 1224-1226.

Hatton, C.G., Main, I.G., and Meredith, P.G., 1994, Non-universal scaling of fracture length and opening displacement: Nature, v. 367, p. 160–162, doi:10.1038/367160a0.

Haering, M., U. Schanz, F. Ladner, and B. C. Dyer (2008), Characterization of the Basel 1 geothermal system, *Geothermics*, *37*, 469–495, doi:10.1016/j.geothermics.2008.06.002

Hubbert, M. K., & Rubey, W. W. (1959). Role of fluid pressure in mechanics of overthrust faulting I. Mechanics of fluid-filled porous solids and its application to overthrust faulting. *Geological Society of America Bulletin*, *70*(2), 115–166.

Improta, L., Valoroso, L., Piccinini, D., & Chiarabba, C. (2015). A detailed analysis of wastewater-induced seismicity in the Val d'Agri oil field (Italy). *Geophysical Research Letters*, *42*(8), 2682-2690.

Iverson, R. M., Dzurisin, D., Gardner, C. A., Gerlach, T. M., LaHusen, R. G., Lisowski, M., ... & Vallance, J. W. (2006). Dynamics of seismogenic volcanic extrusion at Mount St Helens in 2004–05. *Nature*, *444*(7118), 439-443.

Juncu, D., Árnadóttir, T., Geirsson, H., Guðmundsson, G. B., Lund, B., Gunnarsson, G., ... & Michalczewska, K. (2020). Injection-induced surface deformation and seismicity at the Hellisheidi geothermal field, Iceland. *Journal of Volcanology and Geothermal Research*, *391*, 106337.

Keranen, K. M., Weingarten, M., Abers, G. A., Bekins, B. A., & Ge, S. (2014). Sharp increase in central Oklahoma seismicity since 2008 induced by massive wastewater injection. *Science*, *345*(6195), 448-451.

Klein, F. W., Koyanagi, R. Y., Nakata, J. S., & Tanigawa, W. R. (1987). The seismicity of Kilauea's magma system. *Volcanism in Hawaii*, *2*, 1019-1185.

Lee, K. K., Ellsworth, W. L., Giardini, D., Townend, J., Ge, S., Shimamoto, T., ... & Chang, C. (2019). Managing injection-induced seismic risks. *Science*, *364*(6442), 730-732.

Li, Q., T. E. Tullis, D. Goldsby, and R. W. Carpick (2011), Frictional ageing from interfacial bonding and the origins of rate and state friction, *Nature*, 480, 233– 236, doi:10.1038/nature10589.

Lockwood, J. P., J. J. Dvorak, T. T. English, R. Y. Koyanagi, A. T. Okamura, M. L. Summers, and W. R. Tanigawa (1987), Mauna-Loa 1974–1984: A decade of intrusive and extrusive activity, in Volcanism in Hawaii, U. S. Geol. Surv. Prof. Pap., 1350, 537– 570.

Majer, E. L., Baria, R., Stark, M., Oates, S., Bommer, J., Smith, B., & Asanuma, H. (2007). Induced seismicity associated with enhanced geothermal systems. *Geothermics*, *36*(3), 185-222.

Marone, C. (1998). Laboratory-derived friction laws and their application to seismic faulting. *Annual Review of Earth and Planetary Sciences*, *26*(1), 643-696.

Marone, C., & Saffer, D. M. (2015). The mechanics of frictional healing and slip instability during the seismic cycle. In *Earthquake Seismology* (pp. 111-138). Elsevier Inc.

McGarr, A., Simpson, D., Seeber, L., & Lee, W. (2002). Case histories of induced and triggered seismicity. *International Geophysics Series*, *81*(A), 647-664.

McGrail, B. P., Schaef, H. T., Ho, A. M., Chien, Y. J., Dooley, J. J., & Davidson, C. L. (2006). Potential for carbon dioxide sequestration in flood basalts. *Journal of Geophysical Research: Solid Earth*, *111*(B12).

Miller, S. A., Collettini, C., Chiaraluce, L., Cocco, M., Barchi, M., & Kaus, B. J. (2004). Aftershocks driven by a high-pressure CO 2 source at depth. *Nature*, *427*(6976), 724-727.

Moore, P., N. R. Iverson, and R. M. Iverson (2008), Frictional properties of the Mount St. Helens gouge, *A Volcano Rekindled: The Renewed Eruption of Mount St. Helens, 2004-2006*, *1750*, 415-424.

Raleigh, C. B., Healy, J. H., & Bredehoeft, J. D. (1976). An experiment in earthquake control at Rangely, Colorado. *Science*, *191*(4233), 1230-1237.

Rice, J. R., & Ruina, A. L. (1983). Stability of steady frictional slipping.

Ruina, A. (1983). Slip instability and state variable friction laws. *Journal of Geophysical Research: Solid Earth*, *88*(B12), 10359-10370.

Rutter, E., & Hackston, A. (2017). On the effective stress law for rock-on-rock frictional sliding, and fault slip triggered by means of fluid injection. *Philosophical Transactions of the Royal Society A: Mathematical, Physical and Engineering Sciences*, *375*(2103), 20160001.

Scuderi, M. M., Collettini, C., & Marone, C. (2017). Frictional stability and earthquake triggering during fluid pressure stimulation of an experimental fault. *Earth and Planetary Science Letters*, *477*, 84-96.

Sibson, R.H., 1986. Earthquakes and rock deformation in crustal fault zones. Annu. Rev. Earth Planet. Sci.14, 149–175. http://dx.doi.org/10.1146/annurev.ea.14.050186.001053

Terzaghi, K. (1925). Erdbaumechanik auf bodenphysikalischer Grundlage.

Tesei, T., Collettini, C., Barchi, M. R., Carpenter, B. M., & Di Stefano, G. (2014). Heterogeneous strength and fault zone complexity of carbonate-bearing thrusts with possible implications for seismicity. *Earth and Planetary Science Letters*, *408*, 307-318.

Tullis, T. E. (1988), Rock friction constitutive behavior from laboratory experiments and its implications for an earthquake prediction field monitoring program, *Pure Appl. Geophys.*, 126, 555– 588.

van Thienen-Visser, K., & Breunese, J. N. (2015). Induced seismicity of the Groningen gas field: History and recent developments. *The Leading Edge*, *34*(6), 664-671.

Villani, F., Pucci, S., Azzaro, R. *et al.* Surface ruptures database related to the 26 December 2018, Mᴡ 4.9 Mt. Etna earthquake, southern Italy. *Sci Data* **7,** 42 (2020). https://doi.org/10.1038/s41597-020-0383-0.

Walker, R. J., R. E. Holdsworth, P. J. Armitage, and D. R. Faulkner (2013), Fault zone permeability structure evolution in basalts, *Geology*, *41*(1), 59-62, doi:10.1130/g33508.1.

Walker, R., R. Holdsworth, J. Imber, and D. Ellis (2012), Fault-zone evolution in layered basalt sequences: A case study from the Faroe Islands, NE Atlantic margin, *Geological Society of America Bulletin*, *124*, 1382-1393, doi:10.1130/B30512.1.Townend, J., & Zoback, M. D. (2000). How faulting keeps the crust strong. *Geology*, *28*(5), 399-402.

Weingarten, M., Ge, S., Godt, J. W., Bekins, B. A., & Rubinstein, J. L. (2015). High-rate injection is associated with the increase in US mid-continent seismicity. *Science*, *348*(6241), 1336-1340.

Zoback, M. L., & Zoback, M. D. (1989). Tectonic stress field of the continental United States. *Geophysical framework of the continental United States: Geological Society of America Memoir*, *172*, 523-539.

2. Frictional strength, stability, and healing properties of basalt-built experimental faults

Piercarlo Giacomel[1], Roberta Ruggieri[1], Marco M. Scuderi[1], Elena Spagnuolo[2], Giulio Di Toro[2,3], and Cristiano Collettini[1,2]

[1] Dipartimento di Scienze della Terra, Sapienza Università di Roma, Piaz. Aldo Moro 5, Rome

[2] Istituto Nazionale di Geofisica e Vulcanologia, Via di Vigna Murata 605, Rome, Italy

[3] Dipartimento di Geoscienze, Università degli Studi di Padova, Via G. Gradenigo 6, Padua, Italy

AUTHOR CONTRIBUTIONS

PG wrote the first version of the manuscript. CC, PG, ES, MMS, GDT conceived the idea of the experiments. PG performed the petrophysical and microstructural analyses. RR, MMS, PG, ES performed the experiments. All the authors analyzed the mechanical and microstructural data and contributed to the final version of the manuscript.

ABSTRACT

We performed a suite of experiments aimed at examining the frictional properties of unaltered basalts at conditions considered to be representative of slip at shallow depths in volcano-tectonic environments and in-situ geo-energy basaltic sites. Scientific drilling and field studies on exhumed subsurface faults and fractures analogues suggest that, frictional sliding in basalts can occur in shear zones within a volume of wear debris or along localized joint planes. To illuminate how structural heterogeneities effect the nucleation of slip instabilities into basalts, we sheared simulated fault gouge and bare rock surfaces at low normal stresses (4 to 30 MPa) at ambient temperature, under room-dry and wet conditions. We ran velocity steps (0.1-300 μm/s) and slide-hold-slides (30-3000 s holds) to determine the frictional stability and healing properties of basalts. In all the tests, we observed high friction coefficient associated with important frictional re-strengthening. Overall, our results show that structural heterogeneities strongly affect the friction velocity dependence of basalts: while with increasing normal stress, shear localization accompanied by cataclasis and grain size reduction favors the transition to velocity weakening behavior of powdered samples, on bare surfaces gouge production with accumulated displacement promotes a transition to a velocity strengthening behavior. Our results imply that at the tested conditions, friction instabilities may promptly nucleate in shear zones where deformation within (unaltered) basaltic gouge layers is localized, such as those located along volcanic flanks and beneath the edifices, while joint planes characterized by rough rock-on-rock contacts are less prone to unstable slip, which is quenched at higher slip velocities.

2.1 INTRODUCTION

The frictional properties of fault rocks are expected to exert a primary control on fault slip behavior (*Brace and Byerlee*, 1966). Multiple data sources support the frictionally strong nature of a broad gamut of seismically active faults, with the static coefficient of Coulomb friction µ in the range 0.6-0.85 (e.g., *Byerlee*, 1978; *Collettini and Sibson*, 2001*; Scholz*, 2000) and high frictional healing values, which allow the rapid recovery of shear strength required for repeated fault reactivations (*Carpenter et al.*, 2014; *Marone*, 1998b). However, several lines of evidence suggest that fault frictional and structural heterogeneities may result in complex slip behavior (e.g., *Ben-Zion*, 2001; *Boatwright and Cocco*, 1996; *Collettini et al.*, 2019; *Di Stefano et al.*, 2011; *Kaneko et al.*, 2010; *Niemeijer and Vissers*, 2014, and many others), which can be captured by variations in rate and state friction constitutive parameters.

In the last few decades, the seismic and landslide hazard potential related to volcano-tectonic environments have raised the burning necessity to delve into the mechanisms of slip instability nucleation into basalts also at shallow depths. Reported examples of active volcano-tectonics include the Kilauea and Mauna Loa basaltic volcanoes in Hawaii, where rates of shear failures are mainly controlled by local stress changes associated to magmatic intrusions or eruptive activities (e.g., *Aki and Ferrazzini*, 2001): here the observed shallow Mw ≤ 3 seismicity clustered at 0 -2 km bgl (below ground level) beneath the summit calderas and along the rift zones (*Klein et al.*, 1987; *Klein*, 2016; *Lin and Okubo*, 2020; *Lengliné et al.,* 2008; *Lockwood et al.*, 1987). Submarine evidence and seismic surveys have also found the presence of sand-sized debris where deformation was accommodated via shallow landslides cutting the Hawaiian volcano flanks. Some of these deposits are mainly derived from fragmented lava flows, which are considered the dominant rock type in the upper first km of the Mauna Loa's submarine slope section (*Denlinger and Morgan*, 2014; *Garcia and Davis*, 2001). Striking similarities characterize other active volcano-tectonic settings, such as the Mt. Etna basaltic stratovolcano in Italy, where many of the shallow earthquakes nucleate and/or propagate in basaltic lava flows located beneath the central summit area and along the eastern flank of the volcano (*Azzaro et al.*, 2017; *Branca et al.*, 2011; *Villani et al.*, 2020). The latter represents a

relevant source of hazard since it also encompasses a densely urbanized area (*Azzaro et al.*, 2013). A clear evidence of fault reactivations along the eastern flank is the shallow seismogenic layer located between the ground surface and 5 km depth along the Pernicana-Provenzana Fault system, that enucleated up to Mw 4.2 subsurface earthquakes in basalts during the 1981-1988 seismic sequence (*Alparone et al.*, 2013; *Azzaro et al.*, 2017). Although it is not uncommon that synmagmatic fault zones can present pervasive alteration (i.e., smectites) and mineralization (i.e., calcite and zeolite) of the primary basaltic fault gouge mineralogy (*Khodayar and Einarsson*, 2002; *Kristmannsdóttir*, 1979; *Reidel et al.*, 2013; *Walker et al.*, 2012, 2013a, 2013b), in some cases shear zones are localized in unaltered volcanic fault gouge. A good example is represented by the plagioclase-rich wear debris formed along the margins of the Mount St. Helens lava domes, in response to persistent stick-slip events at < 1 km depth coupled with volcanic extrusion (*Iverson et al.*, 2006; *Moore et al.*, 2008).

Understanding the frictional behavior of unaltered basalt bare surfaces is of strategic importance in basalt-hosted geo-reservoirs and/or caprocks for the safe in-situ carbon geological sequestration or for the reinjection of wastewater byproducts from geothermal power plants. In some of the selected regions, such as the Wallula Basalt Sequestration and the CarbFix pilot projects (*Gislason et al.*, 2010; *Kelemen et al.*, 2019; *McGrail et al.*, 2011; *Snæbjörnsdóttir et al.*, 2020), the majority of basalts are low-altered and far from the local high-temperature geothermal systems, so that temperature reaches up to 35°C in the main target aquifers, located respectively at ~ 800 m and 500 m depth (*Alfredsson et al.*, 2013; *McGrail et al.*, 2006). Furthermore, basaltic lava flows capping a storage reservoir normally exhibit cooling columnar joints and (micro) fractures that can potentially affect the integrity and stability of the fluid repositories (e.g., *Goldberg et al.*, 2010). As a matter of fact, pervasive preexisting joint sets can act as preexisting weakness planes inside the intact rock and consequently be reactivated during fluid injection in tectonically active areas (*Hatton et al.*, 1994). Outcrop studies conducted by *Walker et al.* (2012, 2013b) on exhumed subsurface (0 - 3 km bgl) faults and fractures within continental flood basalts, confirmed the occurrence of reactivated unaltered basalt joints, leading to fault-zone development and possibly seismicity.

To date, although a concerted effort has been done to characterize the frictional properties of intrusive rocks like gabbros (*Cox*, 1990; *He et al.*, 2006, 2007; *Marone and Cox*, 1994; *Mitchell et al.*, 2015), friction stability data on its extrusive counterpart (i.e., basalts) are still limited. To our knowledge, measurements of the friction velocity dependence of basalts were carried out by *Zhang et al.* (2017) on unaltered basalt gouge having a particle size, Φ, < 74 μm, at effective normal stress, σ'_n, of 45 – 51 MPa under hydrothermal conditions, and by *Ikari et al.* (2020), on both altered basalt gouge with Φ < 125 μm and bare surfaces finished with #60-grit, at room temperature and σ'_n = 25 MPa.

In order to investigate the possible modes of slip that may arise from differences in fault structures, we investigated the frictional properties and the friction velocity dependence of unaltered basalts simulating deformation along localized rough joint planes, i.e., bare rock surfaces, and shear zones containing fault gouge, i.e., powdered material. The results presented in this study, obtained under low normal stresses (≤ 30 MPa), room-dry and water-saturated conditions at ambient temperature, allow to fill a knowledge gap found in the literature and carry important implications for *(i)* the refinement of local seismic and landslide hazard evaluation in volcanic flanks and edifices and *(ii)* the integrity and stability of basalt-hosted geo-energy sites.

2.2 MATERIALS AND METHODS

Selected specimens are low porosity trachybasalts from Mount Etna (Italy), with an initial density of 2980 ± 10 kg/m^3 and a connected porosity of ~ 6%, measured with the Helium pycnometer Accu Pyc II 1340 installed at the Istituto Nazionale of Geofisica and Vulcanologia (INGV) in Rome (Italy). Bulk-rock chemical and mineralogical analysis were performed using X-ray fluorescence (XRF) and X-Ray powder diffraction (XRPD) at the laboratories located at the Geoscience Department of Padua University and are reported in Supplementary Figures S2.1 and S2.2. Etnean basalts are typical lava flow basalts with a porphyric texture (Figure S2.3, Suppl. Mat.) with phenocrysts showing no discernable preferred alignment. The primary minerals consisted in mm-sized phenocrysts of olivine, clinopyroxene (augite), plagioclase and Fe-Ti oxides, in a completely crystallized groundmass (~ 60% vol on average) with the same mineralogy. The heterogenous spatial distribution of the phenocrysts in basaltic lava flows explains the variable percentage of phenocrystals among different specimens. The relative abundance of the olivine, plagioclase, and pyroxenes, which are the most efficient sources of divalent cations for mineral carbonation, renders Etnean basalts also a suitable natural analogue for CO_2 sequestration into basaltic rocks (e.g., *Kelemen et al. 2019*).

2.2.1 Biaxial deformation experiments

To simulate natural fault gouges, intact fragments of the starting protolith were crushed in a disk mill and hand-sieved to get powders with a grain size < 125 μm. The grain size fraction of starting basalt revealed a high concentration of fine material resulting in about 50% of the volume characterized by a particle size < 20 μm (Figure S2.4, Suppl. Mat.). To simulate fault planes, basalt slabs were carefully cut to produce samples of 4X4 cm^2 nominal area and approximately 0.8 – 1.2 mm thick. In this arrangement the bare surfaces were polished flat with a precision grinder better than 0.1 mm and then hand roughened with #80 grit SiC abrasive powder and water on a glass plate.

We performed laboratory friction experiments in a servo-controlled biaxial deformation apparatus, BRAVA (Brittle Rock deformAtion Versatile Apparatus; *Collettini et al.*, 2014), hosted at the HP-HT Laboratory of the INGV in Rome, Italy. The apparatus is equipped with a fast-acting hydraulic servo-controlled ram that was used to apply and maintain constant normal stress (σ_n) on the simulated fault zone via a load-feedback loop control system. Likewise, a servo-controlled vertical ram was used to apply shear stress (τ). The vertical piston was controlled in displacement-feedback mode, in which the ram was advanced at a constant displacement rate. Applied forces were measured using load cells with 0.03 kN resolution over a maximum force of 1.5 MN, that are calibrated regularly. Displacements were measured to ± 0.1 μm via Linear Variable Displacement Transfomers (LVDTs) throughout the experiments. Load point displacement measurements were corrected for the stiffness of the apparatus, with nominal values of 386.12 kN/mm for the horizontal frame and of 359.75 kN/mm for the vertical frame.

We used the double direct-shear configuration to perform experiments on fault gouge (Figure 2.1b). This experimental configuration consists of two parallel layers of simulated fault gouge placed in between three grooved steel blocks. The grooves are 0.8 mm in height and spaced 1 mm and they ensure shear localization within the fault gouge. For each experiment, the two gouge layers were produced using leveling jigs to obtain a uniform layer thickness of 5 mm before the samples were loaded. These layers have a 5X5 cm^2 nominal area that was kept constant throughout the experiment. For data reproducibility, gouge layers were weighted after sample preparation. This procedure guaranteed similar porosity and a variability < 6% in the material density at the beginning of each test. During each test, σ_n is maintained constant at 5-10-20-30 MPa. For each of these normal stresses, experiments were conducted under both room-dry and water- saturated conditions. Saturation was accomplished by placing the sample assembly in an impermeable plastic membrane filled with deionized water at the beginning of the tests.
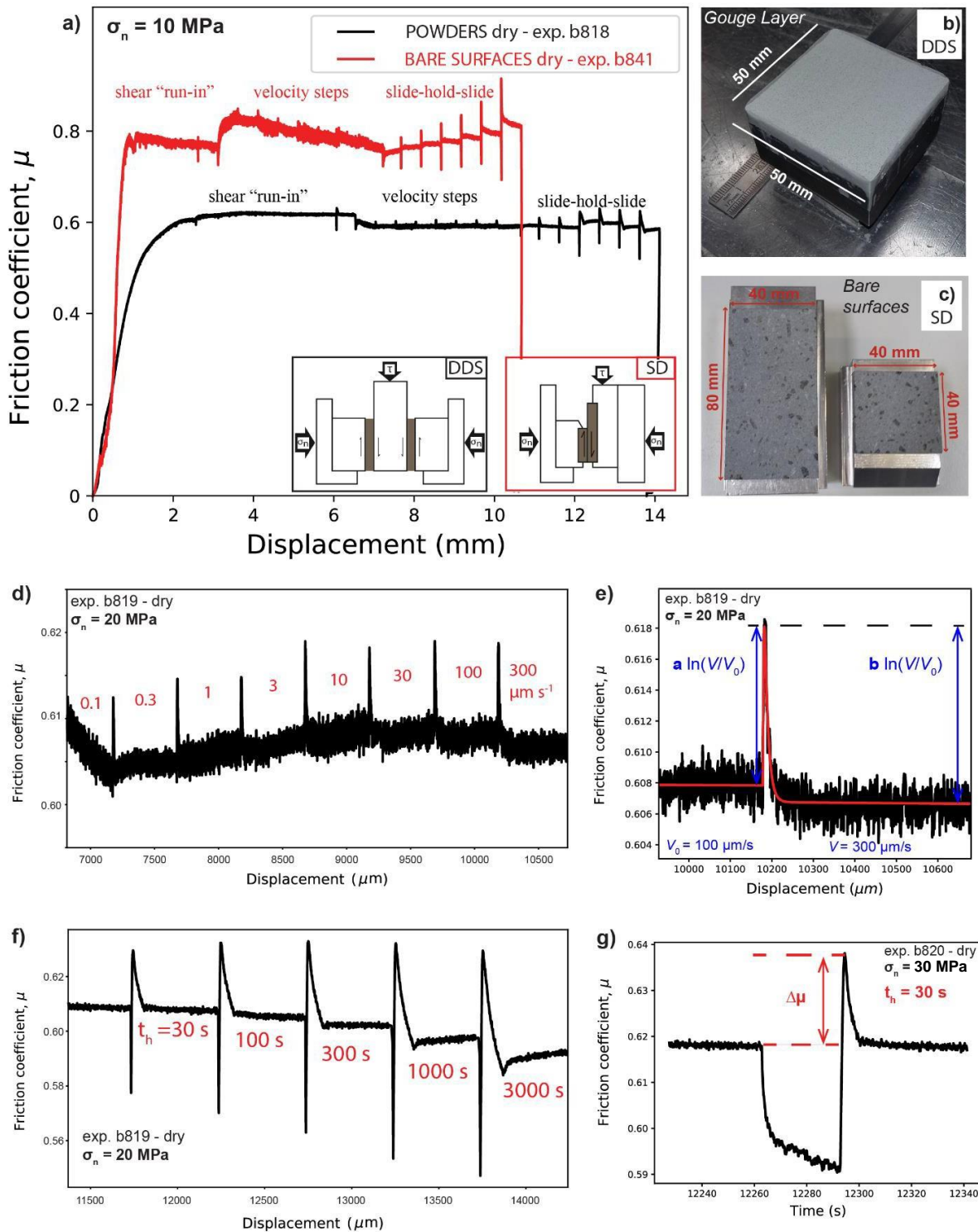
Figure 2.1. (a) Friction Vs. displacement curves retrieved from two typical direct shear experiments involving simulated fault gouge (black line) and bare surfaces (red line). **(b)** Double direct shear, DDS, configuration for the simulated fault gouge and the single direct, SD, shear configuration for bare rock surfaces **(c)**. The "shear run-in" phase is conceived to attain a steady state friction condition and precedes the velocity step and slide-hold-hold sequences. **(d)** Friction vs. displacement for a representative velocity step sequence. **(e)** Enlargement of a 100-300 μm/s velocity step modeled with a fifth order Runge Kutta numerical integration. The "direct effect" a scales as the sudden change in friction upon the velocity upstep and the "evolution effect" b scales as the subsequent decay in friction towards a new steady state value. **(f)** Friction vs. displacement for a representative slide-hold-slide sequence. **(g)** Friction vs. time for a 30 s hold. Frictional healing Δμ is measured as the difference between peak friction value upon reshear and the pre-hold steady state friction.

To study the frictional properties of bare rock surfaces, experiments were designed in unconfined single-direct shear configuration, in which two blocks were juxtaposed to simulate a fault plane (Figure 2.1c). In this experimental geometry, the sliding area of 16 cm^2 was also kept constant during the test. Due to limited tensile strength of the unconfined basalt blocks in single-direct shear configuration, tests on bare rock surfaces were conducted up to 10 MPa normal stress.

The experimental procedure is common for both the configurations and consists in initially applying a normal stress of 1 MPa and let the sample compact. For wet experiments, samples were allowed to saturate for 30-40 min with deionized water. Subsequently, normal stress was increased stepwise to the target values and the sample compaction monitored, until the achievement of a steady state value of horizontal shortening, usually reached after 30-40 min. At this point the vertical ram was advanced at a constant displacement rate of 10 µm/s to apply shear stress and induce shear deformation. We waited until a steady state frictional strength was achieved, which for gouges requires a displacement of 6-7 mm and for bare surfaces 3 mm. This procedure was meant to develop steady-state shear fabric (e.g. *Haines et al.*, 2013) within the gouge layer, and to produce a relatively uniform surface roughness for bare surface experiments. The coefficient of stable sliding friction (μ_{ss}) at steady state was then computed as the ratio between the vertical force and the horizontal force applied by their respective rams, and assuming no cohesion (Table S2.1, Suppl. Mat.). In double-direct shear configuration, the vertical load was halved to average the friction coefficient within the two gouge layers.

Following the achievement of steady-state friction, two distinct types of tests were performed: velocity stepping tests are designed to investigate the velocity dependence of friction, thus the frictional constitutive behavior to infer fault slip stability, and slide-hold-slide (SHS) tests to measure time dependent frictional re-strengthening (Figure 2.1a; Table S2.1).

During velocity stepping tests, we imposed a series of computer-controlled velocity step increases in the following sequence, 0.1 – 0.3 – 1 – 3 - 10 – 30 – 100 – 300 µm s^{-1} with

a constant displacement of 500 µm at each step. Each velocity step consisted in a quasi-instantaneous step increase in sliding velocity from V_0 to V and the new sliding velocity was kept constant until a new steady state condition was attained (Figure 2.1d).

To investigate the velocity dependence of friction, we modelled the collected data from each velocity step   following the Dieterich's time-dependent formulation of the rate-and-state friction constitutive law (*Dieterich*, 1979; *Marone*, 1998b), coupled with the slip evolution law proposed by *Ruina* (1983) as a description of the state evolution:

Eq. (2.1)
$$\mu = \mu_0 + a \ln\frac{V}{V_0} + b_1 \ln\frac{V_0\,\theta_1}{D_{c1}} + b_2 \ln\frac{V_0\,\theta_2}{D_{c2}}$$

Eq. (2.2)
$$\frac{d\theta}{dt} = -\frac{V\,\theta_i}{D_{ci}} \ln\left(\frac{V\theta_i}{D_{ci}}\right), \text{i} =1,2 \quad \text{Ruina's "slip" law}$$

where μ_0 represents the reference steady-state friction at the initial slip velocity V_0, a, b_1 and b_2 are empirically derived constants (dimensionless) termed direct and evolution effect, respectively, θ_1 and θ_2 are the state variable with units of time, D_{c1} and D_{c2} are the critical slip distances over which the state variables evolve to a new steady-state value following the velocity step (e.g., *Marone*, 1998b).

To model our data, we simultaneously solved Eq. (2.1) and (2.2) using a fifth order Runge Kutta numerical integration technique, with the time derivative of a one-dimensional elastic system as a constraint (Eq. (2.3), which accounts for the finite stiffness of the testing apparatus and its elastic interaction with the frictional surface/gouge layers:

Eq. (2.3)
$$\frac{d\mu}{dt} = k\,(V_{lp} - V)$$

where V_{lp} is the load point velocity and k is the elastic loading stiffness of our experimental apparatus and the experimental fault, normalized by the normal stress (given in units of coefficient of friction per displacement). We then determined the constitutive parameters a, b, and Dc as in Figure 2.1e, by fitting our data from velocity step tests using an inverse modelling technique (e.g., *Blanpied et al.*, 1998a; *Reinen and Weeks*, 1993; *Saffer and Marone*,

2003). This technique also includes removing the slip-dependent linear trends in friction that accompany the velocity steps. In most cases, one state variable is sufficient to fit the experimental data; in such cases, the last term of Eq. (2.1) can be deleted by setting b_2 and θ_2 as null, so that $b = b_1$ and $Dc = Dc_1$. However, in some relatively low slip velocity steps ($V \leq 30$ μm/s), bare surfaces data are best described using the two state variables, where $D_c = D_{c1} + D_{c2}$ and $b = b_1 + b_2$. We quantified the friction velocity dependence under steady-state sliding conditions through the friction rate parameter (a-b), defined as:

Eq. (2.4) $$(a\text{-}b) = \Delta\mu_{ss}/ \ln(V/V_0)$$

where $\Delta\mu_{ss}$ is the change in steady-state friction upon a step change in slip velocity from V_0 to V. In the rate-and-state friction context, positive values of *(a-b)* defined velocity strengthening behavior, that is associated with stable sliding, whereas negative values of *(a-b)*, termed velocity weakening behavior, are a requirement for the nucleation of unstable slip (e.g., *Marone*, 1998b; *Scholz*, 2002).

Time dependent frictional strength (i.e., frictional healing) was studied with slide-hold-slide (SHS) sequences that consist in alternating shearing at constant displacement rate of 10 μm/s with periods where the fault is held under quasi-stationary contact ($V = 0$). We employed hold times (t_h) of 30, 100, 300, 1000, 3000 s with 500 μm displacement at 10 μm s^{-1} after each hold (Figure 2.1f). The amount of frictional healing ($\Delta\mu$) of both gouge layers and bare surfaces was determined for each hold time as the difference between peak friction measured upon re-shear and the steady state friction value measured just before the hold, (e.g., *Frye and Marone*, 2002; *Marone*, 1998a; *Richardson and Marone,* 1999), (Figure 2.1g). By varying the hold time (t_h), we then determined the frictional healing rate (ß) for all the materials as:

Eq. (2.5) $$ß = \Delta\mu/\log_{10}(t_h)$$

The parameter ß provides an estimate of the rate of recovery of frictional strength.

2.2.2 Rotary-shear experiments

Friction experiments were also performed with the rotary-shear apparatus SHIVA (Slow to HIgh Velocity Apparatus), installed at the INGV in Rome (Italy). These tests were designed to interrogate the frictional strength at large displacement values that could not be reached with the biaxial deformation apparatus BRAVA (Figure 2.2).

SHIVA uses two brushless motors (maximum power 300 kW) in a rotary-shear configuration that supply the torque (i.e., shear stress) and the angular rotation, at nominally infinite slip. Normal load is applied to the experimental fault via an air actuator acting through a lever to amplify the resulting normal load (2t amplified to 5t). Mechanical data including axial load, torque, axial shortening, and angular rotation were acquired at a frequency of 12.5 Hz. Further details on the experimental apparatus, the control and acquisition system can be found in *Di Toro et al.* (2010) and *Niemeijer et al.* (2011). The experiments were performed on hollowed rock cylinders of basalts 50/30 mm external/internal diameter. Specimens were ground flat and parallel using a surface grinder, jacketed in aluminum ring, and embedded in epoxy, following the protocol described in *Nielsen et al.* (2012). This procedure ensured misalignment smaller than 100 μm when the samples are juxtaposed and mounted on SHIVA to simulate rock-on-rock frictional sliding. To obtain the same starting average roughness as in the slabs installed in BRAVA, basalt cylinders were subsequently roughened with #80 grit silicon carbide powders as in the direct-shear tests.

All the experiments were conducted at nominally 4 - 8 - 12 MPa normal stress and specified displacement rate of 10 μm/s, under both room-dry and water saturated conditions. To perform experiments at water-saturated conditions, SHIVA was equipped with a pressure vessel that allowed sample saturation (*Violay et al.*, 2013a, 2013b). The chamber of the pressure vessel was filled with deionized water via an ISCO Teledyne Pump, by injecting fluid at atmospheric pressure. In order to prevent fluid overpressure throughout the tests, all the experiments were carried out under drained conditions, and the fluid pressure monitored via the fluid pressure sensors located at about 5 mm from the fault zone

and internally the ISCO pump.

Furthermore, to further reduce the possible sample misalignment along the frictional interface, at the beginning of each experiment, the fault was slid for 2 mm at room-dry conditions ("shear run-in" phase), and the normal and shear load subsequently removed. In wet experiments, fault saturation followed the "run-in" phase. After reapplication of normal load, we reiterated sliding episodes of length 2 mm at 10 μm/s, followed by 2 min of hold time (displacement rate = 0), up to 8 mm slip. Then, the fault was slid steadily at 10 μm/s until the achievement of 48 mm displacement. Finally, we performed a second slide-hold-slide sequence (Figure 2.2) reaching a cumulative slip of 56 mm. These cycles were intended to monitor the fault strength evolution within small cumulative slip intervals, but since a very small increase in frictional strength within each 2 mm sliding episode is observed, we report only the measurements at 4- and 56-mm net displacements (Table S2.1).
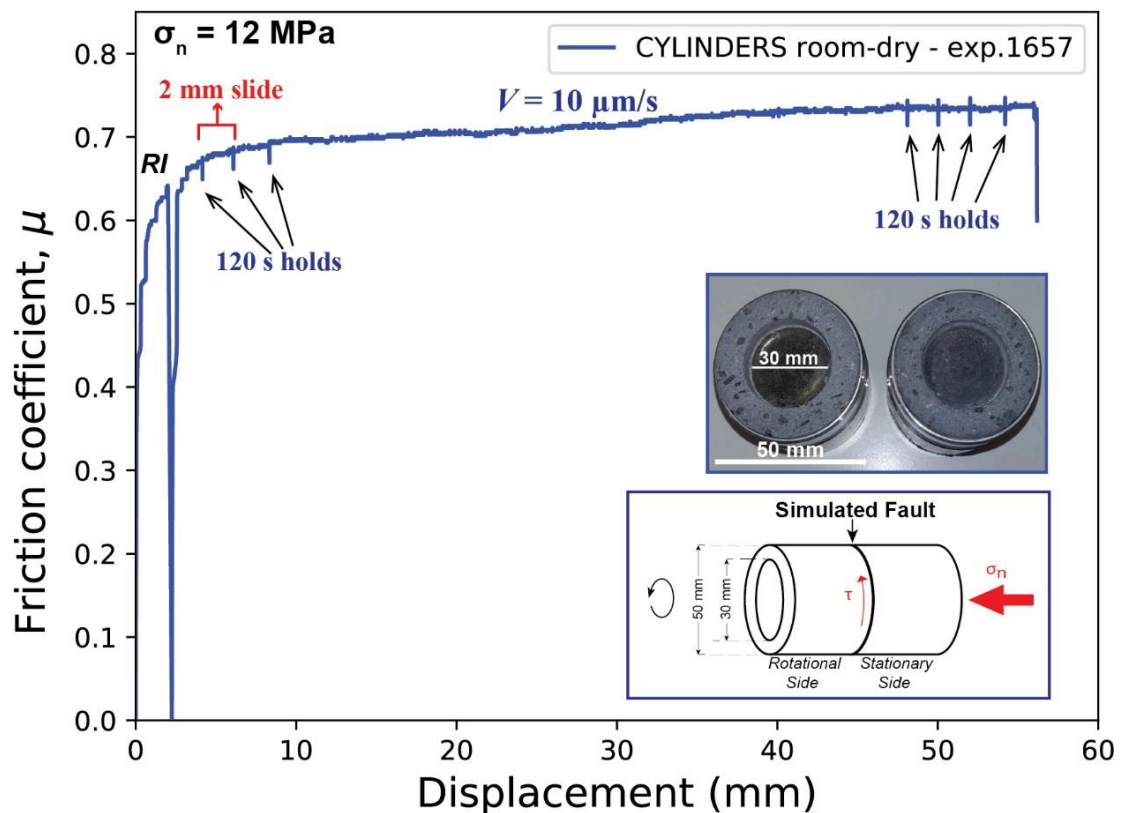
Figure 2.2. Friction against displacement curve in a typical test performed on basalt hollow cylinders with the rotary-shear apparatus SHIVA. The sequences of 2 mm sliding at 10 μm/s followed by 120 s holds were reiterated to interrogate the frictional strength evolution within small displacement intervals. RI denotes the "shear run-in" phase.

31

2.2.3 Dilatancy measurements

Dilation of granular layers due to velocity steps have been widely documented: gouge layers generally dilate in response to a velocity step increase, whereas overall compaction is expected to accompany step decreases in slip velocity (e.g., *Marone et al.*, 1990). Specifically, dilation magnitude represents a good proxy for the volumetric strain changes, hence the thickness of the shear band accommodating strain (*Marone and Kilgore*, 1993) and ultimately, the degree of strain localization: the higher the strain localization, the lower is the corresponding dilation velocity dependence. In order to determine the gouge layer evolution upon step changes in loading velocity, we measured variation in layer thickness at constant normal stress by monitoring the horizontal LVDT displacement, in accordance with the approach outlined in *Samuelson et al.* (2009) and *Scuderi et al.* (2013) (see also *Mair and Marone*, 1999; *Marone et al.*, 1990; *Scuderi et al.*, 2017). As gouge layers thin quasi-continuously with displacement due to simple shear (e.g., *Scott et al.*, 1994), we removed monotonic long-term trends in layer thickness prior to assessing dilation related to velocity perturbations (Figure S2.5b). The same method has been applied during the slide-hold-slide tests, in which the hold phase is accompanied by gouge layer compaction, while dilation occurs as load point resumes (Figure S2.5c) (see *Frye and Marone*, 2002; *Karner and Marone*, 2001 for further details). Pore volume changes paired with load point perturbations during SHS tests may provide insights on the microphysical processes responsible for the frictional healing in simulated gouge layers. Such changes were monitored at different environmental conditions (i.e., room-dry and wet conditions) to shed light on the possible contribution of compaction on the frictional restrengthening between slip events in basalts.

2.2.4 Microscopy investigations

We collected photo-mosaics of the whole thin section length and thickness with the DeltaPix M12Z optical microscope, and micrographs of the thin section details at higher magnification using a JEOL JSM-6500 F thermal field emission scanning electron microscope (FE-SEM). All the micrographs taken with the FE-SEM were back-scattered electron images. Both microscopes are located at INGV – Rome (Italy).

2.3 RESULTS

2.3.1 Frictional strength

After the initially nearly linear-elastic loading phase, the friction vs. slip curve reaches a steady-state value (τ_{ss}) with increasing displacement, at the end of the run-in phase (Figure 2.1a; 2.2). The steady-state shear strength scales linearly with the applied normal stress irrespective of the tested simulated faults, environmental conditions, and sample configurations, and can be fitted with a linear regression accordingly to the Amontons' law and with the associated coefficient of stable sliding friction, μ_{ss} at steady state.

Frictional sliding data reported in Figure 2.3 range from μ_{ss} = 0.59 to 0.78. Collectively, data agree well with Byerlee's rule for friction (*Byerlee*, 1978). Differences in sliding friction between tests performed under room-dry and water-saturated conditions, if any, are contained in the error.
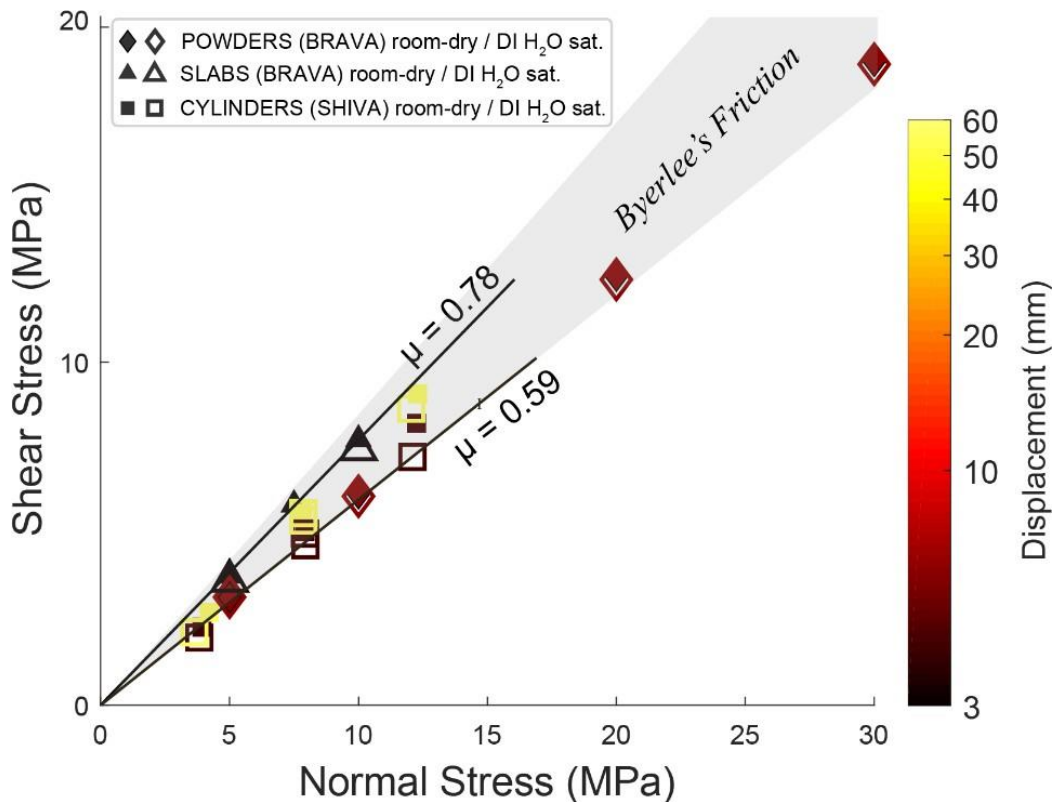
Figure 2.3. Mohr-Coulomb failure diagram reporting the compilation of shear strength values collected at different normal stresses. The linear reactivation envelopes fall within the field of Byerlee's friction law (i.e., μ = 0.6 − 0.85, shaded area), regardless of tested samples, shear configuration, and environmental conditions.

Notably, within the small friction range observed, rock-on-rock experiments revealed systematic discrepancies between the average frictional sliding measured at low displacements for bare surfaces deformed on BRAVA (μ_{ss} = 0.76) and hollow cylinders mounted on SHIVA (μ_{ss} = 0.63). The latter exhibited a very small positive rate of displacement hardening with cumulative displacement, with friction increasing from about 0.6 upon initial sliding to ~ 0.7 after 56 mm slip. We also report a slightly higher friction coefficient in bare surfaces than in simulated gouge (average μ_{ss} = 0.62), ceteris paribus.

2.3.2 Frictional stability

Figure 2.4 and 2.5 show the friction rate parameter *(a-b)* for velocity steps of experiments conducted on both fault gouge and bare surfaces. For experiments involving simulated fault gouge, the examination of the friction rate parameter *(a-b)* reveals a dependence on the normal stress and sliding velocity for both dry and water saturated samples. Our results show that for normal stress larger than 5 MPa, the frictional behavior is progressively velocity weakening with the increase of sliding velocity (Figure 2.4a, Table S2.2). Notably, at σ_n = 30 MPa simulated fault gouge transitions to slightly velocity weakening/velocity neutral behavior, with room-dry powders exhibiting a lower weakening rate when compared to their wet equivalents. At the lowest normal stress, i.e. σ_n = 5 MPa, this tendency changes to a velocity strengthening behavior at $V > 30$ μm/s, markedly under DI water-saturated conditions (Figure 2.4a).

We further investigate the frictional behavior of simulated fault gouge by exploring the evolution of the individual friction rate parameters *a* and *b*, and *Dc*. Overall, the experiments on simulated fault gouge show no discernable increase in direct effect *a* with increasing velocities. The only exception concerns the tests performed at σ_n = 30 MPa, where we observed progressively larger direct effect at the highest velocities, especially for the tests involving DI H_2O (Figure 2.4b).

SIMULATED FAULT GOUGE
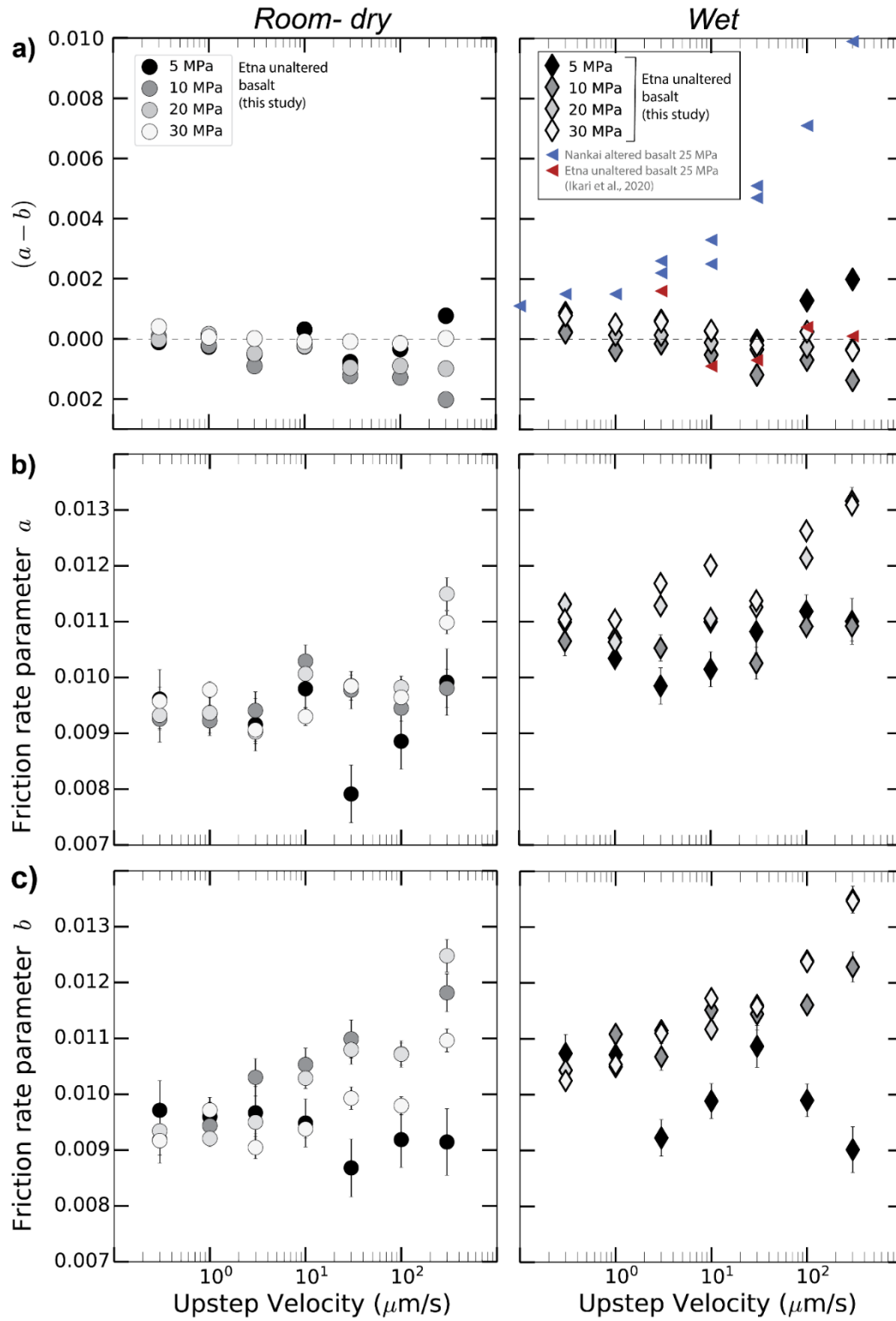
Figure 2.4. Results from velocity stepping tests in simulated fault gouge deformed at 5 to 30 MPa normal stress, under room-dry and water-saturated conditions. **(a)** Friction velocity dependence (a-b) and the associated friction rate parameters a **(b)** and b **(c)** as a function of the velocity upsteps.

We find that *(a-b)* was mostly influenced by the evolution of the friction velocity parameter *b*. In fact, at σ_n = 5 MPa *b* shows a negative trend with increasing sliding velocities (Figure 2.4c), yielding b < *a* and thus a velocity strengthening behavior. Whereas, from 10 to 30 MPa, *b* becomes progressively larger than *a* as we approached higher velocities (Figure 2.4b,c), justifying the transition from velocity strengthening/neutral to velocity weakening behavior. With regard to the critical slip distance, all the tests exhibit a general increase in *Dc* as slip velocity builds up, which is enhanced at the lowest normal stresses under wet conditions (Figure 2.5a).
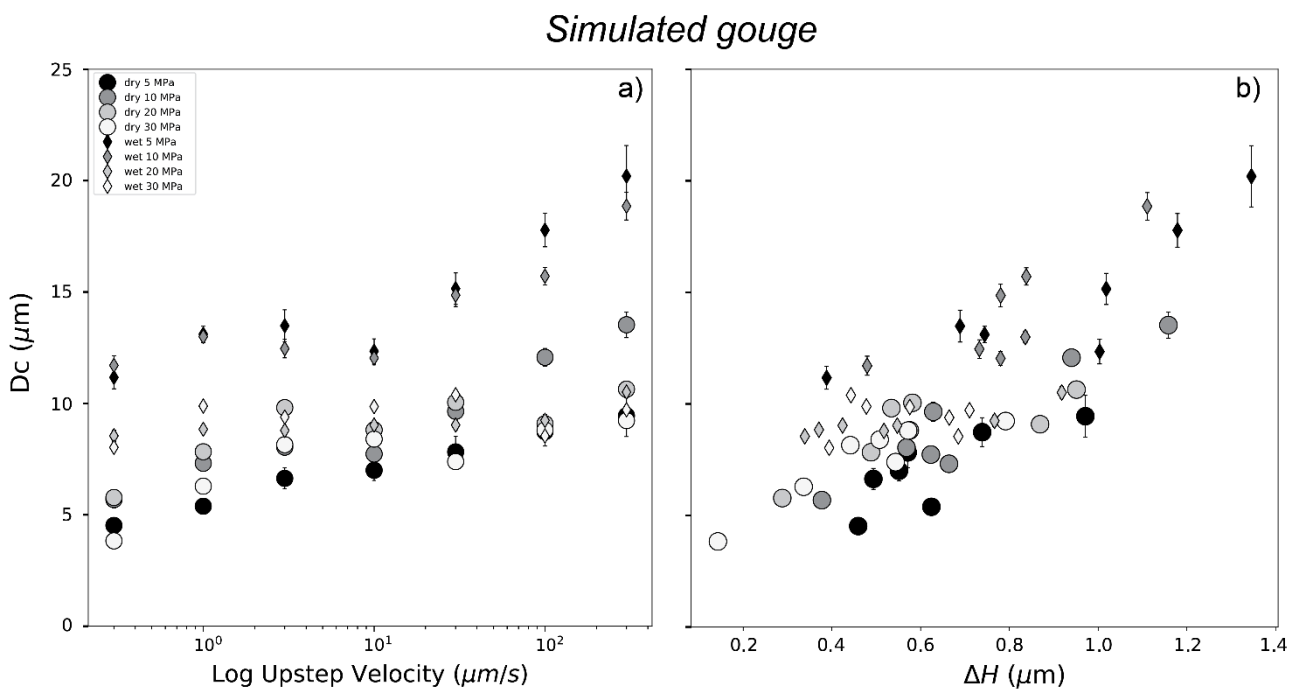
Simulated gouge

Figure 2.5. Results from velocity stepping tests in simulated fault gouge deformed at 5 to 30 MPa normal stress, under room-dry and water-saturated conditions. Critical slip distance as a function of **(a)** the velocity upsteps and **(b)** the gouge layer dilation accompanying the velocity upsteps.

Experiments on bare rock surfaces revealed a positive dependence of *(a-b)* on shear velocity *V*. We find a transition from velocity weakening at *V* ≤ 3 µm to velocity strengthening behavior at the highest velocities in particular in the case of dry surfaces. This evolution is still persistent on water-saturated samples but less pronounced. (Figure 2.6, Table S2.2). Furthermore, we note a systematic negative slip dependence of friction for all the velocity stepping tests involving shear along bare surfaces (Figure 2.1a). Bare surfaces generally show a decrease in *Dc* at higher slip velocities (Figure 2.7a). If we consider the single contributions

to the cumulative critical slip distance *Dc*, we find that *Dc1* remains fairly constant with increasing velocity within the data uncertainty (Figure 2.7b). It is worth mentioning that the outlier found at *V* = 1 μm/s and σ_n = 7.5 MPa, is probably related to the noise following the step change in velocity, that may have introduced biases in choosing between one state or two state variables during the inverse modelling. Conversely, the term *Dc2* falls in the range ~ 15- 70 μm at V≤ 3 μm/s and decreases or becomes null with increasing velocity. Therefore, the recorded decrease in *Dc* is mainly associated with the disappearance of the term *Dc2* as we approach higher slip velocities.
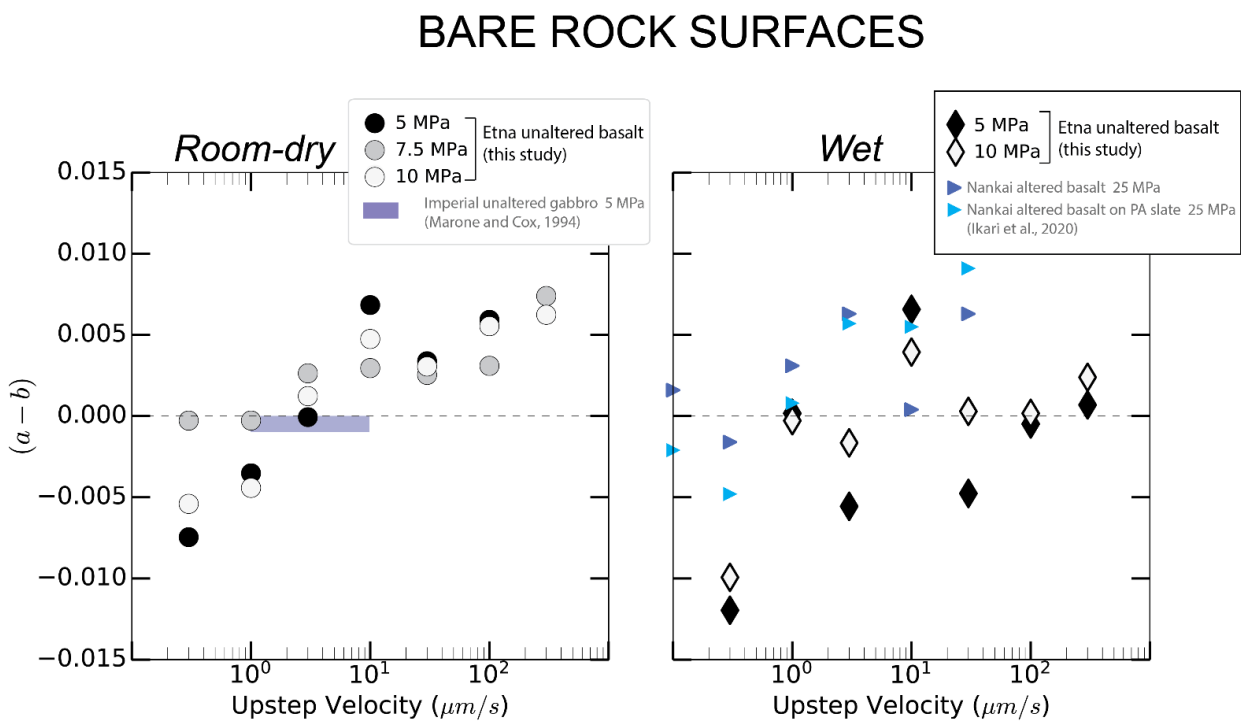
Figure 2.6. Results from velocity stepping tests in bare rock surfaces deformed at 5 to 10 MPa normal stress, under room-dry and water-saturated conditions. Evolution of the friction constitutive parameter (a-b) plotted against the velocity upsteps.
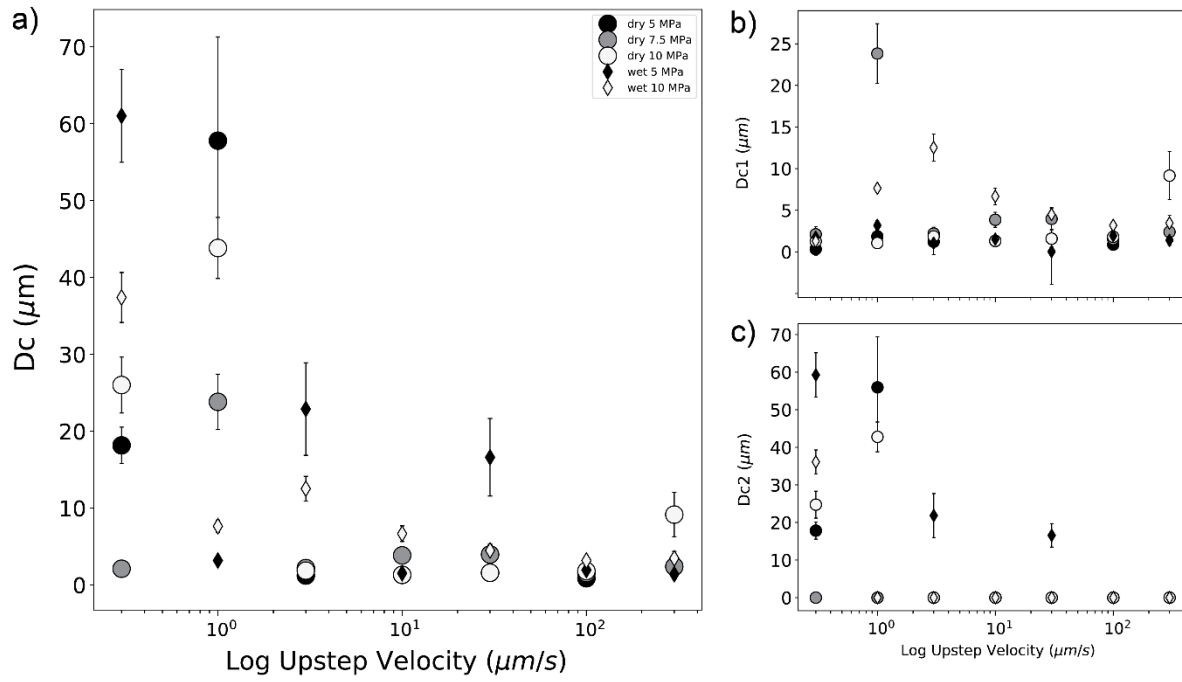
Figure 2.7. Results from velocity stepping tests in bare rock surfaces deformed at 5 to 10 MPa normal stress, under room-dry and water-saturated conditions. **(a)** Evolution of the friction constitutive parameter *Dc*, including the single terms (b) *Dc1* and *Dc2* plotted against the velocity upsteps.

2.3.3 Frictional healing

Figure 2.8 displays the healing values at different normal stresses against hold time. Frictional healing data Δμ show positive values over the entire sample suite. In detail, data involving shearing of bare rock surfaces show the largest healing rates, in the range ß = 0.0211 – 0.0265. Experiments performed with simulated fault gouge systematically exhibit lower values of healing rate than the bare surfaces equivalents, with ß from 0.0051 to 0.0128.

We also found that frictional healing for synthetic gouge evolved differently depending upon the environmental conditions: simulated fault gouges saturated with DI water have higher frictional strengthening rates (ß = 0.0091 to 0.0128) compared to room- dry samples (ß = 0.0051 to 0.0063) (Table S2.2). In contrast, such divergence was not evident in bare rock surfaces friction experiments. Furthermore, none of the experimental faults we studied showed a clear dependence of ß on the normal stress.
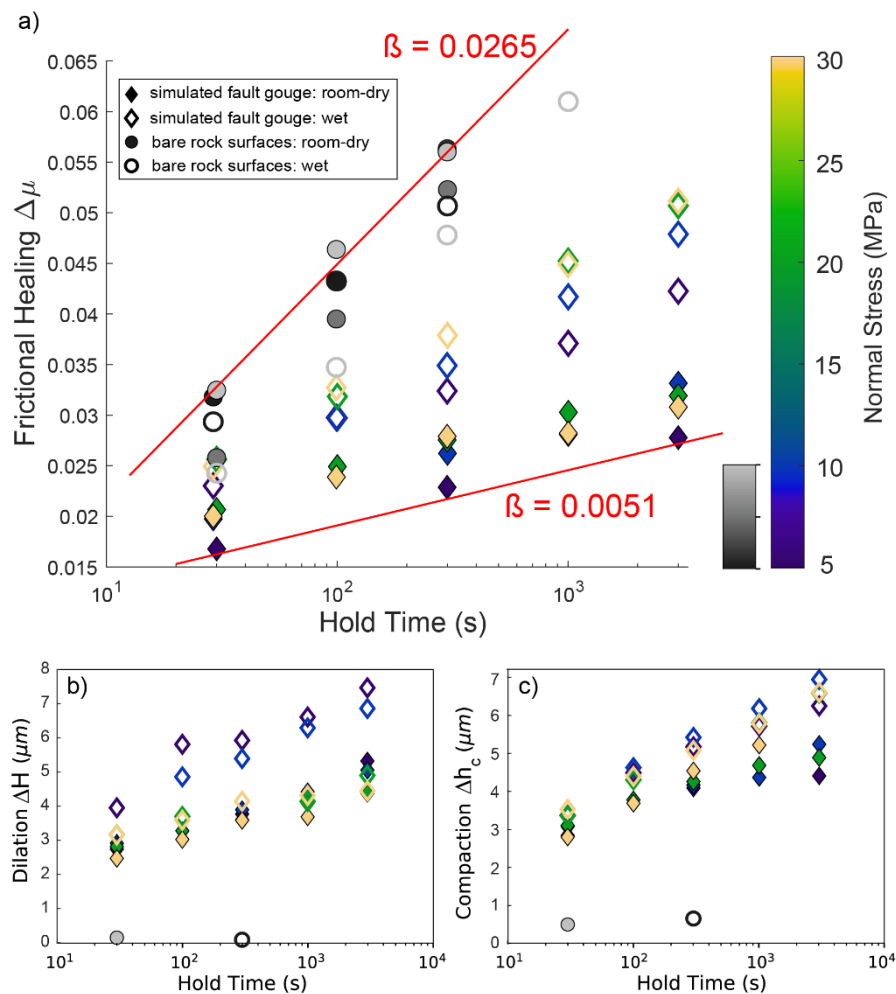
Figure 2.8. Frictional healing parameter Δμ plotted against the hold time t_h for each experimental configuration. Two populations of strengthening rates ß can be observed: lower strengthening rates for synthetic fault gouge and higher rates for bare rock surfaces. (b) Positive dilation and (c) compaction rates accompany the time-dependent friction restrengthening during slide-hold-slide tests.

## 2.3.4 Volumetric deformation during velocity steps and slide-hold-slides

In all our tested conditions, we notice that: *(a)* each velocity upstep corresponds to a transient and steady-state increase in gouge layer dilation and *(b)* volumetric strain changes occur over the same distance as the slip required for reaching a new steady state friction level upon the velocity upsteps, and therefore are significant for the stability of sliding (e.g., *Rice and Ruina*, 1983) (Figure S2.5a). Steady state values were then averaged over the entire duration of the velocity steps and plotted against normal stress (Figure 2.9). We therefore define ΔH as the average steady-state layer dilation in response to a velocity step (*Marone and Kilgore*, 1993).

Overall, the experiments show an increase in ΔH with increasing sliding velocity in the range of 0.2 < ΔH < 1.4 μm, but smaller dilation values towards larger normal stresses. Under water-saturated conditions, samples sheared at σ_n = 5 MPa exhibit higher ΔH when compared to their room-dry equivalents (Figure 2.9). Our data also indicate a direct relation between the extent of dilation following the velocity steps and the critical slip distance, *Dc* (Figure 2.5b), in agreement with findings of *Marone and Kilgore* (1993). Due to the higher noise characterizing the H-LVDT data for initially bare surfaces, we could not investigate the dilation during such velocity steps. Similarly, only in a few cases dilation and compaction measurements were possible following SHS tests.

Analysis of volumetric changes during such tests, indicate that positive healing rates are accompanied by increases in dilation and compaction with log time, whose values are generally higher for powders relative to bare surfaces (Figure 2.8b,c). We find that dilation in simulated gouge increases log-linearly with hold time, with the largest magnitudes found at the lowest normal stresses under wet conditions (Figure 2.8b). Conversely, compaction data display a bimodal trend depending on the environmental conditions: SHS compaction increases linearly with log hold time in gouge layers sheared under wet conditions, which is

consistently higher in comparison to their room-dry analogues, for the entire range of conditions investigated (Figure 2.8c).

SIMULATED FAULT GOUGE
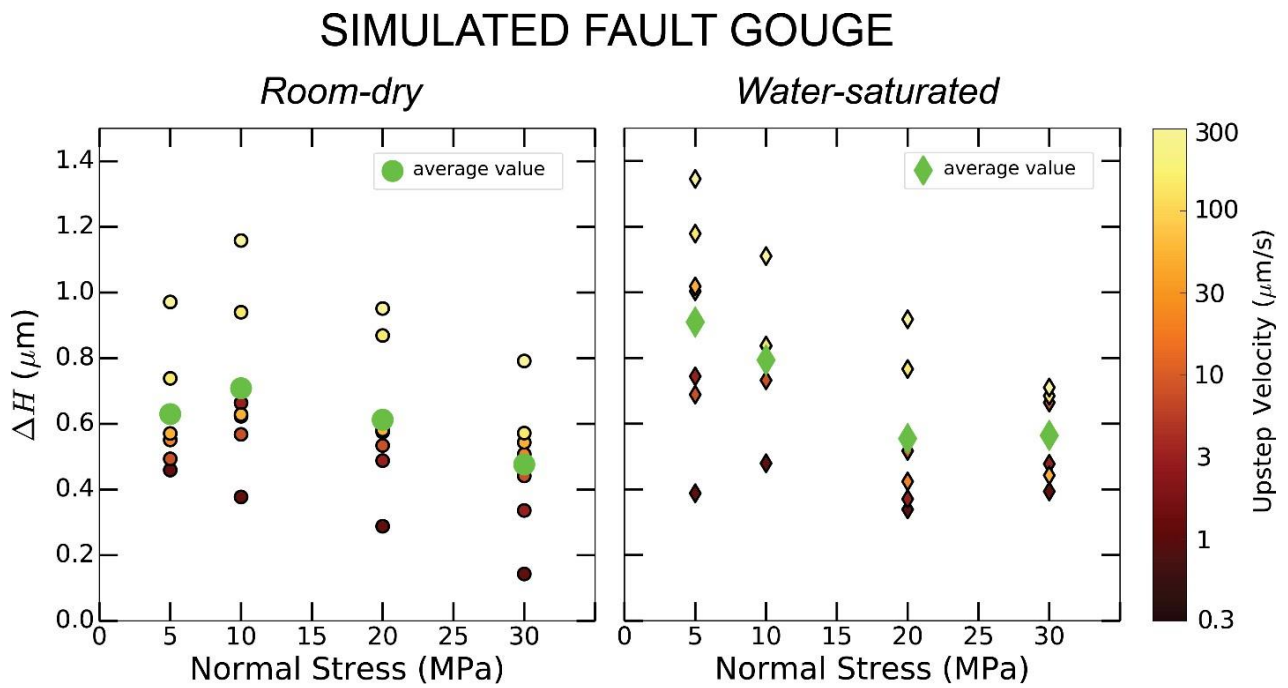
Figure 2.9. Steady-state dilation changes as a function of the normal stress and the velocity upsteps. Green symbols represent the mean dilation value.

2.3.5 Microstructural observations

2.3.5.1 Simulated fault gouge

We carried out microstructural analysis at the optical and scanning electron microscopes on our deformed gouge layers which had been impregnated with low viscosity epoxy resin after unloading. Our main observations point to a progressive microstructural reorganization with increasing normal stresses, under both room-dry and water-saturated conditions. The entire compilation of optical micrographs is displayed in Figure S2.6, Suppl. Mat.

2.3.5.1.1   Simulated gouge: low normal stresses microstructures

At low normal stress (σ_n < 10 MPa), we observed the development of incipient shear bands along Riedel R1 and B orientations (*Logan*, 1979). Proto B shears are continuous, located at both sides of the fault zone. Conversely, proto-R1 are discontinuous, they start from the boundaries of the gouge layers and subsequently curve at low angle (~ 15°) with the direction of shear (Figure 2.10a).

Both shear planes are characterized by a thickness of ~ 50-70 μm (Figure 2.10b, c), enriched in fine-grained material that surrounds larger angular clasts isotropically-oriented (Figure 2.10c). However, the large presence of grains along the shear bands with comparable dimension to that of the starting material (Figure S2.4, Suppl. Mat.) suggests that *(i)* shearing along incipient R1 and B is not significantly affected by grain-size reduction, and *(ii)* most of the shear deformation is distributed within the bulk volume of the simulated fault gouge. Therefore, we posit that due to the low applied normal stress, it is likely that the incipient shear zones mostly derive from the accumulation of fine grains from the regions of the starting material characterized by small particle sizes and much of the deformation was accommodated via frictional sliding at the grain contacts, rotation and translation, with no predominant role of grain size reduction during shearing (e.g., *Biegel et al.*, 1989; *Engelder*, 1974).
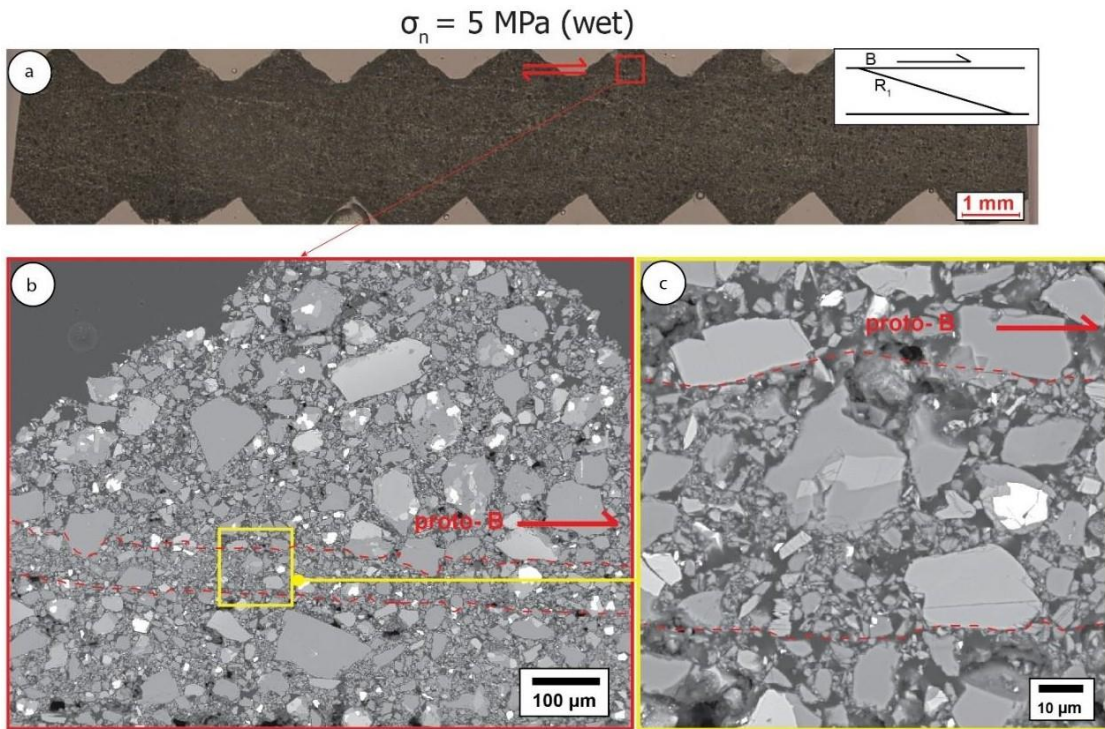
Figure 2.10. (a) Optical microscope picture of a simulated basalt fault gouge deformed at low normal stress at water saturated conditions. **(b)** Back-scattered image of the proto-boundary shear zone and **(c)** enlargement within the proto-B showing details of the shear band microstructure.
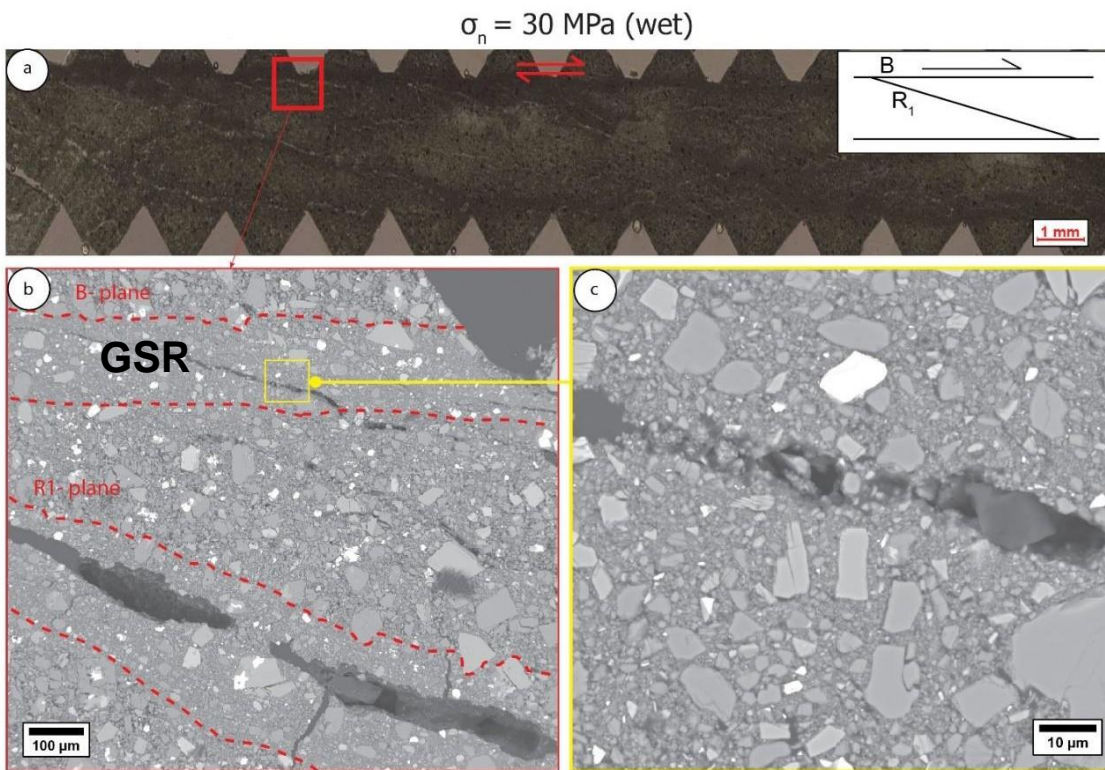
Figure 2.11. (a) Micrograph of a basalt layer deformed at 30 MPa normal stress. The sense of shear is shown by the arrows. **(b)** Backscatter scanning electron (SEM) image highlighting the R1 and B shear planes characterized by enhanced grain size reduction (GSR). **(c)** Enlargement of a B-shear zone representing the prominent microstructure of a typical localized shear zone observed at $\sigma_n \geq 10$ MPa.

Under dry conditions, we do not observe the development of incipient R1 and B shear zones, suggesting that the whole bulk gouge volume participated in the deformation (Figure S2.6).

### 2.3.5.1.2 Simulated gouge: higher normal stress microstructures

Observations under the optical microscope reveal shear planes R1 and B affected by significant grain-size reduction (Figure 2.11). This testifies that at higher normal stresses (i.e., $\sigma_n \geq$ 10 MPa), shear deformation was predominantly localized along well-developed shear planes B and R1, whilst particles essentially retained their original size elsewhere in the gouge.

Comparisons with the microstructures observed at 5 MPa indicate a progressive sharpening and thickening of B and R1 with increasing normal stress (from 70 to 200 um thickness with σ_n in the range 5-30 MPa). Both B and R1 shear zones are the loci of cataclastic processes with extensive grain size reduction (GSR in Figure 2.11b; see also e.g., *Logan*, 1979; *Logan and Rauenzahn*, 1987; *Logan et al.*, 1992). Shear bands B and R1 are typically separated by relic pockets of relatively undeformed material and consist of sub-angular larger clasts, with grain size comparable with the starting material (~ 20 -70 μm), sustained by a fine-grained matrix (Figure 2.11c). Larger clasts located within the shear zones and at the shear zone interfaces are characterized by limited chipping and fracturing (e.g., *Billi*, 2010), whereas fine-grained material consists of angular grains with size << 10 μm, derived from localized cataclasis and also from the starting material due to the plausible redistribution of finer undeformed basalt grains along shear zones. Both larger and fine grains are randomly oriented within the bulk gouge layer.

2.3.5.2 Bare rock surfaces

In sliding experiments executed with bare rock surfaces, samples exhibited similar macroscopic deformation structures despite differences in geometry of the specimens and in the deformation apparatuses. The slipping zones that are produced at the end of each experiment consist of lineated principal slip surfaces, characterized by a few microns-thick cohesive gouge with mechanical wear streaks along the entire slipping surface, elongated in the slip direction (Figure 2.12a,b). The gouge overlies the slip surfaces and covered the grooves ploughed into the basalt surfaces during shearing of the surface asperities. As anticipated, slip surfaces subjected to higher normal stresses produce more wear material with progressive slip (Figure S2.7; e.g. *Badt et al.*, 2016; *Tesei et al.*, 2017).

Furthermore, cylinders deformed on SHIVA at room-dry conditions also preserved tool marks consisting of high relief gouge patches displaced by slip-perpendicular steps (Figure 2.12a). This feature was not observed during DI-H_2O saturated experiments, since most of the gouge layer was flushed away with water during the sample recovery, as previously pointed out by e.g., *Violay et al.* (2013b) and *Giacomel et al.* (2018).
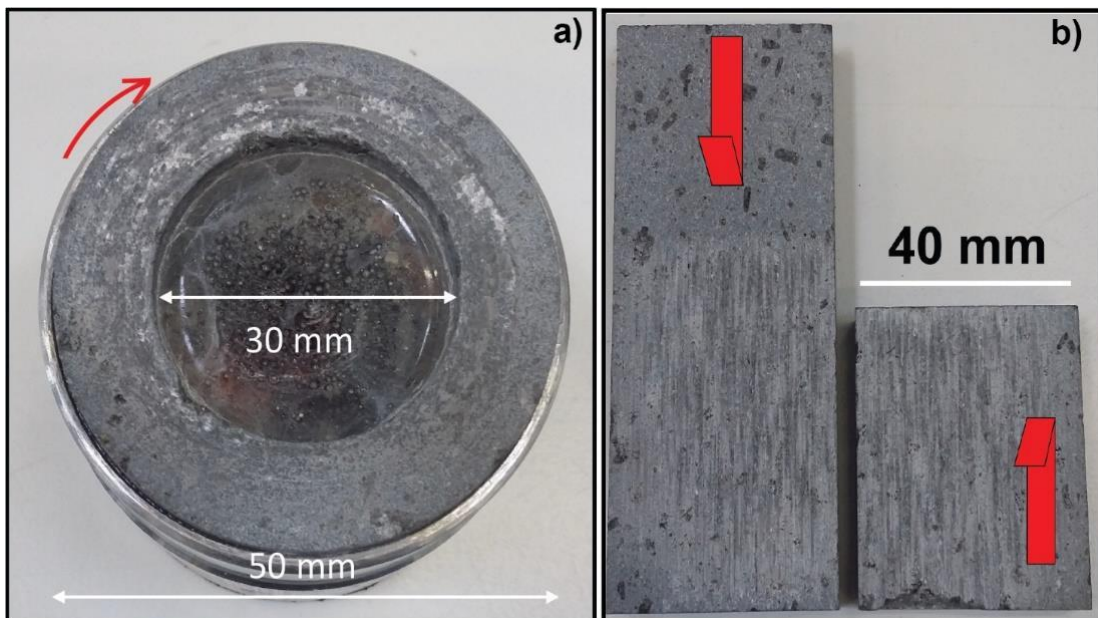
Figure 2.12. Macroscopic deformation structures of post-tested simulated basalt fault planes with their characteristic frictional wearing features. The bare surfaces were deformed at $\sigma_n = 8$ MPa **(a)** and 10 MPa **(b)** under room-dry conditions, in a rotary-shear **(a)** and direct shear **(b)** configuration.

2.4 DISCUSSION:

2.4.1 The role of localization vs. delocalization in basalt fault slip behavior

We merge our mechanical data with microstructural analysis to gain better insights on the physical processes at the origin of the frictional properties of basalt faults.

As anticipated, fault strength in our tests is in the range of the Byerlee's rule for friction and varies only slightly among tests employing different experimental configurations and sample geometries, given the relative friction data scatter expected at low normal stresses for solid silicate-bearing rocks (*Byerlee*, 1978). This evidence testifies that our data are not particularly affected by artifacts resulting from the experimental design. Minor discrepancies in sliding friction coefficient deriving from the different sample geometries we employed may be due to *(i)* local stress heterogeneities along bare rock surfaces, which could arise from the 0.1 mm tolerance of the sample grinder as well as the starting roughness, *(ii)* possible different textural evolution characterizing shear within gouge and between bare rock surfaces, and *(iii)* the different method employed in direct shear and rotary shear configurations to calculate the shear stress acting along the frictional interface (see *Shimamoto and Tsutsumi, 1994* for details). Furthermore, the small displacement hardening observed in rotary shear tests reflects the accumulation of a ~ 50 μm thick gouge layer coating on the sliding bare surfaces after 56 mm slip, in good agreement with findings of *Marone and Cox* (1994) and *Mitchell et al.* (2015) on bare surfaces of gabbros at 5 MPa normal stress. The elevated healing rates (ß) regardless of the simulated fault type employed in our tests, coupled with the high frictional strength are typical hallmarks of faults with frictionally strong mineral phases such as the primary phases constituting basalts i.e., olivine, pyroxene, and plagioclase. Within this framework, the highest healing rates related to basalt bare surfaces can be interpreted in terms of asperity interaction and specifically, by invoking a larger contact junction size for bare surfaces with respect to simulated gouge. The positive correlation between higher friction restrengthening and compaction rates in wet compared to room-dry gouge samples, attests that compaction during the hold periods represents a key fraction of the frictional healing in (unaltered) basalt fault gouge, which is aided by the

presence of water. However, we cannot rule out that slip-dependent processes also participated in fault restrengthening during creep relaxation, nor a possible contribution of water-assisted time-dependent strengthening of grain contacts (e.g., *Frye and Marone*, 2002).

For the velocity dependence of friction, our results illustrate heterogeneous frictional stability behavior according to the different configurations, represented by bare rock surfaces or simulated fault gouge, and the normal stress at which faults are subjected. The frictional behavior of bare surfaces and simulated fault gouge is the opposite with increasing velocity and displacement.

Regarding powdered gouge, we find that the measurements of friction rate dependence, critical slip distance, dilation, and microstructural observations are interrelated. At 5 MPa normal stress, *(i)* the small friction rate parameter *b* throughout the velocity stepping sequences (Figure 2.4c), associated with *(ii)* the limited grain size reduction characterizing proto B-shears (Figure 2.10), *(iii)* the large gouge layer dilation at high velocities (Figure 2.9) and *(iv)* the coupled large *Dc* (Figure 2.5), testify that deformation is essentially distributed and dominated by grain rolling or sliding rather than grain comminution processes, and consequently explains the recognized rate strengthening behavior as we approached higher slip velocities (Figure 2.4a). This behavior is more pronounced in wet experiments at the highest slip velocities (Figure 2.4a) probably due to the more significant dilation effect compared to their room-dry equivalents (Figure 2.9), which entails a higher excess in work done against the normal stress (*Marone et al.*, 1990) and thus a higher frictional resistance upon velocity upsteps. On the contrary, at $\sigma_n \geq 10$ MPa, the progressively larger *b* with slip velocity (Figure 2.4c) correlates with the observed strain localization along continuous R1 and B shears accompanied by cataclasis and grain size reduction (Figure 2.11), resulting in the recorded velocity weakening behavior, as previously reported by laboratory observations on simulated gouge (e.g., *Mair and Marone*, 1999). The enhanced strain localization at $\sigma_n \geq 10$ MPa is also corroborated by the overall lower dilation values paired with lower *Dc* values, recorded at progressively higher normal stresses (Figure 2.9; 2.5b). The velocity weakening behavior, induced by shear localization,

coupled with the high healing rates and high shear strength, render fault zones characterized by basalt gouge good candidates to potentially host the nucleation of seismic events.

In marked contrast, the positive evolution of the friction rate parameter (*a-b*) with increasing slip velocity in bare surfaces sheared at σ_n = 5 to 10 MPa (Figure 2.6), results in a transition to slightly or strong rate strengthening behavior for wet and room-dry conditions, respectively. A possible explanation for the switch to rate-strengthening behavior could involve shear delocalization that may have occurred due to frictional wear production and played a key role in strengthening the bare surfaces upon velocity steps. It is indeed well documented that gouge accumulation during shear of initially bare surfaces tends to stabilize slip, especially at low applied normal stresses (*Byerlee,* 1967; *Byerlee and Summers,* 1976; *Scholz et al.*, 1972; *Engelder,* 1975; *Wong et al.,* 1992). In addition, the experimental work documented in *Marone et al.* (1990) and *Marone* (1998b) highlights the strict relation between strain delocalization following the presence of a gouge layer during slip along bare rock surfaces and the increase in the friction rate parameter *(a-b)*. This effect is further magnified with increasing the initial surface roughness. Recent published studies by *Ikari et al.*, (2020) at 25 MPa effective normal stress, further corroborate the pivotal role played by shear dilation during the velocity steps, causing the switch to velocity strengthening friction even when slip nucleates along altered (clay-rich) basalt rock-on-rock contacts (Figure 2.6). In the light of these observations, comparisons between friction stability data covering small net displacements (≤ 12 mm) on *a)* (unaltered) gabbro bare surfaces from Marone and Cox, (1994) at 5 MPa normal stress, *b)* (unaltered) basalt surfaces from our tests, and *c)* (altered) basalt surfaces from *Ikari et al.*, 2020 (Figure 2.6), point to an inherent tendency for unstable sliding at low slip velocities in frictionally strong bare surfaces of basalts and gabbros, which is overcome by a strengthening effect at higher velocities due to changes in dilatancy rates.

To summarize, we postulate that (unaltered) simulated fault gouge and rough bare surfaces represent two basalt structural end-members, whose contrasting evolution of the rate and state constitutive parameter (*a-b*) with increasing sliding velocity and slip possibly results from two opposite mechanical processes operating during frictional sliding: on one hand, shear within simulated fault gouge is characterized by cataclasis with grain size

reduction and localization that facilitates the transition to velocity neutral/weakening behavior; on the other hand, gouge development during slip along bare surfaces likely involves shear delocalization that entails the evolution towards velocity strengthening behavior. However, we envisage that dilatancy-strengthening is probably a small net displacement process, because, as we observed from our tests at large accumulated slip, the bare surfaces are likely to be greatly affected by production of gouge during shearing (Figure 2.12a), in particular with increasing normal stresses (Figure S2.7). We thus posit that at large displacements, once gouge layer becomes thick enough with respect to the bare surface roughness, rock surfaces separated by the gouge layer would start to localize deformation within the gouge, that would lead samples to become progressively velocity weakening and potentially unstable (Figure 2.4a).

2.4.2 Implications for the slip behavior of shallow faults in volcano-tectonic settings and basalt-hosted geo-energy sites

In our laboratory friction experiments, we investigated an effective normal stress interval of 5-30 MPa, which corresponds to an in-situ depth up to ~ 2-3 km, depending on hydrostatic or supra-hydrostatic fluid pressure levels. At these inferred depths, wet conditions are expected to represent more realistic conditions of shearing rather than room-dry tests. It should be emphasized that the experimental protocol enables us to investigate the friction stability and healing rates at low strains (γ~4) and displacements, implying that our tests mimic only the early stages of structural evolution that accompanies slip localization within unaltered basalt fault gouge or competent rock. Therefore, our data provide mechanical connections with unaltered basalt gouge-rich shear zones and incipient fault zones in the presence of pervasive jointed networks, such as those potentially located in CarbFix-like sites or active shallow volcano-tectonic settings. In these geological environments the documented combination of high-strength for unaltered basalt fault gouge, with prevalent velocity weakening behavior and important healing rates, define potentially unstable zones that would explain some of the slip instabilities documented in active volcano-tectonic settings such as along the shallow flanks and edifices of the Hawaiian (*Denlinger and Morgan*, 2014; *Klein et al.*, 1987; *Lockwood et al.*, 1987) and Etnean (*Alparone et al.*, 2013; *Azzaro et al.*, 2017) volcanoes. On the contrary, fault maturity within basalt shear zones and associated fluid assisted reaction softening promote the development of interconnected clay networks that would favor the transition to a predominant velocity strengthening friction, thus a tendency for stable sliding behavior (Figure 4b; *Ikari et al.*, 2011, 2020).

The observed switch from velocity weakening to strengthening of bare surfaces with increasing sliding velocity indicates that slip initiation in rough jointed surfaces may be possible at slow sliding velocity (V≤ 10 μm/s), yet unstable slip would be suppressed at higher rates, resulting either into stable sliding or limited coseismic slip rates, stress drop and cumulated slip (e.g., *Blanpied et al.*, 1998b; *Weeks*, 1993). In this second scenario, the superposition of the negative slip dependence of friction following the velocity steps (Figure

1a) may counteract the slightly velocity strengthening/neutral behavior at the highest slip velocities (Figure 2.6), and possibly result in a net weakening that would favor slip acceleration even at higher slip rates than predicted from our rate-and-state friction analysis (*Ikari et al.*, 2013; *Ito and Ikari*, 2015). This observation, coupled with the significant propensity of bare surfaces to regain strength following the slip events (Figure 2.8), suggests the possibility to develop potential unstable faults from incipient basalt jointed networks with important implications for the long-term integrity and stability of basalt-hosted geo-energy sites, including the CO_2 repositories.

2.5 CONCLUSIONS

We carried out a series of laboratory friction experiments intended to explore the role of experimental fault structure, defined by simulated gouge and rough bare rock surfaces, on the frictional properties and constitutive parameters of unaltered basalt-built faults. Samples were deformed under room-dry and wet conditions in a direct- and a rotary-shear configuration, at normal stresses up to 30 MPa at ambient temperature, which are deemed to represent the conditions for fault slip in some areas such as those potentially suitable for in-situ geological carbon storage and active volcano-tectonic settings.

Our results indicate that: (1) the elevated friction coefficient (μ = 0.59- 0.78) and high healing rates (ß = 0.0055 – 0.0265) render basalt faults frictionally strong and able to rapidly regain the shear strength necessary for repeated fault reactivation throughout the geological fault history; (2) shear along bare rock surfaces and within simulated gouge led to opposite frictional stability behavior in the velocity range investigated (V = 0.1 – 300 µm/s): while powdered gouge switch to velocity weakening behavior with increasing slip velocity and displacement, bare surfaces transition to velocity strengthening behavior. Consequently, (3) the strong correlation at increasing normal stress between velocity weakening behavior and shear localization along B and R1 shear planes with grain size reduction, coupled with the high healing rates and high shear strength, render fault zones characterized by basalt gouge good candidates to potentially host seismic nucleation and rupture propagation; (4) the observed velocity strengthening behavior accompanied by gouge production during shearing, would render initially rough bare surfaces less prone to unstable slip.

Overall, we envisage from our tests that a thorough knowledge of the complexity of fault structure would be of paramount importance to mitigate the seismic risk associated to volcano-tectonic regions dominated by basalts and before embarking in industrial scale geo-energy projects, where large volumes of fluid are anticipated to be injected into such formations. Nonetheless, further research aimed at investigating how textural and mineralogical maturity, temperature, and pore fluid pressure may influence the frictional strength, stability, and healing properties of basalt-built faults, would be warranted to extend

the laboratory-based seismic risk assessment to a broader range of targets-bearing basaltic rocks.

ACKNOWLEDGEMENTS

REFERENCES

Aki, K., & Ferrazzini, V. (2001). Comparison of Mount Etna, Kilauea, and Piton de la Fournaise by a quantitative modeling of their eruption histories. *Journal of Geophysical Research: Solid Earth*, *106*(B3), 4091-4102.

Alfredsson, H. A., E. H. Oelkers, B. S. Hardarsson, H. Franzson, E. Gunnlaugsson, and S. R. Gislason (2013), The geology and water chemistry of the Hellisheidi, SW-Iceland carbon storage site, *International Journal of Greenhouse Gas Control*, *12*, 399-418, doi:10.1016/j.ijggc.2012.11.019.

Alparone, S., Cocina, O., Gambino, S., Mostaccio, A., Spampinato, S., Tuvè, T., & Ursino, A. (2013). Seismological features of the Pernicana–Provenzana Fault System (Mt. Etna, Italy) and implications for the dynamics of northeastern flank of the volcano. *Journal of volcanology and geothermal research*, *251*, 16-26.

Azzaro, R., G. Barberi, S. D'Amico, B. Pace, L. Peruzza, and T. Tuvè (2017), When probabilistic seismic hazard climbs volcanoes: the Mt. Etna case, Italy – Part 1: Model components for sources parameterization, *Nat. Hazards Earth Syst. Sci.*, *17*(11), 1981-1998, doi:10.5194/nhess-17-1981-2017.

Azzaro, R., D'Amico, S., Peruzza, L., & Tuvè, T. (2013). Probabilistic seismic hazard at Mt. Etna (Italy): the contribution of local fault activity in mid-term assessment. *Journal of volcanology and geothermal research*, *251*, 158-169.

Badt, N., Y. H. Hatzor, R. Toussaint, and A. Sagy (2016), Geometrical evolution of interlocked rough slip surfaces: The role of normal stress, *Earth and Planetary Science Letters*, *443*, 153-161, doi:10.1016/j.epsl.2016.03.026.

Ben-Zion, Y. (2001), Dynamic ruptures in recent models of earthquake faults, *Journal of the Mechanics and Physics of Solids*, *49*(9), 2209-2244, doi:https://doi.org/10.1016/S0022-5096(01)00036-9.

Billi, A. (2010), Microtectonics of low-P low-T carbonate fault rocks, *Journal of Structural Geology*, *32*(9), 1392-1402, doi:10.1016/j.jsg.2009.05.007.

Biegel, R. L., C. G. Sammis, and J. H. Dieterich (1989), The frictional properties of a simulated gouge having a fractal particle distribution, *Journal of Structural Geology*, *11*(7), 827-846, doi: https://doi.org/10.1016/0191-8141(89)90101-6.

Blanpied, M. L., Marone, C. J., Lockner, D. A., Byerlee, J. D., & King, D. P. (1998a). Quantitative measure of the variation in fault rheology due to fluid-rock interactions. *Journal of Geophysical Research: Solid Earth, 103(B5), 9691-9712*, doi:10.1029/98jb00162.

Blanpied, M. L., T. E. Tullis, and J. D. Weeks (1998b), Effects of slip, slip rate, and shear heating on the friction of granite, *Journal of Geophysical Research B: Solid Earth*, *103*(1), 489-511.

Boatwright, J., and M. Cocco (1996), Frictional constraints on crustal faulting, *Journal of Geophysical Research: Solid Earth*, *101*(B6), 13895-13909, doi:10.1029/96JB00405.

Brace, W. F., and J. D. Byerlee (1966), Stick-Slip as a Mechanism for Earthquakes. *Science*, *153*(3739), 990-992, doi:10.1126/science.153.3739.990.

Branca, S., M. Coltelli, and G. Groppelli (2011), Geological evolution of a complex basaltic stratovolcano: Mount Etna, Italy, *Italian Journal of Geosciences*, *130*(3), 306-317.

Byerlee JD. 1967. Frictional characteristics of granite under high confining pressure. *J. Geophys. Res.* 72:3639–48

Byerlee, J. (1978), Friction of rocks, *pure and applied geophysics*, *116*(4), 615-626, doi:10.1007/BF00876528.

Byerlee, J., & Summers, R. (1976, January). A note on the effect of fault gouge thickness on fault stability. In *International Journal of Rock Mechanics and Mining Sciences & Geomechanics Abstracts* (Vol. 13, No. 1, pp. 35-36). Pergamon.

Carpenter, B. M., M. M. Scuderi, C. Collettini, and C. Marone (2014), Frictional heterogeneities on carbonate-bearing normal faults: Insights from the Monte Maggio Fault, Italy. *Journal of Geophysical Research: Solid Earth*, *119*(12), 9062-9076, doi:10.1002/2014jb011337.

Collettini, C., and R. H. Sibson (2001), Normal faults, normal friction?, *Geology*, *29*(10), 927-930, doi:10.1130/0091-7613(2001)029<0927:Nfnf>2.0.Co;2.

Collettini, C., G. Di Stefano, B. Carpenter, P. Scarlato, T. Tesei, S. Mollo, F. Trippetta, C. Marone, G. Romeo, and L. Chiaraluce (2014), A novel and versatile apparatus for brittle rock deformation, *International Journal of Rock Mechanics and Mining Sciences*, *66*, 114-123, doi:10.1016/j.ijrmms.2013.12.005.

Collettini, C., T. Tesei, M. Scuderi, B. Carpenter, and C. Viti (2019), Beyond Byerlee friction, weak faults and implications for slip behavior, *Earth and Planetary Science Letters*, *519*, doi:10.1016/j.epsl.2019.05.011.

Cox, S. J. D., Velocity dependent friction in a large direct shear experiment on gabbro. In *Deformation Mechanisms, Rheology, and Tectonics* (eds. Knipe, R. J, and Rutter, E.H.) (Geol. Soc. London 1990) Spec. Pub. *54,* pp. 63-70.

Denlinger, R. P., & Morgan, J. K. (2014). *Instability of Hawaiian volcanoes: Chapter 4 in Characteristics of Hawaiian volcanoes* (No. 1801-4, pp. 149-176). US Geological Survey.

Di Stefano, R., C. Chiarabba, L. Chiaraluce, M. Cocco, P. De Gori, D. Piccinini, and L. Valoroso (2011), Fault zone properties affecting the rupture evolution of the 2009 (Mw 6.1) L'Aquila earthquake (central Italy): Insights from seismic tomography, *Geophysical Research Letters*, *38*(10), doi:10.1029/2011GL047365.

Di Toro, G., Niemeijer, A., Tripoli, A., Nielsen, S., Di Felice, F., Scarlato, P., ... & Smith, S. (2010). From field geology to earthquake simulation: a new state-of-the-art tool to investigate rock friction during the seismic cycle (SHIVA). *Rendiconti Lincei*, *21*(1), 95-114, doi:10.1007/s12210-010-0097-x.

Dieterich, J. H. (1979), Modeling of rock friction: 1. Experimental results and constitutive equations, *Journal of Geophysical Research*, *84*(B5), doi:10.1029/JB084iB05p02161.

Engelder, J. T. (1974), Cataclasis and the generation of fault gouge, *Geological Society of America Bulletin*, *85*(10), 1515-1522.

Engelder JT, Logan JM, Handin J. 1975. The sliding characteristics of sandstone on quartz fault-gouge. *Pure Appl. Geophys.* 113:69–86

Frye, K. M., and C. Marone (2002), Effect of humidity on granular friction at room temperature, *Journal of Geophysical Research: Solid Earth*, *107*(B11), ETG 11-11-ETG 11-13, doi:10.1029/2001jb000654.

Garcia, M. O., & Davis, M. G. (2001). Submarine growth and internal structure of ocean island volcanoes based on submarine observations of Mauna Loa volcano, Hawaii. *Geology*, *29*(2), 163-166.

Giacomel, P., E. Spagnuolo, M. Nazzari, A. Marzoli, F. Passelegue, N. Youbi, and G. Di Toro (2018), Frictional Instabilities and Carbonation of Basalts Triggered by Injection of Pressurized H2 O- and CO2 - Rich Fluids, *Geophysical Research Letters*, doi:10.1029/2018gl078082.

Giacomel, P.; Ruggieri, R.; Scuderi, M. M.; Spagnuolo, E.; Di Toro, G.; Collettini, C. (2020): Mechanical data of simulated basalt-built faults from rotary shear and direct shear experiments. GFZ Data Services. https://doi.org/10.5880/fidgeo.2020.035

Gislason, S. R., D. Wolff-Boenisch, A. Stefansson, E. H. Oelkers, E. Gunnlaugsson, H. Sigurdardottir, B. Sigfusson, W. S. Broecker, J. M. Matter, and M. Stute (2010), Mineral sequestration of carbon dioxide in basalt: A pre-injection overview of the CarbFix project, *International Journal of Greenhouse Gas Control*, *4*(3), 537-545, doi:10.1016/j.ijggc.2009.11.013.

Goldberg, D. S., Kent, D. V., & Olsen, P. E. (2010). Potential on-shore and off-shore reservoirs for CO2 sequestration in Central Atlantic magmatic province basalts. *Proceedings of the National Academy of Sciences*, *107*(4), 1327-1332.

Haines, S. H., B. Kaproth, C. Marone, D. Saffer, and B. van der Pluijm (2013), Shear zones in clay-rich fault gouge: A laboratory study of fabric development and evolution, *Journal of Structural Geology*, *51*, 206-225, doi: https://doi.org/10.1016/j.jsg.2013.01.002

Hatton, C.G., Main, I.G., and Meredith, P.G., 1994, Non-universal scaling of fracture length and opening displacement: Nature, v. 367, p. 160–162, doi:10.1038/367160a0.

He, C., Z. Wang, and W. Yao (2007), Frictional sliding of gabbro gouge under hydrothermal conditions, *Tectonophysics*, *445*(3), 353-362, doi:https://doi.org/10.1016/j.tecto.2007.09.008.

He, C., W. Yao, Z. Wang, and Y. Zhou (2006), Strength and stability of frictional sliding of gabbro gouge at elevated temperatures, *Tectonophysics*, *427*(1), 217-229, doi:https://doi.org/10.1016/j.tecto.2006.05.023.

Ikari, M. J., C. Marone, and D. M. Saffer (2011), On the relation between fault strength and frictional stability, *Geology*, *39*(1), 83-86, doi:10.1130/g31416.1.

Ikari, M. J., C. Marone, D. M. Saffer, and A. J. Kopf (2013), Slip weakening as a mechanism for slow earthquakes, *Nature Geoscience*, *6*(6), 468-472, doi:10.1038/ngeo1818.

Ikari, M. J., F. K. Wilckens, and D. M. Saffer (2020), Implications of basement rock alteration in the Nankai Trough, Japan for subduction megathrust slip behavior, *Tectonophysics*, *774*, 228275, doi:https://doi.org/10.1016/j.tecto.2019.228275.

Ito, Y., & Ikari, M. J. (2015). Velocity-and slip-dependent weakening in simulated fault gouge: Implications for multimode fault slip. *Geophysical Research Letters*, *42*(21), 9247-9254.

Iverson, R. M., Dzurisin, D., Gardner, C. A., Gerlach, T. M., LaHusen, R. G., Lisowski, M., ... & Vallance, J. W. (2006). Dynamics of seismogenic volcanic extrusion at Mount St Helens in 2004–05. *Nature*, *444*(7118), 439-443.

Karner, S. L., & Marone, C. (2001). Fractional restrengthening in simulated fault gouge: Effect of shear load perturbations. *Journal of Geophysical Research: Solid Earth*, *106*(B9), 19319-19337.

Kaneko, Y., Avouac, J. P., & Lapusta, N. (2010). Towards inferring earthquake patterns from geodetic observations of interseismic coupling. *Nature Geoscience*, *3*(5), 363-369, doi:10.1038/ngeo843.

Kelemen, P., Benson, S. M., Pilorgé, H., Psarras, P., & Wilcox, J. (2019). An overview of the status and challenges of CO_2 storage in minerals and geological formations. *Frontiers in Climate*, *1*, 9.

Klein, F. W. (2016). Lithospheric flexure under the Hawaiian volcanic load: Internal stresses and a broken plate revealed by earthquakes. *Journal of Geophysical Research: Solid Earth*, *121*(4), 2400-2428.

Klein, F. W., Koyanagi, R. Y., Nakata, J. S., & Tanigawa, W. R. (1987). The seismicity of Kilauea's magma system. *Volcanism in Hawaii*, *2*, 1019-1185.

Khodayar, M., & Einarsson, P. (2002). Strike-slip faulting, normal faulting, and lateral dike injections along a single fault: Field example of the Gljúfurá fault near a Tertiary oblique rift-transform zone, Borgarfjörður, west Iceland. *Journal of Geophysical Research: Solid Earth*, *107*(B5), ETG-5.

Kristmannsdóttir, H. (1979). Alteration of basaltic rocks by hydrothermal-activity at 100-300 C. In *Developments in sedimentology* (Vol. 27, pp. 359-367). Elsevier.

Lengliné, O., Marsan, D., Got, J. L., Pinel, V., Ferrazzini, V., & Okubo, P. G. (2008). Seismicity and deformation induced by magma accumulation at three basaltic volcanoes. *Journal of Geophysical Research: Solid Earth*, *113*(B12).

Lin, G., & Okubo, P. G. (2020). Seismic Evidence for a Shallow Detachment Beneath Kīlauea's South Flank During the 2018 Activity. *Geophysical Research Letters*, *47*(15), e2020GL088003.

Lockwood, J. P., J. J. Dvorak, T. T. English, R. Y. Koyanagi, A. T. Okamura, M. L. Summers, and W. R. Tanigawa (1987), Mauna-Loa 1974–1984: A decade of intrusive and extrusive activity, in Volcanism in Hawaii, U. S. Geol. Surv. Prof. Pap., 1350, 537– 570.

Logan, J. M. (1979). Experimental studies of simulated gouge and their application to studies of natural fault zones. In *Proceedings of conference VIII-analysis of actual fault zones in bedrock* (pp. 305-343).

Logan, J. M., Dengo, C. A., Higgs, N. G., & Wang, Z. Z. (1992). Fabrics of experimental fault zones: Their development and relationship to mechanical behavior. In *International geophysics* (Vol. 51, pp. 33-67). Academic Press, doi: https://doi.org/10.1016/S0074-6142(08)62814-4.

Logan, J. M., and K. A. Rauenzahn (1987), Frictional dependence of gouge mixtures of quartz and montmorillonite on velocity, composition and fabric, *Tectonophysics*, *144*(1), 87-108, doi:https://doi.org/10.1016/0040-1951(87)90010-2.

Mair, K., and C. Marone (1999), Friction of simulated fault gouge for a wide range of velocities and normal stresses, *Journal of Geophysical Research: Solid Earth*, *104*(B12), 28899-28914, doi:10.1029/1999jb900279.

Marone, C. (1998a), The effect of loading rate on static friction and the rate of fault healing during the earthquake cycle, *Nature*, *391*(6662), 69-72, doi:10.1038/34157.

Marone, C. (1998b), Laboratory-derived friction laws and their application to seismic faulting, *Annual Review of Earth and*

Planetary Sciences, *26*(1), 643-696, doi:10.1146/annurev.earth.26.1.643.

Marone, C., and S. J. D. Cox (1994), Scaling of rock friction constitutive parameters: The effects of surface roughness and cumulative offset on friction of gabbro, *pure and applied geophysics*, *143*(1), 359-385, doi:10.1007/BF00874335.

Marone, C., and B. Kilgore (1993), Scaling of the critical slip distance for seismic faulting with shear strain in fault zones, *Nature*, *362*(6421), 618-621, doi:10.1038/362618a0.

Marone, C., C. B. Raleigh, and C. H. Scholz (1990), Frictional behavior and constitutive modeling of simulated fault gouge, *Journal of Geophysical Research: Solid Earth*, *95*(B5), 7007-7025, doi:10.1029/JB095iB05p07007.

McGrail, B. P., Schaef, H. T., Ho, A. M., Chien, Y. J., Dooley, J. J., & Davidson, C. L. (2006). Potential for carbon dioxide sequestration in flood basalts. *Journal of Geophysical Research: Solid Earth*, *111*(B12).

McGrail, B. P., F. A. Spane, E. C. Sullivan, D. H. Bacon, and G. Hund (2011), The Wallula basalt sequestration pilot project, *Energy Procedia*, *4*, 5653-5660, doi:10.1016/j.egypro.2011.02.557.

Mitchell, E. K., Fialko, Y., & Brown, K. M. (2015). Frictional properties of gabbro at conditions corresponding to slow slip events in subduction zones. *Geochemistry, Geophysics, Geosystems*, *16*(11), 4006-4020, doi:10.1002/2015gc006093.

Moore, P., N. R. Iverson, and R. M. Iverson (2008), Frictional properties of the Mount St. Helens gouge, *A Volcano Rekindled: The Renewed Eruption of Mount St. Helens, 2004-2006*, *1750*, 415-424.

Nielsen, S., Spagnuolo, E., & Violay, M. (2012). Composite sample mount assembly (SAMOA): The ultimate sample preparation for rotary shear experiments. *INGV Rapporti Tecnici. ISSN*, 2039-741.

Niemeijer, A., Di Toro, G., Nielsen, S., & Di Felice, F. (2011). Frictional melting of gabbro under extreme experimental conditions of normal stress, acceleration, and sliding velocity. *Journal of Geophysical Research: Solid Earth*, *116*(B7), doi:10.1029/2010jb008181.

Niemeijer, A. R., and R. L. M. Vissers (2014), Earthquake rupture propagation inferred from the spatial distribution of fault rock frictional properties, *Earth and Planetary Science Letters*, *396*, 154-164, doi:https://doi.org/10.1016/j.epsl.2014.04.010.

Reidel, S. P., Camp, V. E., Tolan, T. L., Kauffman, J. D., & Garwood, D. L. (2013). Tectonic evolution of the Columbia River flood basalt province. *Geological Society of America Special Papers*, *497*, 293-324, doi:10.1130/2013.2497(12).

Reinen, L. A., and J. D. Weeks (1993), Determination of rock friction constitutive parameters using an iterative least squares inversion method, *Journal of Geophysical Research: Solid Earth*, *98*(B9), 15937-15950, doi:10.1029/93JB00780.

Rice, J. R., and A. L. Ruina, Stability of steady frictional slipping, J. Appl. Mech., 50, 343-349, 1983.

Richardson, E., and C. Marone (1999), Effects of normal stress vibrations on frictional healing, *Journal of Geophysical Research: Solid Earth*, *104*(B12), 28859-28878, doi:10.1029/1999jb900320.

Ruina, A. L. (1983), Slip instability and state variable friction laws, *Journal of Geophysical Research: Solid Earth*, *88*(B12), 10359-10370, doi:10.1029/JB088iB12p10359.

Saffer, D.M., Marone, C., (2003). Comparison of smectite- and illite-rich gouge frictional properties: application to the updip limit of the seismogenic zone along subduction megathrust. *Earth Planet. Sci. Lett.* (215), 219–235. https://doi.org/10.1016/S0012-821X(03)00424-2.

Samuelson, J., D. Elsworth, and C. Marone (2009), Shear-induced dilatancy of fluid-saturated faults: Experiment and theory, *Journal of Geophysical Research*, *114*(B12), doi:10.1029/2008jb006273.

Scholz, C. H. (2000). Evidence for a strong San Andreas fault. *Geology*, *28*(2), 163-166, doi:10.1130/0091-7613(2000)28<163:EFASSA>2.0.CO.

Scholz, C. H. (2002), *The Mechanics of Earthquakes and Faulting*, 2 ed., Cambridge University Press, Cambridge, doi:DOI: 10.1017/CBO9780511818516.

Scholz, C., P. Molnar, and T. Johnson (1972), Detailed studies of frictional sliding of granite and implications for the earthquake mechanism, *Journal of geophysical research*, *77*(32), 6392-6406.

Scott, D. R., C. J. Marone, and C. G. Sammis (1994), The apparent friction of granular fault gouge in sheared layers, *Journal*

of Geophysical Research: Solid Earth, *99*(B4), 7231-7246, doi:10.1029/93jb03361.

Scuderi, M. M., C. Collettini, C. Viti, E. Tinti, and C. Marone (2017), Evolution of shear fabric in granular fault gouge from stable sliding to stick slip and implications for fault slip mode, *Geology*, doi:10.1130/g39033.1.

Scuderi, M. M., A. R. Niemeijer, C. Collettini, and C. Marone (2013), Frictional properties and slip stability of active faults within carbonate–evaporite sequences: The role of dolomite and anhydrite, *Earth and Planetary Science Letters*, *369-370*, 220-232, doi:10.1016/j.epsl.2013.03.024.

Shimamoto, T., & Tsutsumi, A. (1994). A new rotary-shear high-speed frictional testing machine: Its basic design and scope of research (in Japanese with English abstract). *Journal of Tectonic Research Group of Japan*, *39*, 65–78.

Snæbjörnsdóttir, S. Ó., B. Sigfússon, C. Marieni, D. Goldberg, S. R. Gislason, and E. H. Oelkers (2020), Carbon dioxide storage through mineral carbonation, *Nature Reviews Earth & Environment*, *1*(2), 90-102, doi:10.1038/s43017-019-0011-8.

Tesei, T., B. M. Carpenter, C. Giorgetti, M. M. Scuderi, A. Sagy, P. Scarlato, and C. Collettini (2017), Friction and scale-dependent deformation processes of large experimental carbonate faults, *Journal of Structural Geology*, *100*, 12-23, doi:10.1016/j.jsg.2017.05.008.

Villani, F., Pucci, S., Azzaro, R. *et al.* Surface ruptures database related to the 26 December 2018, M$_W$ 4.9 Mt. Etna earthquake, southern Italy. *Sci Data* **7,** 42 (2020). https://doi.org/10.1038/s41597-020-0383-0.

Violay, M., S. Nielsen, B. Gibert, E. Spagnuolo, A. Cavallo, P. Azais, S. Vinciguerra, and G. Di Toro (2013a), Effect of water on the frictional behavior of cohesive rocks during earthquakes, *Geology*, *42*(1), 27-30, doi:10.1130/g34916.1.

Violay, M., S. Nielsen, E. Spagnuolo, D. Cinti, G. Di Toro, and G. Di Stefano (2013b), Pore fluid in experimental calcite-bearing faults: Abrupt weakening and geochemical signature of co-seismic processes, *Earth and Planetary Science Letters*, *361*, 74-84, doi:10.1016/j.epsl.2012.11.021.

Walker, R. J., R. E. Holdsworth, P. J. Armitage, and D. R. Faulkner (2013a), Fault zone permeability structure evolution in basalts, *Geology*, *41*(1), 59-62, doi:10.1130/g33508.1.

Walker, R., R. Holdsworth, J. Imber, and D. Ellis (2012), Fault-zone evolution in layered basalt sequences: A case study from the Faroe Islands, NE Atlantic margin, *Geological Society of America Bulletin*, *124*, 1382-1393, doi:10.1130/B30512.1.

Walker, R. J., R. E. Holdsworth, J. Imber, D. R. Faulkner, and P. J. Armitage (2013b), Fault zone architecture and fluid flow in interlayered basaltic volcaniclastic-crystalline sequences, *Journal of Structural Geology*, *51*, 92-104, doi:https://doi.org/10.1016/j.jsg.2013.03.004.

Weeks, J. D. (1993), Constitutive laws for high-velocity frictional sliding and their influence on stress drop during unstable slip, *Journal of Geophysical Research: Solid Earth*, *98*(B10), 17637-17648, doi:10.1029/93JB00356.

Wong Tf, Gu Y, Yanagidani T, Zhao Y. 1992. Stabilization of faulting by cumulative slip. In *Fault Mechanics and Transport Properties of Rock*, ed. B Evans, Tf Wong, pp. 119–43. London: Academic

Zhang, L., C. He, Y. Liu, and J. Lin (2017), Frictional properties of the South China Sea oceanic basalt and implications for strength of the Manila subduction seismogenic zone, *Marine Geology*, *394*, 16-29, doi:10.1016/j.margeo.2017.05.006.

3. Frictional instabilities and carbonation of basalts triggered by injection of pressurized H_2O- and CO_2- rich fluids

Piercarlo Giacomel[1,2] , Elena Spagnuolo[3] , Manuela Nazzari[3,4], Andrea Marzoli[1] , François Passelegue[5], Nasrrddine Youbi[6,7] , and Giulio Di Toro[1,3]

[1]Dipartimento di Geoscienze, Università degli Studi di Padova, Padua, Italy

[2]Now at Dipartimento di Scienze della Terra, Sapienza Università di Roma, Rome, Italy

[3]Istituto Nazionale di Geofisica e Vulcanologia, Rome, Italy

[4]Dipartimento di Scienze della Terra, Sapienza Università di Roma, Rome, Italy

[5]LEMR, IIC, ENAC, EPFL, Lausanne, Switzerland

[6]Geology Department, Faculty of Sciences-Semlalia, Cadi Ayyad University, Marrakech, Morocco

[7]Instituto Dom Luiz, Faculdade de Ciências, Universidade de Lisboa, Lisbon, Portugal

AUTHOR CONTRIBUTIONS

PG wrote the first version of the manuscript. PG, GDT, ES and MN conceived the idea and the experiments. AM and NY collected CAMP samples. PG performed the geochemical, mineral, and petrographic analyses. ES, PG and MN performed the experiments. PG, ES, GDT, MN, FP and AM analyzed the data. All authors contributed to the final version of the manuscript.

ABSTRACT

The safe application of geological carbon storage depends also on the seismic hazard associated with fluid injection. In this regard, we performed friction experiments under constant shear stress using a rotary shear apparatus on precut basalts with variable degree of hydrothermal alteration by injecting distilled H_2O, pure CO_2, and $H_2O + CO_2$ fluid mixtures under temperature, fluid pressure, and stress conditions relevant for large-scale subsurface CO_2 storage reservoirs. In all experiments, seismic slip was preceded by short-lived slip bursts. Seismic slip occurred at equivalent fluid pressures and normal stresses, thus at comparable effective normal stresses regardless of the fluid injected and degree of alteration of basalts. Injection of fluids caused also carbonation reactions and crystallization of new dolomite grains in the basalt-hosted faults sheared in $H_2O + CO_2$ fluid mixtures. Fast mineral carbonation in the experiments might be explained by shear heating during seismic slip, evidencing the high chemical reactivity of basalts to $H_2O + CO_2$ mixtures.

PLAIN LANGUAGE SUMMARY

The injection of H_2O+CO_2 mixtures in basalts has been proposed for CO_2 storage as an appealing option to the injection of CO_2 fluids. In fact, H_2O+CO_2 fluids should react with basalts and induce the precipitation of carbonate minerals. The huge advantage of this storage technique is that, by *turning CO_2 into rock* (New York Times 9/2/2015), it prevents the risk of CO_2 leakage driven by buoyancy forces in the storage site. However, though it is well known that fluid injection may induce seismicity (e.g., Ellsworth, Science, 2013), the frictional behavior of faults in basalts injected by H_2O+CO_2 fluids is still poorly known. To provide insights on the induced-seismicity potential of this CO_2 storage technique, we reproduced the ambient conditions of typical H_2O+CO_2 storage sites by exploiting the rotary shear apparatus Slow to High Velocity Apparatus (INGV-Rome, Italy). Our experimental results show that fluid composition and degree of alteration of basalts had a negligible role in controlling the maximum fluid pressure that the experimental fault can sustain before failure. Evidence for mineral carbonation after the experiments sheared with CO_2-rich water attest the high chemical reactivity of basalts in acidic environment.

3.1 INTRODUCTION

Reducing the concentration of CO_2 in the atmosphere is among the greatest challenges of the present century. Large-scale carbon capture and geological storage have been proposed to reach this target (*Bachu et al.*, 2007; *Matter & Kelemen*, 2009). One way to provide a long-lasting, thermodynamically stable, and environmentally benign carbon storage is through mineral carbonation (*Oelkers et al.*, 2008). This process requires combining CO_2-rich water with dissolved divalent cations (primarily Ca^{2+}, Mg^{2+}, and Fe^{2+}) to precipitate carbonate minerals. The most efficient sources of divalent cations are silicate minerals like olivine, plagioclase, and pyroxenes, that is, the main constituents of basaltic rocks such as those of continental flood basalts. In particular, dissolution of CO_2 into water during its injection into basalt hosted reservoirs enhances the geological storage security compared to conventional geological formations, such as saline aquifers. In fact, injection of fully pre-dissolved CO_2 mitigates the risks of fluid leakage driven by buoyancy forces back to the surface, so that injection could take place at shallower depth than those where CO_2 behaves as supercritical (usually <1,000 m, depending on the geothermal gradient; e.g., *Edlmann et al.*, 2013). Moreover, CO_2-rich water interaction with pyroxene, olivine, etc., in basalts accelerates dissolution-carbonation reactions, thus mineral trapping (*Aradóttir et al.*, 2012; *Matter et al.*, 2016). However, the amount of dissolved CO_2 at operative depths typical for carbon sequestration into basaltic aquifers (*Alfredsson et al.*, 2013) is in the ratio 30–70 g CO_2 per kg H_2O (*Choi & Nešić*, 2011). Consequently, the large amounts of water to be injected during subsurface CO_2 storage efforts may trigger earthquakes in response to pore fluid overpressures in the vicinity of preexisting faults (*Zoback & Gorelick*, 2012).

Specifically, injection of pressurized CO_2-rich fluids affects the shear strength of faults by (1) mechanical effects due to the increase in pore fluid pressure (*Hubbert & Rubey*, 1959) and (2) a variety of coupled chemically mediated mechanical processes, which may render faults more prone to frictional instabilities (*Rohmer et al.*, 2016, and references therein for an overall overview). While the effect of water-rich fluids on fault reactivation has been studied extensively, the mechanical behavior of faults submitted to injections of CO_2-rich fluids as well as the effect of the degree of alteration of rocks on the dynamics of the onset of slip

remains largely unknown. So far, most experimental studies have addressed the effects of the short-term (i.e., timescale of laboratory experiments: hours to days) and of the long-term (timescales over 100 years, up to 10 kyr) exposure to CO_2-rich water (brine) on the frictional properties of faults and fractures hosted in conventional sandstone reservoirs (*Bakker et al.*, 2016; *Samuelson & Spiers*, 2012) and in anhydrite and claystone caprocks (e.g., *Pluymakers et al.*, 2014). Nonetheless, a knowledge gap regarding the frictional behavior in shallower alternative CO_2 storage systems, involving injection of CO_2-rich water in basaltic reservoirs, still exists. Since hydrothermally altered basaltic rocks may be chosen as suitable CO_2 storage reservoirs, the study of the frictional behavior of basaltic rocks with variable degree of alteration in the presence of pressurized CO_2 and H_2O + CO_2 fluids is of paramount importance.

Here we investigated the role of H_2O- and CO_2-rich pressurized fluids on the triggering of frictional instabilities of preloaded experimental faults in basalts. The experiments were designed to reproduce the rock-type and the ambient conditions relevant for Hellisheidi (Iceland) CO_2-injection site (CarbFix pilot project: *Gislason & Oelkers*, 2014; *Gislason et al.*, 2010). In fact, to date, this is the first storage site in which CO_2 is dissolved in H_2O before being injected in a basalt-built reservoir. The reservoir is located in a low-temperature geothermal area at ~500 m depth, corresponding to a lithostatic pressure of about 15 MPa, and at ~25°C ambient temperature (*Alfredsson et al.*, 2013). Our results that could apply to other voluminous basaltic occurrences (e.g., continental flood basalts sequences) show that fault instability nucleation occurs regardless of the state of alteration of basalts and chemical composition of injection fluids.

3.2 METHODS

3.2.1 Sample Selection and Petrography

Thick lava sequences pertaining to the Central Atlantic magmatic province (CAMP: *Goldberg et al.*, 2010) or the Columbia River basalts (Wallula pilot project: *McGrail et al.*, 2006, 2011) have been proposed as suitable CO_2-storage targets. Therefore, we selected representative samples of these two continental basalt provinces. For the CAMP, basaltic lava flows and shallow intrusions (sills) were collected in Morocco (*Marzoli et al.*, 2004), eastern North America (*Merle et al.*, 2014), and Portugal (*Callegaro et al.*, 2014). The selected samples have an average grain size of 100–300 µm and a maximum grain size <2 mm. The main primary minerals of unaltered continental flood basalts are Ca-rich plagioclase (~45–50 vol %), clinopyroxene (augite and/or pigeonite, ~40–45 vol %), and Fe-Ti oxides (~5 vol%); some samples contain up to ~5 vol% of sideromelane glass. Since the rock-forming minerals of non-altered basalts are water free, the loss on ignition content (LOI or the weight loss measured after heating the sample at 1000°C for 24 hr) is a good proxy of the abundance of breakdown products (smectite, sericite, etc.) and of the degree of alteration of the basalt. A systematic analysis of the LOI values revealed different alteration state of the selected basalts (Table S3.1 in the supporting information), as confirmed by the variable modal content of secondary minerals such as phyllosilicates (sericite, smectite, illite, and chlorite) deriving from alteration of plagioclase and pyroxenes, and from devitrification of sideromelane (optical microscope analysis and bulk X-ray powder diffraction; Figures S3.1 and S3.2), which amounts to ~50 vol % in the most altered specimens. Hereinafter, the basaltic rocks are referred to as "unaltered" when their LOI is below 1.7% wt. and the amount of alteration minerals is less than 5% in volume, and *vice versa* as "altered" (see Figures S3.1 and S3.3 for details).

### 3.2.2. Experimental and Analytical Methods

To investigate the effect of short-term fluid-rock interaction on the mechanical behavior of basalt-built faults, 20 friction experiments were performed with the rotary shear apparatus SHIVA (Slow to High Velocity Apparatus; Table S3.2) installed at the Istituto

Nazionale di Geofisica e Vulcanologia in Rome (Italy; *Di Toro et al.*, 2010; *Niemeijer et al.*, 2011). The experiments were performed on hollow cylinders 30/50 mm internal/external diameter of the continental flood basalts described in section 3.2.1. The mineral and chemical compositions of the basalts were determined with X-ray powder diffraction (PANalytical X'Pert PRO) and X-ray fluorescence (WDS Philips PW2400) installed at Padua University. The effective porosity (< 1%) was determined with a Helium-pycnometer Accu Pyc II 1340. Samples were jacketed in aluminum ring and embedded in epoxy to ensure the fluid pressure sealing as described in *Nielsen et al.* (2012). Bare surfaces were ground flat and parallel with a surface grinder to impose the same roughness on all sample assemblages (wavelength of ~50 μm and height of ~10 μm: e.g., *Passelègue et al.*, 2016). This procedure ensures in most cases sample misalignment smaller than 100 μm once the rock specimens are installed in SHIVA. The sample pair was inserted in a vessel allowing pressurized fluid confinement (Figure S3.4; *Violay et al.*, 2013, 2014). The injected fluids consisted of distilled H_2O, pure CO_2, pure argon, and a mixture of $H_2O + CO_2$. We used three different pressurizing circuits depending on the composition of the fluid (Text S3.1). Normal stress σ_n, fluid pressure Pf, axial shortening, equivalent slip δ, slip velocity V, and shear stress τ (determined on the annular samples; see *Shimamoto & Tsutsumi*, 1994) were acquired at a frequency up to 250 Hz. To assess the role of the chemistry of the injected fluids on the reactivation of faults juxtaposing basalts with variable degree of hydrothermal alteration, the frictional experiments were conducted over a range of σ_n from 10 to 20 MPa, at a starting fluid pressure Pf_i from 0.5 to 5 MPa. Injection of fluids initiated under a constant shear stress τ equal to 5 MPa (Table S3.2).

Notably, to approach the CarbFix reservoir working conditions, several tests were performed by applying σ_n = 15 MPa and an initial Pf = 2.5 MPa at room temperature (T ~ 20–25°C; *Alfredsson et al.*, 2013). The experimental procedure consisted of the following steps: first we inserted the sample inside the pressure vessel and pumped the fluid to 0.1 MPa. Then we increased (1) σ_n up to target stress value σ_n, target; (2) Pf up to the starting

fluid pressure *Pfi*, under drained conditions (Text S3.1 and Figure S3.4); and (3) τ in three steps of 1.67 MPa every 100 s up to 5 MPa (Figure 3.1). After this stage, σ_n and τ were kept constant during the entire duration of the experiment (the recording rate of the inverter/controller feedback loop system used to control the shear stress applied from the brushless engine was 16 kHz). Lastly, the *Pfi* was increased of Δ*Pf* = 0.1 MPa every ~100 s to trigger the main fault instability resulting in a seismic slip event limited to *V* = 0.3 m/s. A time step of 100 s was sufficient to guarantee fluid penetration within the entire fault slipping zone (*Spagnuolo et al.*, 2018).
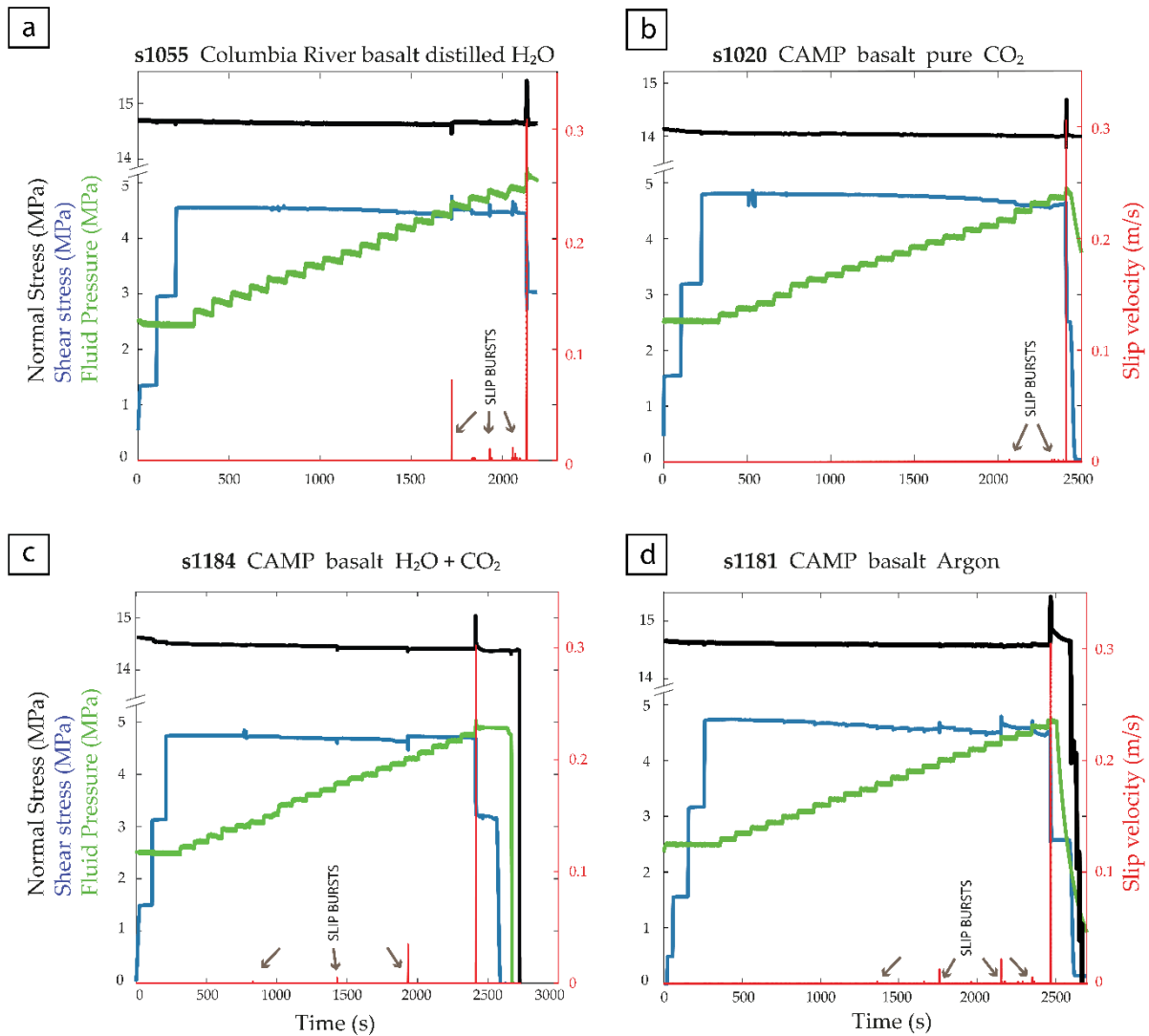

Figure 3.1. Experiments conducted under fluid pressure control at constant τ (blue in color curve) and σ_n (black curve) for **(a)** distilled H_2O, **(b)** pure CO_2, **(c)** $H_2O + CO_2$ mixture, and **(d)** pure argon. In all the experiments the *Pf* (green curve) was increased stepwise to trigger the main instability MI. Short lived slip bursts (grey arrows in the red curve), occurred before the onset of the MI. At MI the slip velocity was limited to 0.3 m/s.

3.3 RESULTS

3.3.1 Mechanical Data

In Figure 3.1 we report the evolution of the σ_n, Pf, τ, and V with time during experiments conducted with the different fluids tested (H_2O, CO_2, $H_2O + CO_2$, and Argon in respectively Figures 3.1a–3.1d). Before the main instability, the stepwise Pf increase resulted in the onset of short-lived spontaneous slip bursts (grey arrows in Figure 3.1) with V ranging from 10^{-3} m/s up to 0.3 m/s at the main instability. Slower slip rate burst events ($V < 10^{-3}$ m/s), if present, were not distinguishable from the background noise and creep. The precursory slip bursts resulted in minor shear stress drops ($\Delta\tau < 0.2$ MPa) followed by fault restrengthening (Figure 3.1). The experiment ended with the main frictional instability, or the slip event during which the fault strength dropped rapidly and accelerates up to 0.3 m/s due to the onset of macroscopic fault reactivation. The fluid pressure and normal stress at the onset of the main instability were defined as Pf_{MI} and σ_{nMI}, respectively, and are shown in Table S3.2 and Figure 3.2 for all conditions tested.

We tested the dependence of the frictional properties from *(1)* the degree of alteration of rocks and *(2)* fluid composition, by combining basalts with variable LOI wt% content in the experimental fault pair. Moreover, as altered minerals (smectite, etc.) and glass have a lower indentation hardness than primary rock-forming minerals (*Beeler et al.*, 2008), we tested the hypothesis that the most altered sample (i.e., the one with the highest LOI) of each pair determines the macroscopic properties of the experimental fault. Accordingly, we defined basalt-faults as unaltered when the LOI of the most altered samples of the fault pairs is below 1.7% wt and altered for LOI > 1.7% wt.
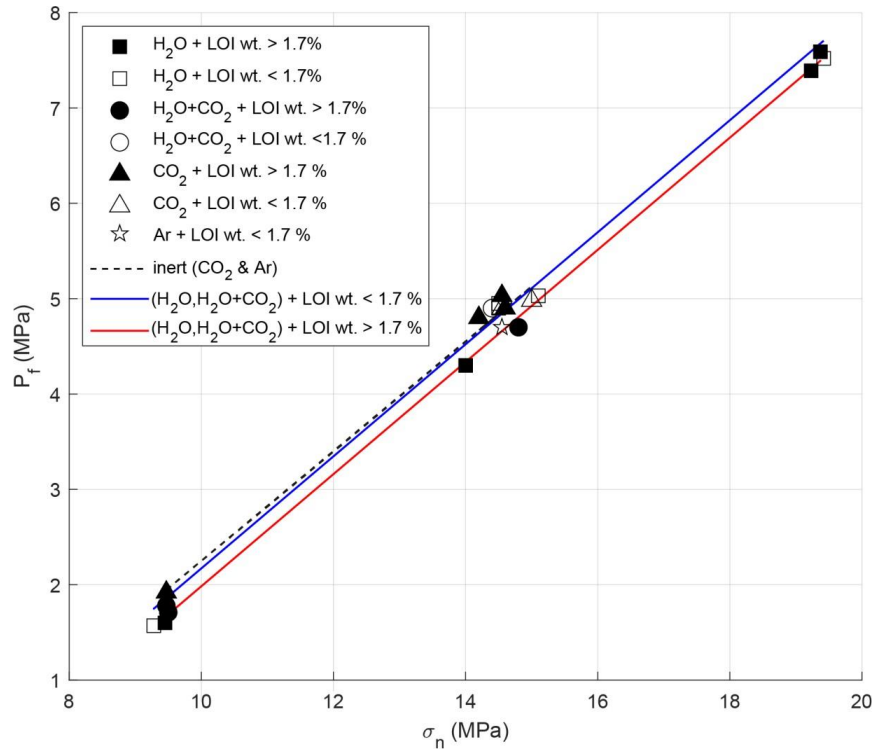
Figure 3.2. Dependence of the main frictional instability (MI) on the fluid pressure at a given normal stress, with fluid composition and LOI (wt %) content of the most altered samples of the fault pairs (i.e., the ones with the highest LOI; see section 3.3.1). The black, red, and blue best fit lines are obtained by linear regression of the plotted Pf MI-σ_n MI data of the experiments sheared in CO_2 and Ar, H_2O, and $H_2O + CO_2$ with LOI > 1.7%, and in H_2O and $H_2O + CO_2$ with LOI < 1.7%, respectively. Experimental errors are smaller than symbol size.
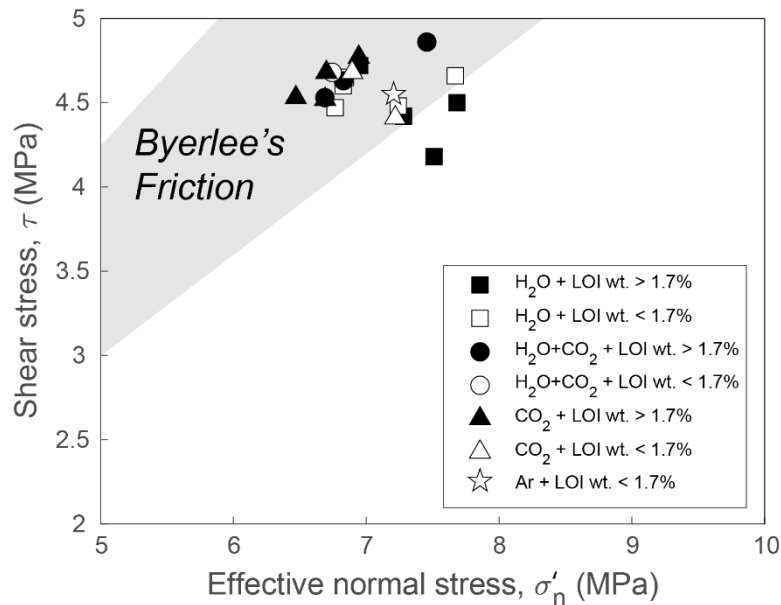
Figure 3.3. Frictional properties of bare rock surfaces employed in our tests with variable degree of alteration, interacting with pressurized fluids (Ar, CO_2, water, and CO_2-rich water). With only few exceptions, data points fall within the Byerlee's friction region, clustered in a limited Mohr-Coulomb space.

67

Independently of the tested environmental conditions (i.e., initial state of stress, nature of the fluids, and degree of alteration), fault reactivation follows the Terzaghi's principle (*Terzaghi*, 1925). The larger the normal stress acting on the experimental fault, the larger the fluid pressure required to trigger the main frictional instability (Table S3.2 and Figure 3.2). All the experimental data, with few exceptions, fell within a narrow band delimited by two straight parallel best fit lines in the *Pf_{MI}*-$\sigma_{n\,MI}$ space (Figure 3.2). The blue and red lines are the trends associated to unaltered and altered basalt-built faults, respectively, sheared either in distilled H_2O or H_2O + CO_2, whereas the black dashed best fit line refers to all the experimental faults (independently of their LOI wt % content), interacting with pure CO_2 or Ar. The best fit lines arise from a linear regression analysis, and their high R^2 values (0.987–0.999) reflect the low scatter of the experimental data and the robustness of the fits. Two observations arise: (1) the blue straight line almost overlaps with the black line in the σ_n range 9–15 MPa, attesting that unaltered basalt-built faults sheared in H_2O and H_2O + CO_2 reactivate at comparable fluid pressures as in the case of basalts pressurized with pure CO_2 or Ar, and (2) for a given normal stress at main instability, unaltered and altered basalt-built faults flooded with H_2O and H_2O + CO_2, reactivate at comparable fluid pressures (the *Pf_{MI}* difference between the red and blue best fit trends is ~0.3 MPa).

To display the mechanical data at the main instability in the Mohr-Coulomb space as in Figure 3.3, the contribution of fluid pressure on the normal stress deriving from the sample geometry and size needs to be explicated. In doing so, we developed an experimentally-derived geometric model (see Appendix 1 for details), so that the effective normal stress becomes:

Eq. (3.1) $$\sigma'_n = N/Ar - Pf\,(\xi + 1) = \sigma_n - Pf\,(\xi + 1)$$

where the ratio between the applied normal load, N, and the nominal contact area of the hollow cylinders, Ar, gives the recorded normal stress, σ_n; ξ is the geometrical correction which amounts to 0.5625 when employing hollow cylinders with internal/external diameter of 30/50 mm. Overall, data are clustered in a narrow region under the Byerlee's friction,

hence bounded by a friction coefficient range, 0.6 < μ < 0.85 (Figure 3.3) (*Byerlee*, 1978). Our findings point to a similar mechanical behavior of basalt bare surfaces at the tested conditions, independently of their alteration state and the composition of the injected fluid.

3.3.2. Microstructural and Microanalytical Data

The slipping zone of all the sheared samples consisted of lineated principal slip surfaces overlaying <100 μm thick gouge layers. However, in the experiments performed in the presence of water-rich fluids, only cohesive gouge was preserved after the tests, as most of the gouge layer was flushed away during the sample recovery. The slipping zone resulted from abrasive and adhesive wear of the basalts during sliding (Figure 3.4a). Systematic micro-Raman investigation of the slipping fault patches interested by grain size reduction and adhesive wearing, evidenced the occurrence of micrometric crystals of dolomite only in the case of basalts sheared in H_2O + CO_2 fluids (Figures 3.4b–e). Ion-chromatography analysis showed that given the similar degree of alteration of the basalts, fluids recovered after experiments performed with H_2O + CO_2 mixtures had higher concentration of Mg^{2+} compared to the fluids from experiments with distilled H_2O (e.g., s1055 versus s1184; Table S3.3). Since both fault sides contribute to cation release during shearing, the composition of the recovered fluid was related to the average of the LOI content of the sample pair forming the experimental fault.
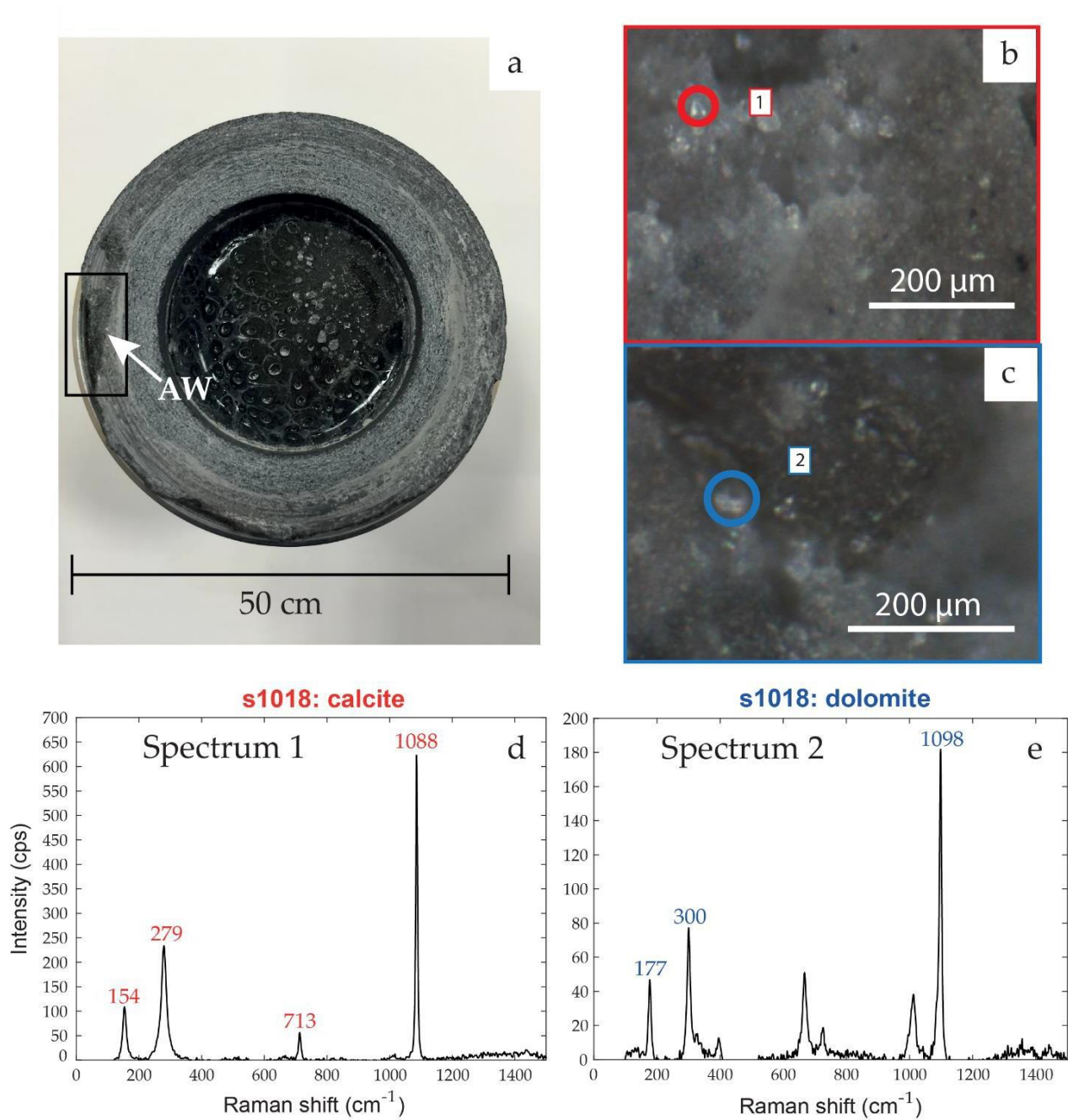
Figure 3.4. Cohesive slip surfaces of the experimental faults and evidence of carbonation of basalts. **(a)** Slip surface of a basalt sheared in $H_2O + CO_2$ mixture. Evidence of adhesive wear (AW, white arrow). During frictional sliding, especially at 0.3 m/s, wear debris remained welded to the slip surfaces. **(b)** and **(c)** Close up of the slip surface with calcite and dolomite microcrystals (Raman microprobe image). **(d)** and **(e)** Raman spectra of microcrystals of calcite and dolomite. Numbers are the characteristic intensity micro-Raman peaks of the two minerals.

3.4. DISCUSSION

3.4.1 Main Frictional Instability: Role of Fluid Composition and Degree of Alteration of Basalts

We performed friction experiments that enabled us to get better insights on the effects of the short-term exposure of H_2O- and CO_2-rich fluids with variably hydrothermally altered basalt-built preloaded faults. Clay minerals like smectite and illite and other phyllosilicates are the typical breakdown products of altered basalt. Their mechanical (e.g., pore fluid pressure) and chemical (e.g., subcritical crack growth and water adsorption) interaction with fluids is expected to reduce the fault frictional strength (*Moore & Lockner*, 2007; *Remitti et al.*, 2015; *Wintsch et al.*, 1995).

Notably, the similar response of basalts sheared with CO_2 independently of their degree of alteration at a given σ_{nMI} suggests that pure CO_2 has mainly a mechanical effect in triggering the main instability (Figure 3.2). This hypothesis is consistent with *Wang et al.* (2013), who observed the lack of chemical reactions following anhydrous CO_2-rock interaction, and is strengthened by the test performed with Ar, which lies in the same Pf_{MI}-σ_{nMI} field as in the experiments pressurized with pure CO_2. Moreover, the best fit line for the occurrence of the main frictional instabilities for unaltered basalt-hosted faults sheared in pressurized H_2O or $H_2O + CO_2$ overlaps with the one resulting from the injection of CO_2 and Ar, suggesting that fault reactivation is mainly due to the mechanical role of the fluids (Figure 3.2). The triggering of the main frictional instabilities for altered basalt-hosted faults sheared in the presence of pressurized H_2O or $H_2O + CO_2$ required, under a given normal stress, a fluid pressure on average 0.3 MPa smaller than the one required for the unaltered samples. The offset between the two best fit lines for the main frictional instabilities for unaltered or altered faults is within the reproducibility range of laboratory data. The scatter of the experimental data could be ascribed to local heterogeneities in mineral composition and rock microstructure, as well as micrometric sample misalignments.

In fact, though the samples are carefully prepared (see details in *Nielsen et al.*, 2012), misalignments up to 100 μm between the sample pairs are extremely difficult to eliminate in quite hard rocks as basalts. Consequently, the experimental data set reported here under constant shear stress, suggests that the chemically mediated mechanical fault weakening due to short-term exposure to H_2O + CO_2 fluids can be ruled out, as the main instabilities occur at similar fluid pressures given the same applied normal stress (Figure 3.2), and more generally, at comparable effective normal stresses, independently of the composition of the injected fluids and of the degree of alteration of the basalts (Figure 3.3).
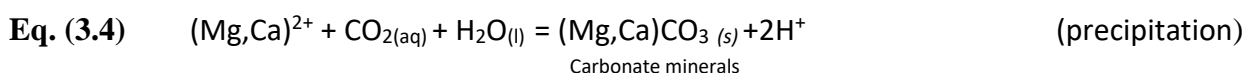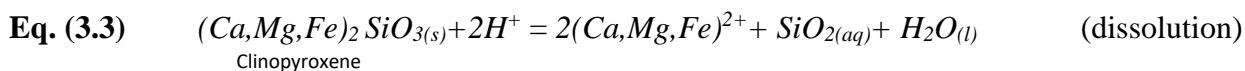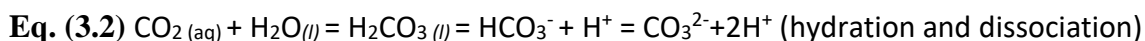
This conclusion is akin to findings from *Samuelson and Spiers* (2012), aimed at investigating the short-term impact of CO_2 exposure on the mechanical behavior of wet simulated quartz- and clay-rich gouges, whereas analogous experiments in wet-anhydrite fault gouges evidenced additional CO_2-weakening effects to that caused by water alone (*Pluymakers et al.*, 2014). Instead, despite the high chemical reactivity of basalt forming minerals in acidic environment as attested by the chemistry of the recovered fluids (Table S3.3), the presence of H_2O + CO_2-rich fluids did not entail macroscopic variations in frictional strength of faults.

Furthermore, phyllosilicates content had no significant influence on the frictional strength of the basalt hosted faults. Unfortunately, because of the design of the pressure vessel, the gouges in the slipping zones could not be recovered because flushed away with water during sample recovery. This impeded detailed microstructural analysis of the entire slipping zone. However, we argue that phyllosilicates did not form a continuous weak layer. Instead, it seems reasonable that faults accommodated deformation predominantly by cataclastic processes in all the experiments.

3.4.2 Carbonation Reactions

Newly formed dolomite grains were found only in cohesive slipping zones recovered from experiments performed in $H_2O + CO_2$ mixtures (Figure 3.4), in contrast to calcite crystals that were present in limited amounts in the starting protolith as vacuole fillings. Basalt carbonation is the result of kinetic processes involving (1) dissolution of basalt primary minerals due to interaction with acid water, (2) diffusion of the dissolved material, and (3) precipitation of carbonates. The rate-limiting step in mineral sequestration is associated to alkali earth ions availability, released from the parent minerals. Because Ca-rich clinopyroxene is the sustaining contributor of divalent cations during dissolution of basalts (*Wells et al.*, 2017), we argue that dolomite (and possibly calcite) precipitation during the $H_2O + CO_2$ tests is the result of the following reactions (*Gislason et al.*, 2010; *Aradóttir et al.*, 2011):

Eq. (3.2) $CO_{2\,(aq)} + H_2O_{(l)} = H_2CO_{3\,(l)} = HCO_3^- + H^+ = CO_3^{2-} + 2H^+$ (hydration and dissociation)

Eq. (3.3) $(Ca,Mg,Fe)_2\,SiO_{3(s)} + 2H^+ = 2(Ca,Mg,Fe)^{2+} + SiO_{2(aq)} + H_2O_{(l)}$ (dissolution)
          Clinopyroxene

Eq. (3.4) $(Mg,Ca)^{2+} + CO_{2(aq)} + H_2O_{(l)} = (Mg,Ca)CO_{3\,(s)} + 2H^+$ (precipitation)
          Carbonate minerals

According to equation (3.2), Ca^{2+} and Mg^{2+}, leached mainly from Ca-rich clinopyroxene in acid environment (equation (3.3)), react with CO_2 to precipitate calcite and dolomite (equation (3.3)). Notably, the acid environment of $H_2O + CO_2$ mixtures (pH $\simeq$ 3.2 at *Pf* = 2.5–5 MPa and 20 < *T* < 30°C, from *Diamond & Akinfiev*, 2003; Figure S3.5) promotes the release of Mg^{2+} from rock-forming basaltic minerals as showed by comparing the geochemical analysis of $H_2O + CO_2$ and distilled H_2O in basalts with similar mean LOI and cumulated slip (cf. s1055 and s1184; Table S3.3). This is corroborated by the higher Mg^{2+} concentration leached by more altered samples sheared in H_2O+CO_2 mixtures that cumulated less displacement than their counterpart with lower mean LOI and pressurized with only water

(s1018 versus s1021; Table S3.3). Moreover, as CO_2-dissolution into water can occur within 5 min during the CO_2 injection process (*Sigfusson et al.*, 2015), and the experiments last less than 1 hr, cation enrichment in solution during the stage preceding the main instability is expected to occur.

Finally, since carbonate mineral solubility decreases with increasing temperature (*Langmuir*, 1997), reaction in equation (3.4) could be favored by the temperature increase due to the frictional heat exchanged in the slipping zone during the episodic slip bursts, and especially after the main instability was achieved and the pair sample sheared at V = 0.3 m/s. The latter, together with the reduced grain size, would enhance significantly the kinetics of dissolution of basalt rock-forming minerals and precipitation of calcite and dolomite from the solution H_2O + CO_2 despite the relatively short duration of the experiment (<40 min in total).

Following the reasoning in *Kelemen et al.* (2011), assuming that basalt mineral carbonation rates are comparable to olivine carbonation rates, the optimum temperature for equation (3.4) would be in the range 15–200°C (*Kelemen & Matter*, 2008). This is in good agreement with the bulk temperature increase estimated along the slipping zone at the main frictional instability. If the heat production is (*Beeler et al.*, 2008; *Lachenbruch & Sass*, 1980):

Eq. (3.5) $$\mathrm{d}Q = \tau\, V\, \mathrm{d}t$$

an estimate of the bulk temperature increase in the slipping zone during the experiments can be computed numerically using the approximation (*Carslaw and Jaeger*, 1959) (Figure S3.6) $T(t) = \frac{1}{\rho \cdot C_p \cdot \sqrt{\kappa\pi}} \cdot \int_0^t \frac{1}{2} \cdot \frac{Q}{\sqrt{t-t'}}\, dt$ (with, for basalts, thermal diffusivity κ = 0.012 $cm^2\, s^{-1}$ (*Hanley et al.*, 1978), specific heat capacity Cp = 898 J $kg^{-1}\, K^{-1}$ (*Waples and Waples*, 2004) and density ρ = 2960 kg m^{-3}). The numerical solution revealed indeed the achievement of bulk temperatures of several hundred degrees Celsius once the main instability was triggered, as shown in Figure S3.6. In small fault patches (<1 mm^2) of the experimental fault, because of flash heating at the asperity scale or of debris trapped in the slipping zone, temperatures can be higher than

1000°C (see *Tisato et al.*, 2012, for discussion). This can also be attested by the presence of adhesive wear products, because of frictional welding between opposing asperities in the slipping zone in all the experiments and independently of the composition of the injected fluid (Figure 3.3a). Adhesive wear products were also found in experiments performed with H_2O-rich fluids, suggesting the achievement of high temperatures despite the presence of water that should buffer the temperature increase (*Violay et al.*, 2014). Furthermore, since thermal decomposition of dolomite and calcite happens at a temperature ranging from 600 to 800°C, this temperature interval can be reasonably regarded as an upper bound of the temperature reached in the slipping zone at the main frictional instability (*Rodriguez-Navarro et al.*, 2009, 2012).

The presence of newly formed dolomite grains at the end of our friction experiments supports the great effectiveness of mineral carbonation in basalts interacting with H_2O + CO_2 mixtures (e.g., *Aradóttir et al.*, 2012; *Matter et al.*, 2016). However, in our experiments and compared to natural conditions, dolomite precipitation was possibly fostered by both rapid temperature rise (up to 600–800°C) and grain comminution associated to the main fault frictional instability and simulated seismic slip. In nature, if mineral precipitation associated to seismic slip would lead to significant fault clogging, buildup of fluid pressure may occur in the vicinity of the fault, further increasing the seismic hazard.

3.5 CONCLUSIONS

We investigated the effects of the injection of pressurized fluids (Ar, CO_2, H_2O, and $H_2O + CO_2$) in preloaded basalt-built experimental faults (Figure 3.1). Experimental conditions were designed to reproduce the typical operating conditions for CO_2 storage in basaltic-built reservoirs. The pressure of the fluid to trigger the main instability scaled linearly with the normal stress acting on the fault (Figure 3.2), and notably resulted in fault activation occurring at comparable effective normal stresses under constant shear stress, regardless of the tested conditions (Figure 3.3).

Fluid composition and degree of alteration of basalts had a negligible role in controlling the maximum fluid pressure that the experimental fault could sustain before failure (i.e., main instability; Figure 3.2). In fact, more altered basalts (i.e., with higher LOI and higher content of secondary minerals such as sericite, smectite, etc.) sheared in H_2O- and $H_2O+ CO_2$-rich fluids were just slightly more prone to the main frictional instability than less altered basalts and basalts sheared in pure CO_2 and Ar (Figure 3.2). However, this tiny discrepancy may be due to local heterogeneities in mineral composition and microstructure of basaltic samples.

The evidence of newly formed dolomite grains in the slipping zones of all the basalts (i.e., independently of the alteration state) sheared in $H_2O + CO_2$ mixtures is the result of the easy release of Ca^{2+} and Mg^{2+} from basalt-bearing minerals, plus grain size reduction and heat production during frictional sliding (Figure 3.4). The experiments discussed here confirm that dissolution and mineral carbonation of basalts in the presence of $H_2O + CO_2$ mixtures is extremely efficient, also during frictional sliding at seismic slip rates (~0.3 m/s) associated to the main instability event.

ACKNOWLEDGEMENTS AND DATA POLICY

REFERENCES

Alfredsson, H. A., E. H. Oelkers, B. S. Hardarsson, H. Franzson, E. Gunnlaugsson, and S. R. Gislason (2013), The geology and water chemistry of the Hellisheidi, SW-Iceland carbon storage site, *International Journal of Greenhouse Gas Control*, *12*, 399-418, doi:10.1016/j.ijggc.2012.11.019.

Aradóttir, E. S. P., H. Sigurdardottir, B. Sigfusson, and E. Gunnlaugsson (2011), CarbFix: a CCS pilot project imitating and accelerating natural CO2 sequestration, *Greenh Gases*, *1*(2), 105-118, doi:10.1002/ghg.18.

Aradóttir, E. S. P., E. L. Sonnenthal, G. Björnsson, and H. Jónsson (2012), Multidimensional reactive transport modeling of CO2 mineral sequestration in basalts at the Hellisheidi geothermal field, Iceland, *International Journal of Greenhouse Gas Control*, *9*, 24-40, doi:10.1016/j.ijggc.2012.02.006.

Bachu, S., D. Bonijoly, J. Bradshaw, R. Burruss, S. Holloway, N. P. Christensen, and O. M. Mathiassen (2007), CO2 storage capacity estimation: Methodology and gaps, *International Journal of Greenhouse Gas Control*, *1*(4), 430-443, doi:10.1016/s1750-5836(07)00086-2.

Bakker, E., Hangx, S. J., Niemeijer, A. R., & Spiers, C. J. (2016). Frictional behaviour and transport properties of simulated fault gouges derived from a natural CO2 reservoir. *International Journal of Greenhouse Gas Control*, *54*, 70-83.

Beeler, N. M., T. E. Tullis, and D. L. Goldsby (2008), Constitutive relationships and physical basis of fault strength due to flash heating, *J Geophys Res-Sol Ea*, *113*(B1), doi:Artn B0140110.1029/2007jb004988.

Byerlee, J., 1978. Friction of rocks. Pure Appl. Geophys.116, 615–626.

Callegaro, S., et al. (2014), Enriched mantle source for the Central Atlantic magmatic province: New supporting evidence from southwestern Europe, *Lithos*, *188*, 15-32, doi:10.1016/j.lithos.2013.10.021.

Carslaw, H., and J. Jaeger (1959), *Heat in solids*, Clarendon Press, Oxford.

Choi, Y.-S., and S. Nešić (2011), Determining the corrosive potential of CO2 transport pipeline in high pCO2–water environments, *International Journal of Greenhouse Gas Control*, *5*(4), 788-797, doi:10.1016/j.ijggc.2010.11.008.

Diamond, L. W., & Akinfiev, N. N. (2003). Solubility of CO2 in water from− 1.5 to 100 C and from 0.1 to 100 MPa: evaluation of literature data and thermodynamic modelling. *Fluid phase equilibria*, *208*(1-2), 265-290.

Di Toro, G., et al. (2010), From field geology to earthquake simulation: a new state-of-the-art tool to investigate rock friction during the seismic cycle (SHIVA), *Rendiconti Lincei*, *21*(S1), 95-114, doi:10.1007/s12210-010-0097-x.

Edlmann, K., Haszeldine, S., & McDermott, C. I. (2013). Experimental investigation into the sealing capability of naturally fractured shale caprocks to supercritical carbon dioxide flow. *Environmental earth sciences*, *70*(7), 3393-3409.

Giacomel, Piercarlo; Spagnuolo, Elena; Nazzari, Manuela; Marzoli, Andrea; Passelegue, François; Youbi, Nasrrddine; Di Toro, Giulio (2018): Frictional and microstructural data of basalts sheared with pressurized H2O- and CO2- rich fluids. GFZ Data Services. http://doi.org/10.5880/fidgeo.2018.013

Gislason, S. R., & Oelkers, E. H. (2014). Carbon storage in basalt. *Science*, *344*(6182), 373-374.

Gislason, S. R., Wolff-Boenisch, D., Stefansson, A., Oelkers, E. H., Gunnlaugsson, E., Sigurdardottir, H., ... & Axelsson, G. (2010). Mineral sequestration of carbon dioxide in basalt: A pre-injection overview of the CarbFix project. *International Journal of Greenhouse Gas Control*, *4*(3), 537-545.

Goldberg, D. S., D. V. Kent, and P. E. Olsen (2010), Potential on-shore and off-shore reservoirs for CO2 sequestration in Central Atlantic magmatic province basalts, *Proc Natl Acad Sci U S A*, *107*(4), 1327-1332, doi:10.1073/pnas.0913721107.

Hanley, E., D. Dewitt, and R. Roy (1978), The thermal diffusivity of eight well-characterized rocks for the temperature range 300–1000 K, *Engineering Geology*, *12*, 31-47.

Hubbert, M. K., and W. W. Rubey (1959), Role of fluid pressure in mechanics of overthrust faulting I. Mechanics of fluid-filled porous solids and its application to overthrust faulting, *Geological Society of America Bulletin*, *70*(2), 115-166.

Kelemen, P. B., & Matter, J. (2008). In situ carbonation of peridotite for CO2 storage. *Proceedings of the National Academy of Sciences*, *105*(45), 17295-17300

Kelemen, P. B., Matter, J., Streit, E. E., Rudge, J. F., Curry, W. B., & Blusztajn, J. (2011). Rates and mechanisms of mineral carbonation in peridotite: natural processes and recipes for enhanced, in situ CO2 capture and storage. *Annual Review of Earth and Planetary Sciences*, *39*, 545-576.

Lachenbruch, A. H., and J. H. Sass (1980), Heat flow and energetics of the San Andreas Fault Zone, *Journal of Geophysical Research: Solid Earth*, *85*(B11), 6185-6222, doi:10.1029/JB085iB11p06185.

Langmuir, D. (1997). *Aqueous environmental geochemistry* (No. 551.48 L3.).

Marzoli, A., et al. (2004), Synchrony of the Central Atlantic magmatic province and the Triassic-Jurassic boundary climatic and biotic crisis, *Geology*, *32*(11), 973, doi:10.1130/g20652.1.

Matter, and P. B. Kelemen (2009), Permanent storage of carbon dioxide in geological reservoirs by mineral carbonation, *Nat Geosci*, *2*(12), 837-841.

Matter, J. M., Stute, M., Snæbjörnsdottir, S. Ó., Oelkers, E. H., Gislason, S. R., Aradottir, E. S., ... & Axelsson, G. (2016). Rapid carbon mineralization for permanent disposal of anthropogenic carbon dioxide emissions. *Science*, *352*(6291), 1312-1314.

McGrail, H. T. Schaef, A. M. Ho, Y.-J. Chien, J. J. Dooley, and C. L. Davidson (2006), Potential for carbon dioxide sequestration in flood basalts, *Journal of Geophysical Research*, *111*(B12), doi:10.1029/2005jb004169.

McGrail, F. A. Spane, E. C. Sullivan, D. H. Bacon, and G. Hund (2011), The Wallula basalt sequestration pilot project, *Energy Procedia*, *4*, 5653-5660, doi:10.1016/j.egypro.2011.02.557.

Merle, R., et al. (2014), Sr, Nd, Pb and Os Isotope Systematics of CAMP Tholeiites from Eastern North America (ENA): Evidence of a Subduction-enriched Mantle Source, *Journal of Petrology*, *55*(1), 133-180, doi:10.1093/petrology/egt063.

Moore, D. E., & Lockner, D. A. (2007). Friction of the smectite clay montmorillonite. *The seismogenic zone of subduction thrust faults*, 317-345.

Nielsen, S., Di Toro, G., Hirose, T., & Shimamoto, T. (2008). Frictional melt and seismic slip. *Journal of Geophysical Research: Solid Earth*, *113*(B1).

Nielsen, S., E. Spagnuolo, and M. Violay (2012), Composite sample mount assembly (SAMOA): the ultimate sample preparation for rotary shear experiments., *INGV Rapporti Tecnici. ISSN 2039-741*, *215*.

Niemeijer, A., G. Di Toro, S. Nielsen, and F. Di Felice (2011), Frictional melting of gabbro under extreme experimental conditions of normal stress, acceleration, and sliding velocity, *Journal of Geophysical Research*, *116*(B7), doi:10.1029/2010jb008181.

Oelkers, E. H., S. R. Gislason, and J. Matter (2008), Mineral Carbonation of CO2, *Elements*, *4*(5), 333-337, doi:10.2113/gselements.4.5.333.

Passelègue, F., Spagnuolo, E., Violay, M., Nielsen, S., Di Toro, G., & Schubnel, A. (2016). Frictional evolution, acoustic emissions activity, and off-fault damage in simulated faults sheared at seismic slip rates. *Journal of Geophysical Research: Solid Earth*, *121*(10), 7490-7513.

Pluymakers, A. M., Samuelson, J. E., Niemeijer, A. R., & Spiers, C. J. (2014). Effects of temperature and CO2 on the frictional behavior of simulated anhydrite fault rock. *Journal of Geophysical Research: Solid Earth*, *119*(12), 8728-8747.

Remitti, F., Smith, S. A. F., Mittempergher, S., Gualtieri, A. F., & Di Toro, G. (2015). Frictional properties of fault zone gouges from the J-FAST drilling project (Mw 9.0 2011 Tohoku-Oki earthquake). *Geophysical Research Letters*, *42*(8), 2691-2699.

Rodriguez-Navarro, C., Ruiz-Agudo, E., Luque, A., Rodriguez-Navarro, A. B., & Ortega-Huertas, M. (2009). Thermal decomposition of calcite: Mechanisms of formation and textural evolution of CaO nanocrystals. *American Mineralogist*, *94*(4), 578-593.

Rodriguez-Navarro, C., Kudlacz, K., & Ruiz-Agudo, E. (2012). The mechanism of thermal decomposition of dolomite: New insights from 2D-XRD and TEM analyses. *American Mineralogist*, *97*(1), 38-51.

Rohmer, J., Pluymakers, A., & Renard, F. (2016). Mechano-chemical interactions in sedimentary rocks in the context of CO2 storage: Weak acid, weak effects?. *Earth-Science Reviews*, *157*, 86-110.

Samuelson, J., & Spiers, C. J. (2012). Fault friction and slip stability not affected by CO2 storage: Evidence from short-term laboratory experiments on North Sea reservoir sandstones and caprocks. *International Journal of Greenhouse Gas Control*, *11*, S78-S90.

Shimamoto, T., and A. Tsutsumi (1994), A new rotary-shear high-speed frictional testing machine: its basic design and scope of research (in Japanese with English abstract), *J. Tectonic Res. Group of Japan*, *39*, 65-78.

Sigfusson, B., Gislason, S. R., Matter, J. M., Stute, M., Gunnlaugsson, E., Gunnarsson, I., ... & Wolff-Boenisch, D. (2015). Solving the carbon-dioxide buoyancy challenge: The design and field testing of a dissolved CO 2 injection system. *International Journal of Greenhouse Gas Control*, *37*, 213-219.

Spagnuolo E., Violay M., Nielsen S., Cornelio C., Di Toro G. Frictional instability under fluid stimulation: insights from load-controlled experiments on preexisting faults. *SEG, Lausanne. Switzerland, 25-28 September 2018*.

Terzaghi K (1925) Erdbaumechanik auf Bodenphysikalischer Grundlage. Franz Deuticke, Liepzig-Vienna

Tisato, N., Di Toro, G., De Rossi, N., Quaresimin, M., & Candela, T. (2012). Experimental investigation of flash weakening in limestone. *Journal of Structural Geology*, *38*, 183-199.

Violay, M., S. Nielsen, E. Spagnuolo, D. Cinti, G. Di Toro, and G. Di Stefano (2013), Pore fluid in experimental calcite-bearing faults: Abrupt weakening and geochemical signature of co-seismic processes, *Earth Planet Sc Lett*, *361*, 74-84, doi:10.1016/j.epsl.2012.11.021.

Violay, M., S. Nielsen, B. Gibert, E. Spagnuolo, A. Cavallo, P. Azais, S. Vinciguerra, and G. Di Toro (2014), Effect of water on the frictional behavior of cohesive rocks during earthquakes, *Geology*, *42*(1), 27-30, doi:10.1130/G34916.1.

Wang, X., Alvarado, V., Swoboda-Colberg, N., & Kaszuba, J. P. (2013). Reactivity of dolomite in water-saturated supercritical carbon dioxide: Significance for carbon capture and storage and for enhanced oil and gas recovery. *Energy conversion and management*, *65*, 564-573.

Waples, D. W., and J. S. Waples (2004), A review and evaluation of specific heat capacities of rocks, minerals, and subsurface fluids. Part 1: Minerals and nonporous rocks, *Natural resources research*, *13*(2), 97-122.

Wells, R. K., Xiong, W., Giammar, D., & Skemer, P. (2017). Dissolution and surface roughening of Columbia River flood basalt at geologic carbon sequestration conditions. *Chemical Geology*, *467*, 100-109

Wintsch, R. P., Christoffersen, R., & Kronenberg, A. K. (1995). Fluid-rock reaction weakening of fault zones. *Journal of Geophysical Research: Solid Earth*, *100*(B7), 13021-13032.

Zoback, M. D., & Gorelick, S. M. (2012). Earthquake triggering and large-scale geologic storage of carbon dioxide. *Proceedings of the National Academy of Sciences*, *109*(26), 10164-10168.

4. On the stability of sliding: hydromechanical responses of basalt rock-on-rock contacts to fluid pressure stimulations

Piercarlo Giacomel[1], Elena Spagnuolo[2], Stefano Aretusini[2], Chris W.A. Harbord[2,3], Marco M. Scuderi[1], Giulio Di Toro[1,4], and Cristiano Collettini[1,2]

[1]Dipartimento di Scienze della Terra, Sapienza Università di Roma, Rome, Italy

[2]Istituto Nazionale di Geofisica e Vulcanologia, Rome, Italy

[3]Now at Department of Earth Sciences, University College London, WC1E6BS, UK

[4]Dipartimento di Geoscienze, Università degli Studi di Padova, Padua, Italy

preliminary results

ABSTRACT

Diffusion of fluid pressure into pre-existing faults is one of the principal mechanisms for human-induced seismicity. This mechanism reduces the effective normal stress that clamps the fault in place promoting fault motion, yet it remains unclear the mode of fault slip upon reactivation and the conditions leading to dynamic frictional instabilities. Here we present laboratory tests on simulated basalt faults to investigate how the hydromechanical coupling affect the fault slip behavior and the dynamic weakening upon fluid pressure stimulations. We performed two types of experiments in a rotary-shear configuration on initially-bare, basalt surfaces:

(1) Constant displacement rate experiments at 10 μm/s to characterize the failure envelope of basalts bare rock surfaces;

(2) Unconventional creep experiments at constant shear stress on nearly critically stressed faults subjected to fluid pressurization, consisting in stepwise pressure increases of 0.2 MPa/300 s.

Creep experiments were run after a pre-shear stage of 4 mm and 50 mm of slip to test the effect of cumulated displacement on the hydromechanical properties and hence on fault frictional stability. To this end, the simulated faults were categorized according to their initial transmissivity and to net displacements before and after the tests. With the experimental simulation, we document that sheared basalts are frictionally strong, with the static friction coefficient within the range of Byerlee's rule for friction, i.e., $\mu \sim 0.66$. Before the onset of seismic slip, we recorded repeated slip pulses accompanied by shear compaction, and followed by fault deceleration and arrest. In the fault pre-sheared for 4 mm, the first slip episodes were characterized by slip rates of ~ 20 mm/s, whereas in the one pre-sheared for 50 mm, slip rates were one order of magnitude faster. Shear-enhanced compaction hindered the flow-through faults, facilitating the transition from drained to locally undrained hydrologic conditions, as testified by the development of fluid overpressure transients larger than the imposed fluid pressures. Fluid overpressure transients exacerbated the mechanical fault weakening effect induced by fluid pressure stimulations, which became more significant the lower the hydraulic transmissivity of the faults. Overall, our results show that compaction-induced weakening driven by fluid pressure stimulations can overcome the rate-strengthening behavior of bare surfaces on basalts, promoting seismic slip. Such feature would produce strong implications for the assessment and mitigation of seismic risk in geo-energy projects associated with in-situ wastewater injection into underground basaltic occurrences. To this purpose, further experimental investigation is strongly needed to support the present hypothesis.

4.1 INTRODUCTION

In the last few decades, the burning necessity of a global response to climate changes (*IPCC*, 2018) gave rise to a host of geoenergy applications alternative to conventional oil and gas extraction, such as geothermal energy and geological carbon sequestration (e.g., *Grigoli et al.*, 2017; *Vilarrasa et al.*, 2019). The synergic combination of such techniques potentially allows to produce geothermal energy at zero or even negative net carbon emissions, as proposed in the Hellisheidi geothermal power plant in Iceland (e.g., *Snæbjörnsdóttir et al.*, 2018; 2020 and references therein). In this context, industrial activities require both wastewater reinjection and pumping CO_2-rich water into nearby underground basaltic formations. One of the greatest concerns for the success of these geoenergy projects is managing the risk posed by fluid injection operations. In fact, starting from the seismic activity following deep wastewater disposal in the early 1950s until modern energy production (e.g., *Hubbert and Rubey*, 1959; *Horton et al.*, 2012; *Zoback and Gorelick*, 2012; *Langhenbruch and Zoback*, 2016), a growing number of unequivocal evidences attest that fluid injection into the Earth's brittle crust can nucleate seismic ruptures, with the seismicity rates being modulated by the fluid pressure buildups (*Zoback and Gorelick*, 2012). Many of these examples include also induced seismic events within continental interiors, far from plate boundaries in low deformation rates areas, such as the Canadian craton (*Atkinson et al.*, 2016) or the central United States regions, where moment magnitude larger than 5 earthquakes became ordinary and produced significant damage other than being felt by local communities (e.g., *Ellsworth*, 2013; *Keranen et al.*, 2013; *Rubistein et al.*, 2014). In such areas, fluid pressure increases can affect wide regions far from the injection site and persist even after injection shut-in (*Healy et al.*, 1968; *Ogwari et al.*, 2018). The recent dramatic experience in the enhanced geothermal system in Pohang (South Korea) further built up knowledge of induced-injection seismicity, proving that earthquake magnitudes are not necessarily bounded by injection volume but by the release of pre-existing tectonic stress (*Ellsworth et al.*, 2019; *Lee et al.*, 2019). Therefore, the injection activity may pose higher seismic risk than previously expected with an injected volume-based assessment protocol,

especially when shear stress is near the strength limit for (static) brittle failure (i.e., critically stressed: *Townend and Zoback*, 2000; *Walsh and Zoback*, 2016; *Ellsworth et al.*, 2019), whereby even small perturbations in pore fluid pressure may promote frictional instabilities and large earthquake ruptures (*Rothert and Shapiro*, 2007).

From a physical standpoint, in order to achieve a successful deployment of geoenergy sites, an important issue that needs to be addressed is how much fluid can be pumped without reaching mechanical failure, that is, the storage capacity of the reservoir. It is widely recognized that during fluid injection, fluid pressure diffusion plays an important role on the mechanical strength of faults affecting frictional failure. Notably, the degree of fluid pressure heterogeneities depends on the balance between injection rates and hydraulic properties (including permeability) along the fault (e.g., *Faulkner et al.*, 2018; *Passelègue et al.*, 2018). When the fluid pressure front equilibrates homogeneously within the fault, increase in fluid pressure causes a corresponding decrease in the effective normal stress that clamps the fault in place, according to the effective stress law (*Terzaghi*, 1925; *Hubbert and Rubey*, 1959; *Raleigh et al.*, 1976; *Sibson*, 1986; *Scholz*, 2019). Then, the effective stress law combined with the Mohr- Coulomb criterion predicts the stress condition for fault reactivation as:

Eq. (4.1) $$\tau_p \geq \tau = \mu\,\sigma_n' = \mu\,(\sigma_n - P_f)$$

where τ_p is the critical shear stress for fault reactivation, τ the fault shear strength, σ_n' the effective normal stress acting on the fault, μ the sliding friction coefficient, and P_f the fluid pressure. According to Eq. (4.1), an increase in Pf, reduces the shear stress acting on the fault, until reaching a static critical value τ_p equal to the shear strength required for promoting fault slip (e.g., *Jaeger and Cook*, 1979). When fault reactivates, under some circumstances, asperity collapse and fluid flow-restricting frictional wear debris can develop during shearing (e.g., *Faoro et al.*, 2009; *Tanikawa et al.*, 2010; *Rutter and Mecklenburgh*, 2018), in a process called shear-enhanced fault compaction. Following this process, the fault can transition from drained to locally undrained conditions because of the consequent decrease in fault transmissivity even when the hydrological boundaries are drained (e.g., *Passelègue et al.*, 2018; *Proctor et al.*, 2020). Contrarily to the drained scenario, locally undrained conditions

are generally characterized by the presence of a fluid pressure gradient, that is, a heterogeneous fluid pressure distribution along the fault and are particularly interesting for their unpredictable effects on fault activation. Indeed, under undrained or locally undrained conditions, shear-enhanced fault compaction causes pore volume and/or pore temperature changes yielding to fluid pressure transients larger than the imposed fluid pressure (=fluid overpressure), promoting the weakening of the faults (e.g., *Morrow and Byerlee*, 1989; *Segall and Rice*, 1995; *Samuelson et al.*, 2009; *Segall et al.*, 2010; *Ferri et al.*, 2010; *Scuderi et al.*, 2015; *Violay et al.*, 2015; *Faulkner et al.*, 2018 among many others). In fact, significant compaction-induced fluid overpressure may potentially overcome or exacerbate the frictional properties changes predicted by empirical rate-and-state friction laws (*Dieterich*, 1979; *Ruina*, 1983; *Marone*, 1998), and determine the initiation of earthquake runaway ruptures even in velocity strengthening materials, as theorized by numerical models (e.g., *Cappa and Rutqvist*, 2011), field-scale (e.g., *Guglielmi et al.*, 2015 and *Cappa et al.*, 2019), and laboratory findings (e.g., *Scuderi et al.*, 2017; *Scuderi and Collettini*, 2018; *Proctor et al.*, 2020). Moreover, coupled hydromechanical changes are also influenced by the fault structure evolving during shearing (*Scuderi and Collettini*, 2018), which may additionally affect the friction velocity dependence (e.g., *Mair and Marone*, 1999; *Ikari et al.*, 2011). Summarizing, both structural and hydraulic properties of fault materials exert first-order control on the stability of sliding but the evolution of such properties during the slow to high velocity deformation of a fault subjected to gradual changes in the stress field is still largely unknown.

Here we aimed to shed light on the fluid pressure controls on the onset of fault reactivation and the fault slip characteristics of experimental basalt fault interfaces nearly critically pre-loaded. The present study allowed to simulate the resolved stress conditions typical of faults/fractures in a tectonically active area such as the Icelandic geothermal site (e.g., *Snæbjörnsdóttir et al.*, 2018). In particular, we captured the coupled hydromechanical responses during fluid pressurization of faults exhibiting different starting hydraulic properties (= fault transmissivity) and accumulated shear displacements (=fault structure) and compared the fault slip behavior with the rate-and-state frictional properties of selected basalts at water-saturated conditions.

4.2 MATERIALS AND METHODS

To get insights on the slip behavior of basalt-bearing faults upon fluid pressure stimulations, we performed laboratory friction experiments using the rotary-shear apparatus SHIVA, hosted at the Istituto Nazionale di Geofisica e Vulcanologia (INGV, Rome- Italy) (*Di Toro et al.*, 2010; *Niemeijer et al.*, 2011). We simulated faults characterized by rough rock-on-rock contacts by juxtaposing basalt hollow cylinders 50/30 mm external/internal diameter, prepared through the procedure described in *Nielsen et al.* (2012). Bare surfaces were ground flat and parallel using a precision lathe, which ensures in most cases sample misalignment smaller than 100 μm. Subsequently, to impose on the rock assemblages a reproducible starting roughness, each sample was hand-lapped on a glass plate with water and #80 grit SiC powder before being mounted on SHIVA apparatus. Initial surface roughness differences among the samples may be attributed to a variable proportion phenocrystal/ groundmass (Figure S4.1). Selected basalts are low porosity (≤ 6% connected porosity) alkali lava floods from Mount Etna (Italy), pertaining to the same batch employed in Chapter 2 of this thesis. We therefore refer to Chapter 2 for the full chemical, mineralogical, and optical characterization of the starting material.

We performed two types of friction experiments:

1- Constant displacement rate experiments to investigate the basalt frictional strength in the presence of pressurized fluids;
2- Unconventional creep experiments at constant shear stress, to investigate the fault slip behavior and dynamic weakening of critically stressed faults upon fluid injection.

All the tests were performed at room temperature and the cylinder pairs were inserted in a vessel allowing fluid pressure confinement (e.g., *Violay et al.*, 2013, 2014; *Giacomel et al.*, 2018). Fluid pressure was controlled either by connecting two fast-acting servo-controlled intensifiers belonging to the biaxial deformation machine BRAVA (*Collettini et al.*, 2014) (constant displacement rate experiments) or two syringe Teledyne ISCO pumps (creep tests)

(Figure 4.1). Volume changes were monitored via the LVDT coupled to the pumps and the fluid pressure monitored through pressure transducers accurate to 7 kPa for the fluid pressure intensifiers and 70 kPa for the syringe pumps. Both experiment types were preceded by a common loading and pressurizing protocol. Fluids, consisting in distilled water, were injected radially (upstream beam) and collected via the inner hole of the stationary hollow cylinder (downstream). Both the upstream and the downstream were controlled in volume, flow, and pressure. First, we removed the air from the upstream and downstream pumps with the reservoirs closed to the atmosphere. Subsequently, we started with the fluid pressure vessel saturation by injecting distilled water (valves A, C open, and valve B closed; Figure 4.1), until water flowed through valve C, positioned on purpose, on the upper part of the vessel. Once we ensured the complete saturation of the pressurizing circuit and the lack of any residual air in the system, valve C was closed and we applied the normal load by applying a loading ramp until the achievement of the normal load target of ~ 15 kN in experiment s1825, that was reduced to ~ 14.3 kN in experiment s1827 due to technical issues.

Next, we pressurized the injected distilled water under nominally drained and initially sub-hydrostatic boundary conditions (valve A open and valve B, C closed), at a starting pore fluid factor $\lambda = Pf/\sigma_n = 0.23$. We waited for the complete downstream fluid pressure equilibration to the upstream fluid pressure before proceeding with the specific test type. Due to our sample geometry and size, the fluid pressure contributes to the total normal stress, resulting in the corrected normal stress, $\sigma_n = N/A_R - \xi \cdot Pf$, where N is the applied normal load, A_R the basalt area of the hollow cylinders, and ξ a geometrical corrective factor we theorized from the observations and calculated equal to 0.5625 (we refer to Appendix 1 for further details). Normal stress σ_n, fluid pressure Pf, axial shortening, equivalent slip δ, equivalent slip velocity V, and the shear stress τ (evaluated on the annulus radii and the applied torque: *Shimamoto and Tsutsumi*, 1994) were sampled at acquisition rate of up to 125 Hz. The axial shortening was acquired continuously during the tests via a linear variable displacement transformer (LVDT), referenced at the loading frame in the sample chamber close to the pressure vessel, with an accuracy of ± 30 nm.
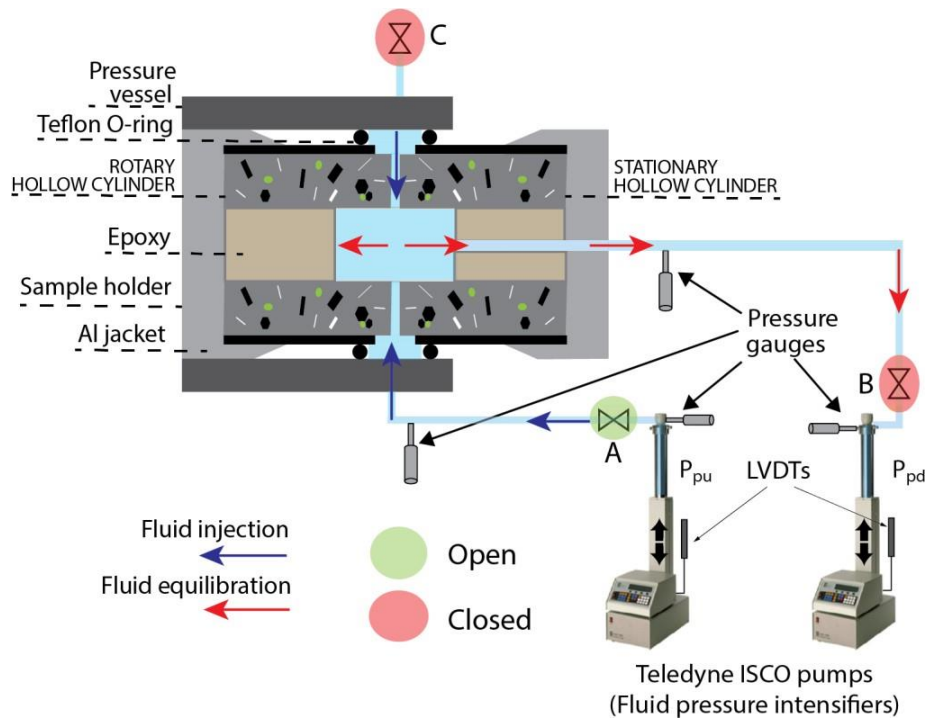
Figure 4.1: Schematic diagram (not to scale) of the flow system through the experimental basalt fault, here shown in longitudinal section, during fluid pressurization via the Teledyne ISCO syringe pumps. For the tests involving the BRAVA's fluid pressure intensifiers, the hydraulic circuit remains unchanged.

Additionally, to study the fluid transport capacity changes of the basalt slipping zone at different effective normal stresses and cumulated displacements, we measured the hydraulic transmissivity of the experimental faults installed in SHIVA (e.g., *Witherspoon*, 1980; *Zimmerman and Bodvarssonn*, 1996). Transmissivity has dimensions of cubic millimeters and it is given by the product of the intrinsic permeability of the rock macrofracture (m^2) with its hydraulic aperture b_h (m) (e.g., *Rutter and Mecklenburgh*, 2018), here represented by the mean height of the contact asperities. Therefore, with respect to the intrinsic permeability, quantifying the transmissivity allows to unravel the transport properties of basalt faults independently of the hydraulic aperture. Benchmarks on fracture transmissivity were provided by calculating the transmissivity of a) saw-cut basalt full cylinders, cut parallel to the basalt cylinder axis and b) intact cores using the permeameter installed at INGV Rome (Italy) (Figure 4.2). Because the intact core permeability is numerically equal to the transmissivity of a meter-thick layer of matrix material, it can be directly compared to crack transmissivity. In all the tests the hydraulic properties of rocks were determined using distilled H_2O as the permeating fluid.
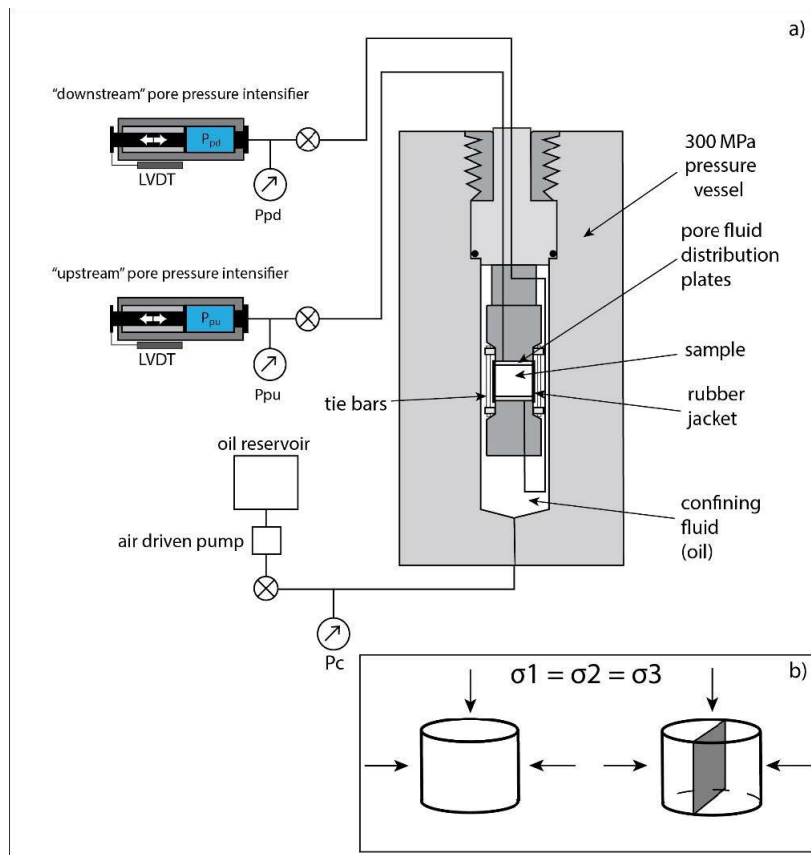
Figure 4.2: **(a)** Schematic diagram illustrating the permeameter used in our tests (after *Heap et al.*, 2014). **(b)** Intact core and saw-cut samples mounted on the pressure vessel under isotropic stress conditions.

4.2.1 Constant displacement rate experiments

We carried out experiments at nominally constant Terzaghi effective normal stress σ'_n = 4 − 8 − 12 − 16 MPa, which corresponds to $\sigma_n' = 3.4 − 6.9 − 10.3 − 13.8$ MPa when the geometrical corrective factor ξ (Appendix 1) is applied, under subhydrostatic conditions (i.e, $\lambda = 0.23$) (Table 4.1a). Simulated faults were slid at a constant displacement rate of V = 10 µm/s until shear steady-state conditions were established.

4.2.2 Unconventional creep experiments

Creep tests were performed at effective normal stresses of ~ 8 MPa. For a more accurate control of the normal stress acting on the simulated fault, normal load was applied using an electromechanical piston Rexroth IndraDrive. Unfortunately, it should be emphasized that the shear stress data are affected by spurious vibrations of the

electromechanical piston used to supply the axial load (Figure 4.3). This technical issue is a consequence of a recent update of the machine. Despite the large oscillations it was possible to retrieve and simplify the main characteristic of the two experiments proposed. The test will be reproduced in view of a paper submission.
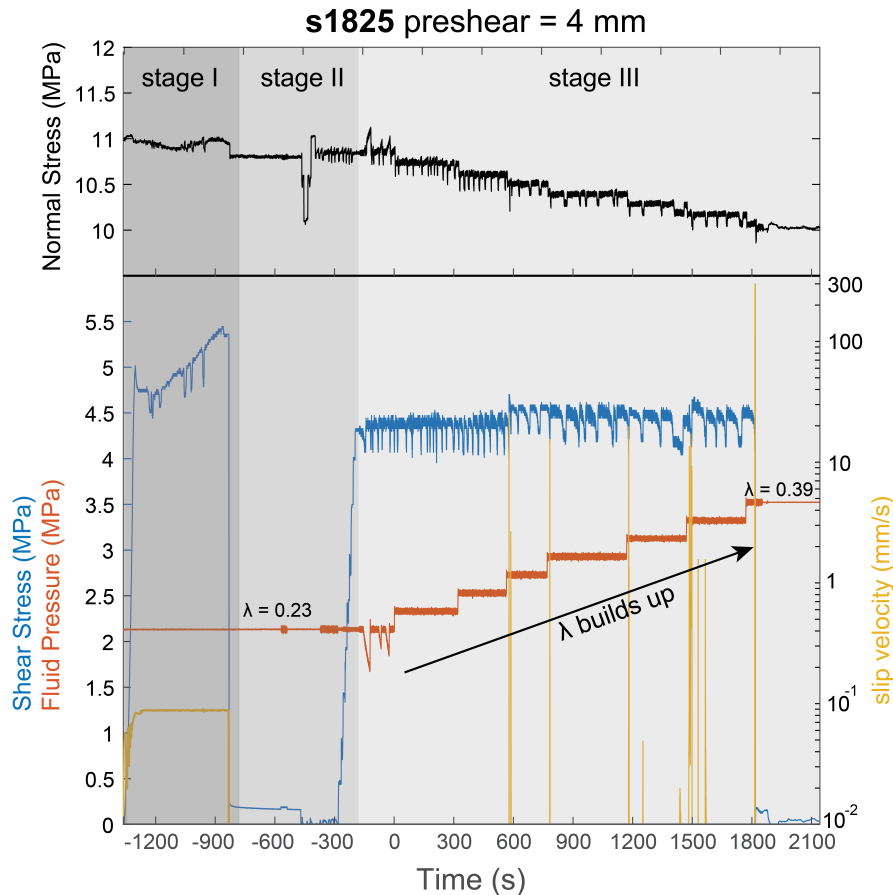
Figure 4.3: Typical creep experiment with the fault subjected to pre-shear of 4 mm (test s1825). The three stages of a typical tests described in section 4.2.2 are depicted in grey shades.

Creep tests can be divided into three sequential stages (Figure 4.3): (1) a pre-sheared stage, where samples were slid at V = 10 µm/s and λ = 0.23 to provide reproducible contact surfaces at two different initial conditions of 4 mm (exp s1825) and 50 mm (exp s1827). During this stage, the peak shear stress τ_p was measured as a reference value for step 2 (Table 1b). (2) pre-loading stage, where the sprag clutch of the low velocity gear was disconnected, the system was switched from a velocity to torque control mode and the shear stress was set to nominal 85% of τ_p. (3) stepwise pressure increase at constant pressure rates of 0.2 MPa/300 s operated manually, where distilled water was injected radially through the

slipping zone from the upstream syringe pump whereas the downstream reservoir pump was closed to the atmosphere (valve A open and valve B closed). It should be noted that, owing to the geometrical correction, fluid pressure step increases imply a consequent decrease in the applied normal stress, other than a decrease in the effective normal stress (Eqs. S1.4 and S1.5, Appendix 1). During each step, we checked the upstream – downstream equilibration times, which can be regarded as a proxy for the permeability evolution with time and provide insights on the pathways of fluid circulation. In fact, taking as a reference the benchmark of the permeability measurements performed with the permeameter (see 4.2.3 for details), ~ 20 seconds is the average time required to equilibrate the downstream and upstream pressures in a lab-fault of 10 mm length. Any time smaller than one order of magnitude in seconds would suggest that the fluid was circulating across preferential pathways (e.g. through apertures due to micrometric misalignments) rather than across the entire slipping zone. After stage 3, the tests ended with the occurrence of the main instability event (MI). The latter is an unstable slip event that achieved a significant stress drop with slip (i.e, > 1 MPa, Figure 4.3), leading to a runaway rupture that was automatically limited to a target slip rate of 300 mm/s and was manually stopped after 5 s (e.g., *Giacomel et al.*, 2018; *Spagnuolo et al.*, 2018). In our tests, MI are generally preceded by short-living slip events, i.e., fault reactivations characterized by fast slip acceleration reaching slip rates lower than 300 mm/s, followed by spontaneous deceleration and arrest (Figure 4.3).

4.2.3 Transmissivity measurements

The permeameter used to measure the hydraulic properties of basalts is equipped with three hydraulic servo-controlled pressure intensifiers to apply confining pressure Pc up to 300 MPa, and upstream and downstream pore fluid pressure up to 70 MPa (e.g., *Trippetta et al.*, 2017). The confining pressure was applied hydrostatically to the sample via a hydrogenated paraffinic oil, such that the effective pressure results from Pe = Pc – α Pf , assuming the poroelastic constant α = 1 (e.g. *Paterson and Wong*, 2005).

All measurements were made by providing a fluid pressure gradient to each end of the rubber jacketed intact/saw-cut cylinders 38 mm diameter by ~ 29 mm length, through the

upstream and downstream intensifiers fitted with LVDTs which monitor the position of the pistons and enable them to act as volumometers. Given the anticipated high permeability of the saw-cut, pore fluid distribution plates were removed during tests in order to avoid biased measurements reflecting the permeability of the porous plates rather than the saw-cut permeability. In this study, we set a pore fluid pressure gradient ∇P = 0.5 and 0.2 MPa to mimic the experimental conditions in SHIVA for both intact and saw cut specimens, for a constant mean fluid pressure of 4 MPa, resulting in Pe ranging from 4 to 12 MPa. After the attainment of a steady-state flow rate, the permeability of the intact core k_{core} was determined via application of the Darcy's law:

Eq. (4.2)
$$k_{core} = \frac{Q \cdot \eta \cdot L}{\nabla P \, A}$$

where, Q the mean steady-state flow rates (m^3/s) measured at the upstream (P_{pu}) and downstream (P_{pd}) intensifiers (Figure 4.2), η the dynamic viscosity set to 8.9·10^{-4} Pa·s at 298 K, L the sample length (m) and A the cross sectional area (m^2).

Analogously, following *Rutter and Mecklenburgh* (2018), macrofracture transmissivity can be viewed as the product k_{frac} b_h, with k_{frac} indicating the fracture permeability, b_h the hydraulic aperture:

Eq. (4.3)
$$T_{perm,ssf} = k_{frac} \, b_h = \frac{Q \cdot \eta \cdot L}{\nabla P \, 2r}$$

where *r* is the sample radius (m).

Transmissivity was measured on SHIVA during unconventional creep tests before the pre-shear phase for reproducibility purposes and after the main instability (MI) event to illuminate possible changes in transport properties during the tests. In both cases these measurements were made at null shear stress and target effective normal stress ranging from 6 to 11 MPa.

Pre-experimental transmissivity was calculated using the steady-state flow method, which consists in applying a constant fluid pressure gradient between the upstream and

downstream syringe pumps, following Darcy's law:

Eq. (4.4)
$$T_{shiva,ssf} = k_{cyl,ssf} \, b_h = \frac{Q \cdot \eta \cdot L}{\nabla P \, 2\pi r_{avg}}$$

Eq (4.3) and Eq. (4.4) only differ in the sample geometry and notably in the fracture width, where in the saw-cut full cylinder it is represented by the core radius, while in the hollow cylinder pair by the radius r_{avg}, averaged between the inner and external radius of the hollow cylinder. In these tests, we imposed ∇P = 0.2 MPa across the slipping zone, for a mean Pf = 0.5 and 2.3 MPa, implying σ_n' ~ 8 to 11 MPa. Following the cubic relation between fluid flow along a microfracture and the hydraulic aperture, Eq. (4.4) is equivalent to:

Eq. (4.5)
$$T_{shiva} = \frac{b_h^3 \cdot \rho g}{12 \, \eta}$$

During the tests, changes in hydraulic aperture caused by mechanical responses modify the fault hydraulic transmissivity of an amount Δb_h. To a first approximation, changes in hydraulic aperture are equal to changes in fault normal displacement, Δb_n, which can be tracked by the LVDT, so that the transmissivity becomes:

Eq. (4.6)
$$T_{shiva} \cong \frac{(b_h + \Delta b_n)^3 \cdot \rho g}{12 \, \eta}$$

At the end of the tests following the MI, we measured the permeability of the sliding surface with the oscillating method pore pressure (*Bernabé et al.*, 2006; *Faulkner and Rutter*, 2000; *Fischer*, 1992 among the others). The application of fluid pressure oscillations was done using DIsco 1.16, a control interface developed for LabVIEW by Luke P. Frash (Los Alamos National Laboratory) which enables serial communication for remotely controlling and monitoring the ISCO pumps. The use of this method became necessary to quantify the fault transmissivity at the end of the tests because of the formation of shear debris during the MI that markedly hindered the fluid flow through pair samples, thereby rendering the steady-state flow method ineffective.

The slipping zone hydraulic transmissivity is given by (*Bernabé et al.*, 2006):

Eq. (4.7)
$$T_{shiva,osc} = k_{cyl,osc}\, b_h = \frac{2A}{\sqrt{1-A^2}} \cdot \frac{\eta\, \text{\ss}_D}{\Delta t} \cdot \frac{r_{ext} - r_{int}}{r_{ext} + r_{int}}$$

where A is the pressure gain, i.e. the ratio between the peak-trough amplitude of the downstream reservoir and the upstream reservoir; Δt is oscillation period set to 60 s, and r_{ext} and r_{int} are the external and internal radius of the annulus. $\text{\ss}_D$ is the downstream storage capacity (m^3/Pa) (*Fischer*, 1987), which can be worked out as the product of the fluid compressibility (=1 in the case of water) at a given temperature and pressure, with the total downstream volume before the fluid pressure oscillations (e.g., *Faulkner*, 1997), including the volume of water stored in SHIVA's pressure vessel as well as the volume of the pipes connecting the downstream ISCO pump with the inner hole of the stationary sample (Figure 4.1). All the transmissivity measurements are reported in Table 4.1c.

(a)   Mechanical data: constant displacement rate experiments

Exp. name	σ_n' (MPa)	τ_{ss} (MPa)	$\lambda = Pf/\sigma_n$	slip (mm)
s1536	3.1	2.2	0.24	1
	6.6	4.8	0.23	3.5
	10.5	7.6	0.22	5.6
	14.3	10.5	0.22	9.2
s1540	3.2	1.5	0.23	1
	6.5	3.7	0.23	3.4
	10.5	6.3	0.22	6
	14.2	8.8	0.22	9.1
s1593	14.5	9.1	0.22	4

(b)   Mechanical data: creep   experiments

Exp. name	σ_n' (MPa)	τ_p (MPa)	$\%\tau_p$ (MPa)	λ,i	Pre-shear (mm)
s1825	8.5	5.4	81	0.22	4
s1827	7.7	5.3	87	0.23	50

(c)   Transport properties: transmissivity measurements

Apparatus	Exp. name	method	Pe (MPa)	Transmissivity (m^3)	slip (mm)
permeameter	Core1	Ssf	3.8	5.66E-19	0
	Core1	Ssf	3.8	5.39E-19	0
	Core1	Ssf	3.8	2.35E-19	0
	Core1	Ssf	8.1	3.84E-19	0
	Core1	Ssf	8.1	2.95E-19	0
	Frac1	Ssf	3.7	8.14E-16	0
	Frac1	Ssf	3.8	8.31E-16	0
	Frac1	Ssf	8.1	3.05E-16	0
	Frac1	Ssf	8.1	7.54E-16	0
	Frac1	Ssf	8	8.14E-16	0

Frac1	Ssf	8.1	7.08E-16	0
Frac1	ssf	11.8	8.15E-16	0
Frac1	Ssf	11.7	7.65E-16	0
Frac1	Ssf	11.8	7.14E-16	0
SHIVA	s1825	Ssf	11.2	6.71E-17	0
	s1825	Ssf	8.4	5.68E-17	0
	s1825	Osc	6.1	6.83E-19	868.8
	s1827	Ssf	10.7	4.97E-16	0
	s1827	Ssf	7.8	4.93E-16	0
	s1827	Osc	6.2	2.61E-19	817.5

(d)	Transport properties: equilibration time measurements (SHIVA)					
Exp. name	τ (MPa)	$\sigma_n{'}$ (MPa)	P_{fu} (MPa)	∇P (kPa)	t_e (s)	slip (mm)
s1825	4.4 ± 0.1	7.9	2.6	200	31	4.2
	4.4 ± 0.1	7.6	2.8	200	35	4.2
	4.4 ± 0.1	7.3	3	200	44	4.2
	4.4 ± 0.1	7.0	3.2	200	117	14.7
	4.4 ± 0.1	6.7	3.4	200	52	20.3
	4.4 ± 0.1	6.4	3.6	200	102	30.1
s1827	4.4 ± 0.2	7.5	2.5	200	19	49.7
	4.4 ± 0.2	7.2	2.7	200	18	49.7
	4.4 ± 0.2	6.9	2.9	200	12	49.7
	4.4 ± 0.2	6.6	3.1	200	22	49.7

Table 4.1: Summary of the experiments and boundary conditions. **(a)** Constant displacement rate tests to assess the frictional strength of basalt faults. We denote the following acronyms: ($\sigma_n{'}$) effective normal stress corrected for the geometrical model; (τ_{ss}) stable sliding shear stress, at steady-state; (λ) fluid factor; (slip) accumulated shear displacement. **(b)** Data from unconventional creep tests. (τ_p) shear stress recorded at the end of the pre-shear phase; (λ,i) pore fluid factor at the beginning of the tests; (%τ_p) percentage of shear stress reached at the end of the pre-shear, applied at the onset of fluid pressure steps; (pre-shear [mm]): cumulated slip at the end of the pre-shearing phase. **(c)** Experiments aimed to get the transport properties of basalt cores and simulated faults: (ssf) steady state flow; (osc) oscillating pore fluid pressure technique; (Pe) Terzaghi's effective pressure; (Transmissivity) hydraulic transmissivity; (slip) displacement cumulated prior to the measurements. **(d)** Data showing the equilibrium times (t_e) measured prior the onset of the main instability. (∇P) is the fluid pressure gradient between the upstream and downstream pump.

4.3 RESULTS

4.3.1 Constant displacement rate tests: short term frictional strength

We measured the shear strength for steady-state frictional sliding τ_{ss} of basalt bare surfaces at σ_n' from ~ 3 to 14 MPa, under sub-hydrostatic conditions ($\lambda = 0.23$) (Table 4.1a). The values of steady-state frictional strength scale linearly with the effective normal stress and satisfy the Mohr-Coulomb frictional sliding criterion for fault reactivation (Eq. (4.1)), yielding $\mu_{ss} = 0.66$ (Figure 4.4). These data fit the Byerlee's friction of strong fault rocks such as basalts (*Byerlee*, 1978), within the scatter generally observed in friction experiments at low normal stresses, which in our tests can be reasonably attributed to specimen heterogeneities (i.e., phenocrystals/groundmass ratio) or pair sample misalignments.
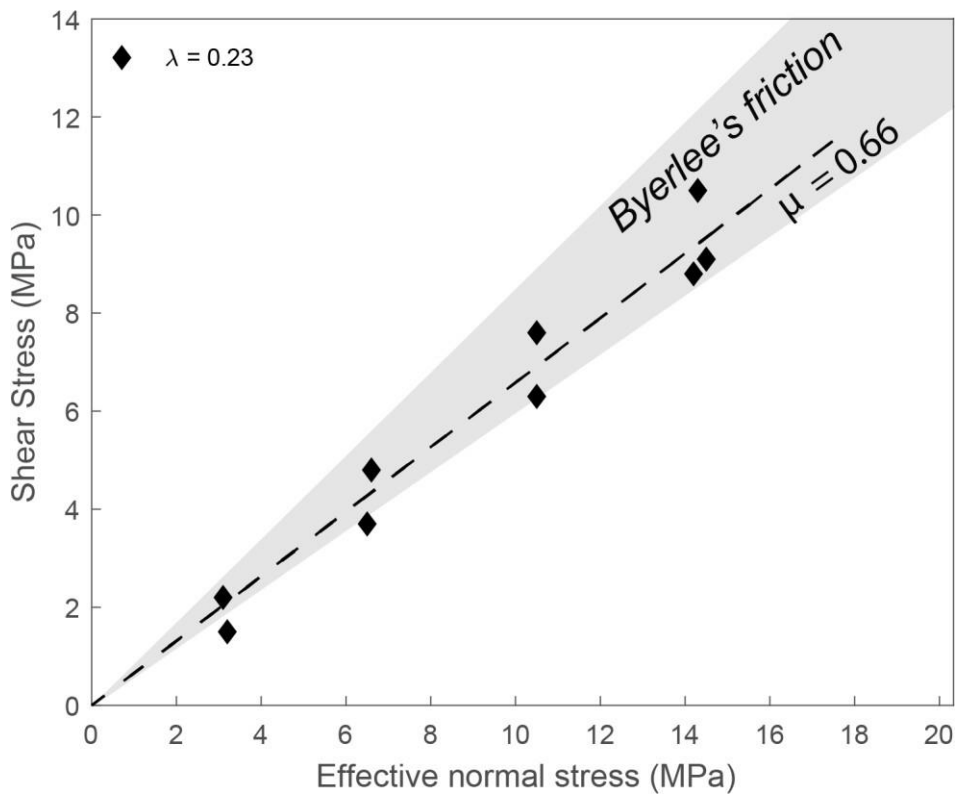
Figure 4.4: Mohr-Coulomb frictional sliding criterion, reporting the value of steady-state shear strength collected at different effective normal stresses at the pore fluid factor $\lambda = 0.23$, during the constant displacement rate tests at V = 10 μm/s. The steady-state friction coefficient fits the Byerlee's friction here represented by the shaded area.

4.3.2 Unconventional creep tests: fault slip behavior and frictional instabilities

To get insights on the slip behavior of basalt-bearing faults upon fluid pressure stimulations, we tracked changes in fault displacement under constant shear stress conditions, where the applied shear stress was kept close to the critical condition and the fluid pressure was increased stepwise. Specifically, the shear stress was kept constant at nominally 85% of the peak in shear strength recorded at 4 and 50 mm net slip, respectively (Table 4.1b; Figure 4.3). Our data show that the onset of fault reactivation is modulated by fluid pressurization before the main instability, MI, resulting in a variety of fault slip behaviors. Notably, the fault slip behavior is affected by the amount of pre-shear prior the onset of fluid pressure steps. Figure 4.5 shows the evolution of slip and slip velocity for the tests conducted under the two different initial conditions, where t0 is the time at the beginning of the stepwise pressure increase. Figure 4.6 reports the corresponding stress path represented in the Mohr-Coulomb space, indicating the evolution of the resolved stress state during the tests. In both cases fault reactivation occurs at an effective normal stress compatible with the sliding friction coefficient obtained from the constant displacement rate tests (i.e., $\mu \sim 0.66$, Figure 4.6), and is preceded by accelerating tertiary creep that evolves into a slip event at coseismic slip rates (Figure 4.5a, insets ii,II).

For the 4 mm test, at the initiation of the fluid pressure increase, the stress state of the fault is far from the fault reactivation criterion in the Mohr-Coulomb diagram, and fault slips by aseismic creep in response to pressure steps (Figures 4.5a, inset i). Once the fault approaches the stress state required for fault reactivation (Figure 4.4), increasing fluid pressure triggers fault acceleration with a peak velocity of $\sim$ 25 mm/s immediately followed by a spontaneous slip deceleration, during which the fault accumulated $\sim$ 13 mm slip (purple peak in Figure 4.5b). The onset of frictional failure was achieved at Pf = 3.0 MPa and a corresponding $\lambda \sim 0.29$. Subsequent stepwise pressure increase at 0.2 MPa/300s was accompanied by slip episodes similar in duration, accumulated slip and slip velocity as the first reactivation episode, until the achievement of Pf = 3.8 MPa and $\lambda \sim 0.39$ where we document the onset of the MI.

For the 50 mm test, far from the reactivation envelope, aseismic slip accompanies the stepwise increase in fluid pressure analogously to the 4 mm case (Figure 4.5a, inset I). However, as we approach the resolved stress state for frictional failure, fluid pressurization causes slip acceleration and subsequent deceleration with the slip velocity increasing up to 230 mm/s, i.e. one order of magnitude higher compared to the 4 mm tests, with an accumulated slip of ~ 230 mm (Figure 4.5c, right panel). The critical stress for fault reactivation was reached at Pf = 3.1 MPa at hydrostatic conditions (i.e., λ = 0.33). A further fluid pressure step was sufficient to trigger the MI. The slip curve and shear stress drop characterizing dynamic failure was similar compared to the one observed for the 4 mm case (Figure 4.6).
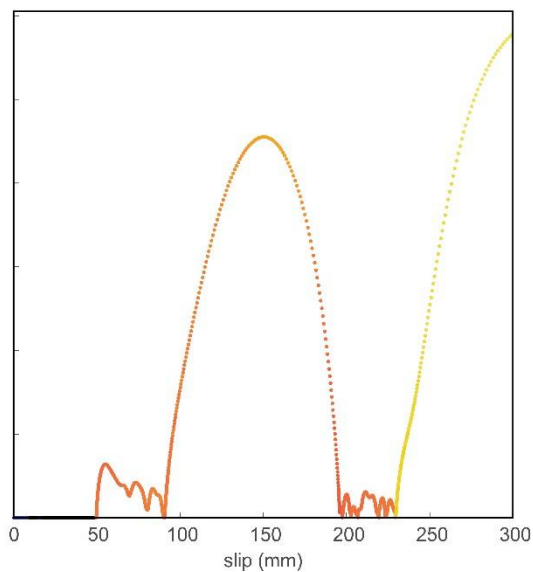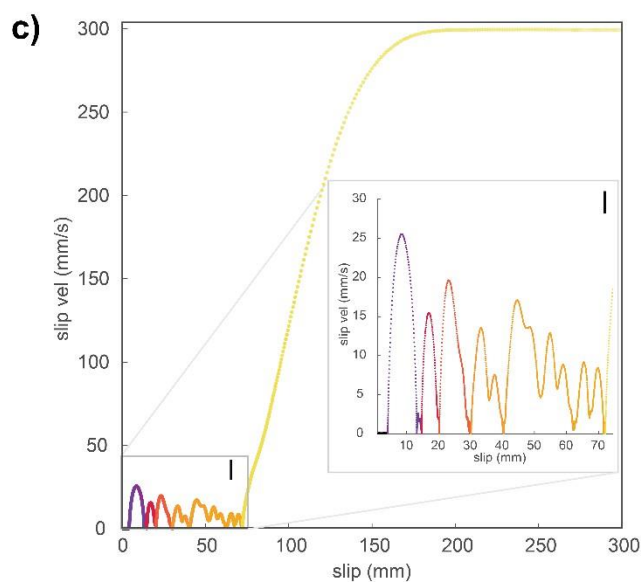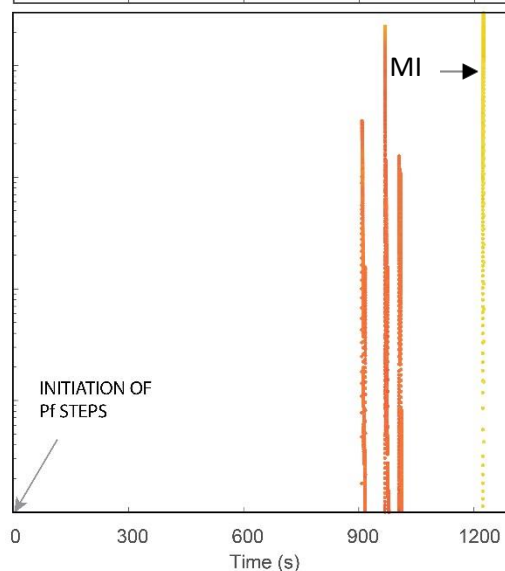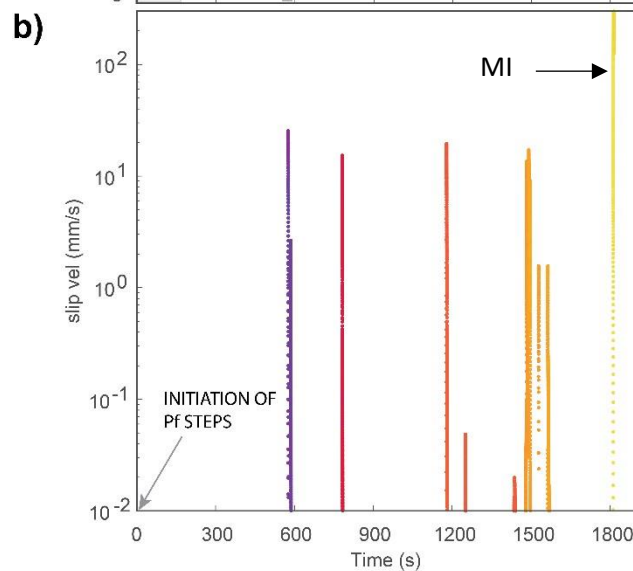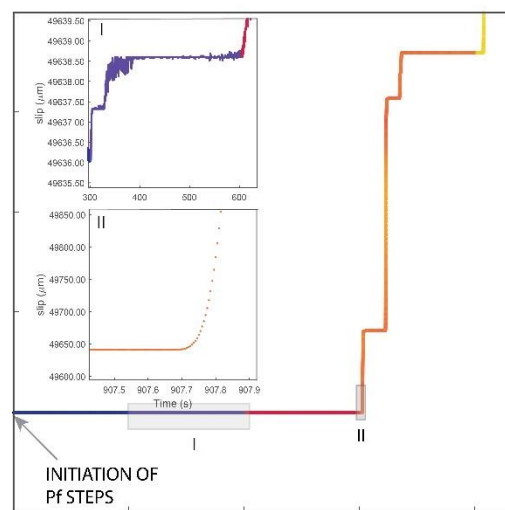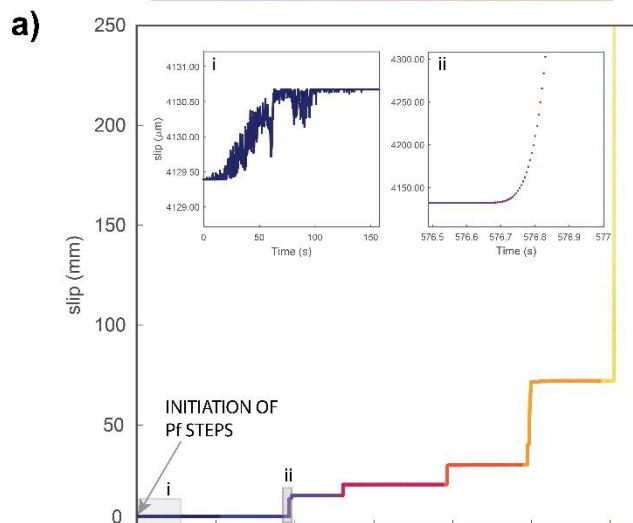
Figure 4.5: Raw data indicating the evolution of fault slip (**a**) and slip velocity (**b,c**) throughout the creep tests pre-sheared for 4 mm (left panels) and 50 mm (right panels) (exp. number s1825 and s1827, respectively), against time (**a,b**) and slip (**c**). The points are color coded by the pore fluid factor, $\lambda = Pf/\sigma_n$ with Pf representing the applied fluid pressure at the upstream syringe pump. The insets in panels (**a**), show a detail of the aseismic creep following the first stages of fluid injection (i,I) and accelerating slip preceding frictional failure (ii,II).(**c**) slip velocity as a function of slip for both the test types, in which the panel shows a detail of fault reactivation events before the main instability that ends the tests.
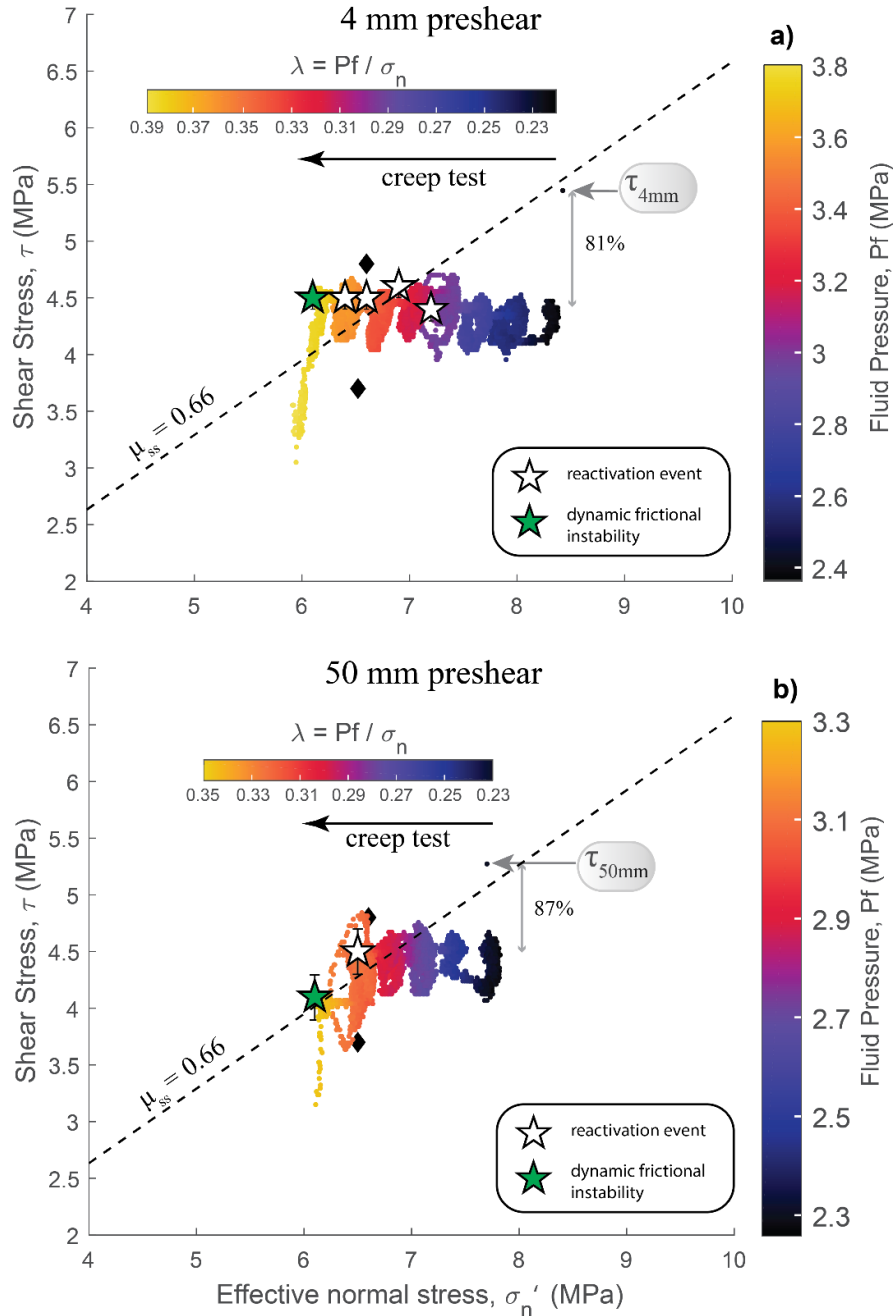

Figure 4.6: Mohr-Coulomb reactivation diagram showing the corresponding stress path evolution for the curves shown in Figure 4.5, with respect to the reactivation criterion established by constant rate experiments (black dashed line, retrieved in Figure 4.4). The pressurization stage of 0.2 MPa/300s follows the pre-shear at constant displacement rate at $V= 10$ μm/s for 4 mm (**a**) and 50 mm (**b**). The symbols are color coded for the applied fluid pressure at the injection side (upstream syringe pump) and the related pore fluid factor λ. Fault slip episodes with $15<V\leq 230$ mm/s (white stars) and the main frictional instability ($V = 300$ mm/s) that ends the tests (green stars), are reported.

4.3.3 Axial displacement evolution

Monitoring the spontaneous evolution of the axial displacement upon fluid injection at constant shear stress (creep tests) provides insights on the micromechanical behavior of bare rock surfaces in connection with the evolving hydraulic properties. The hydraulic aperture, here connected to the mean asperities height, can be indirectly measured from the axial shortening (Figure 4.7) against time and slip, where the time corresponding to the onset of fluid pressure increase was set to 0. We indicate with h0 the axial shortening at the onset of the fluid pressure steps; thus h-h0 points out the axial shortening changes with respect to h0 (= relative normal displacement, Δb_n): positive h-h0 mark shear compaction, whereas negative values define fault dilation, causing a corresponding decrease or increase in fault transmissivity (Eq. (4.6)) .

The visible oscillation in the axial shortening is due to the sample rotation in the presence of ~ 100 μm pre-existing sample misalignments or contact irregularities due to wearing. The period of the oscillation is one rotation (~ 126 mm, blue in color dashed line for reference in Figure 4.7e,f) whereas the amplitude of the oscillations is damped down by progressive wearing during frictional sliding. Therefore, it should be stressed that the recorded dilation accompanying fault acceleration during the first sliding episode in the 50 mm pre-shear sample (red arrows, Figure 4.7b,d) is likely an artifact due to sample rotation that masks the actual compaction observed at the beginning of this fault slip (upward arrow, Figure 4.7f, inset). Analogue conclusions can be drawn for the initial apparent dilation at the onset of the MI in the 4 mm sample (Figure 4.7e, inset). As expected, the amount of shortening is slip- dependent: the axial shortening characterizing sample after 4 mm pre-shear amounts to ~ 310 μm, while the shortening value recorded after 50 mm of slip is ~ 660 μm (Figure 4.7 a to d). In both experimental protocols, we document dilation at the early stages of fluid pressurization. As we approach the critical stress state for fault reactivation, h-h0 transitions abruptly from dilation to compaction associated to fault slip (Figure 4.7a to d). In common for both cases, following the first (short-living) slip event, fault experiences overall compaction as fluid pressurization proceeds.
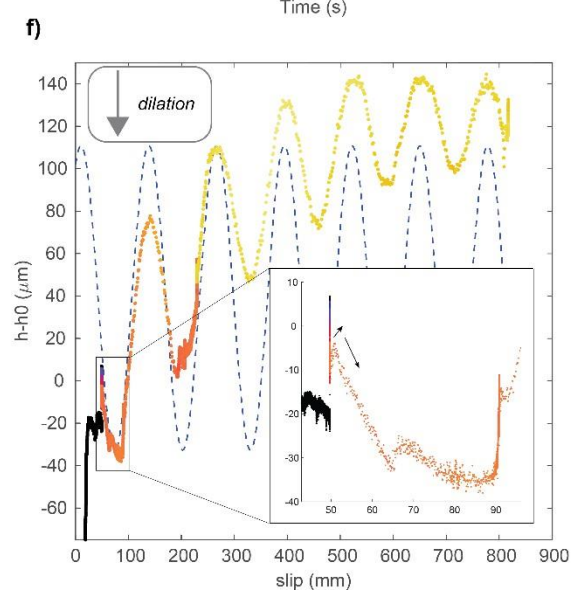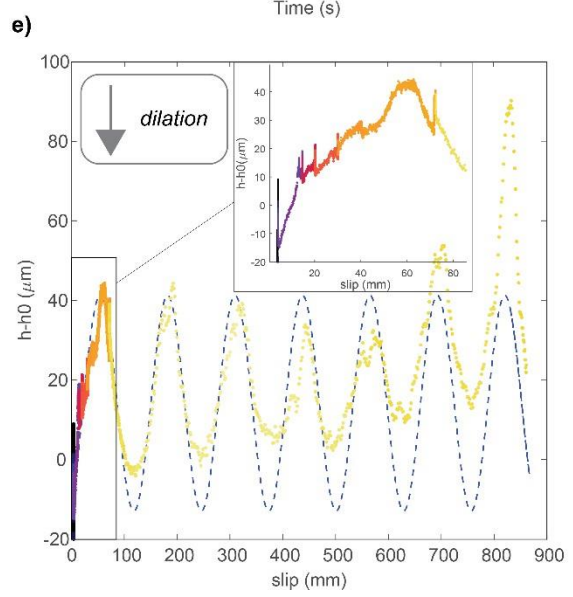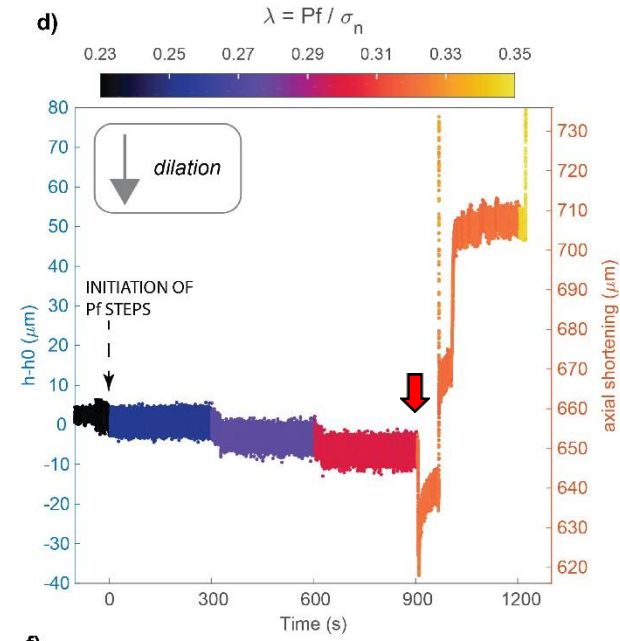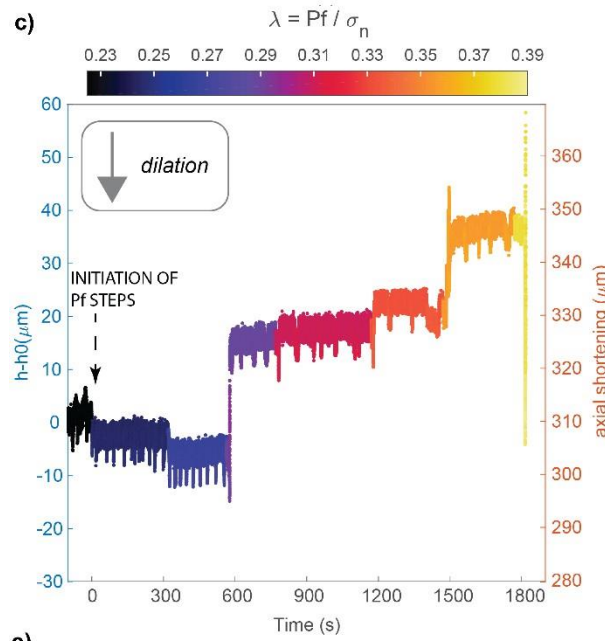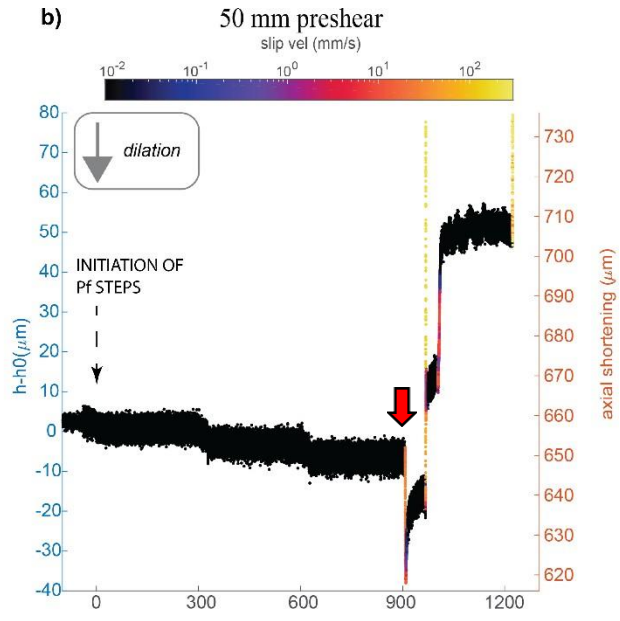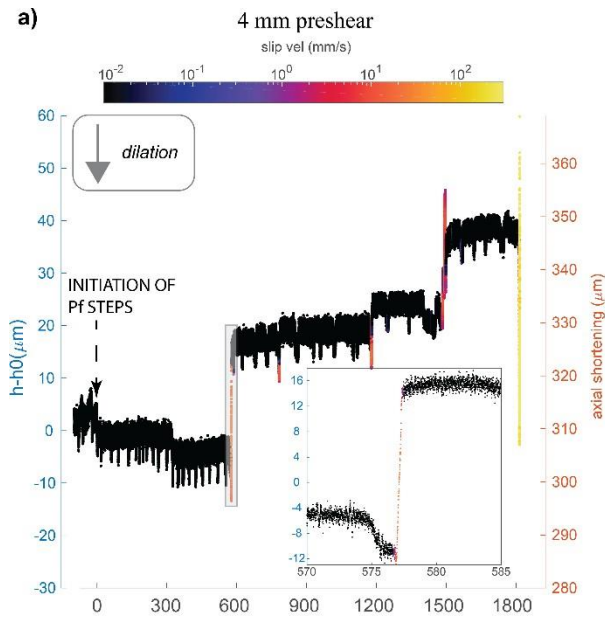
Figure 4.7: Time series for the tests pre-sheared for 4 mm (left panels: exp num. s1825) and 50 mm (right panels: exp num. s1827), highlighting changes in axial displacement with respect to the axial shortening value reached at the onset of fluid pressurization at 0.2 MPa/300s. The symbols are color coded for **(a,b)** the sliding velocity reached during shearing and **(c,d)** the pore fluid factor λ , calculated from the fluid pressure at the injection side (upstream side). The red arrows in **(b,d)** point out the dilation associated with fault slip that possibly masks the overall shear-enhanced compaction, due to the sample geometry. **(e,f)** axial displacement changes during the creep tests as a function of fault slip. Notably, the inset points out the transition from bulk shear compaction to dilation due to the rotary-shear configuration and the cylindrical sample geometry. Blue dashed line represents the periodic oscillations due to the sample rotation here reported for reference.

4.3.4 Hydraulic properties

Diffusion and equilibration of the fluid pressure front during flow through faults and fractures exerts a primary control on the stress state required for fault reactivation and the fault slip behavior, according to the capability of the system to efficiently dissipate fluid overpressure. This efficiency is regulated by crack transmissivity (e.g., *Faulkner et al.*, 2010, 2018; *Rutter and Hackston*, 2017; *Rutter and Macklenburgh, 2018*; *Spagnuolo et al.*, 2018; *Brantut*, 2020). Figure 4.8a shows the evolution transmissivity measured at an effective pressure, P_e, spanning from 4 to 12 MPa and null shear stress, using the steady-state flow and the fluid pressure oscillation technique. Tests conducted with the permeameter on intact core and saw-cut cylinders were made under hydrostatic conditions, whereas transmissivity measurements across paired hollow cylinders during SHIVA tests were made under uniaxial normal loading. Our experimental results show that the transmissivity of the intact cores, equivalent to the permeability of 1m thick intact rock layers is $\sim 10^{-18}$ m^2, which is 2 to 3 orders of magnitude lower than the crack transmissivity measured along saw-cut solid cylinders and hollow cylinders at the investigated P_e intervals and zero accumulated displacement. Therefore, the slipping zone can be regarded as isolated by means of a low permeability rock matrix, implying that macrocrack (=slip surface) transmissivity controls the hydraulic properties of the experimental basalt faults used in this study. In all the tests we do not observe any systematic trend with increasing effective pressure, likely due to the narrow effective pressure interval studied. In some cases, slipping zone transmissivity measured on SHIVA's samples overlaps with the crack transmissivity field of the permeameter, although overall it shows variability of 1 order of magnitude among paired hollow cylinders specimens. This feature probably reflects heterogeneities in initial mean surface roughness or different sample misalignment, which affect the hydraulic aperture and

therefore the hydraulic conductivity of simulated fractures (e.g., *Zimmerman and Bodvarson*, 1996). Nonetheless, after the attainment of the MI, transmissivity decreased down from $5\cdot10^{-16}$ – $6.7\cdot10^{-17}$ m^3 at ~ 11 MPa σ_n' to 2.6 - $6.8\cdot10^{-19}$ m^3 at ~ 6 MPa σ_n' (Table 4.1c; Figure 4.8a,b). This implies that when fault slipped for ~ 800 mm slip, transmissivity decreased significantly down to comparable values as the equivalent transmissivity of 1m thick intact host rock, and differences in hydraulic properties among tested pair samples were minimized.
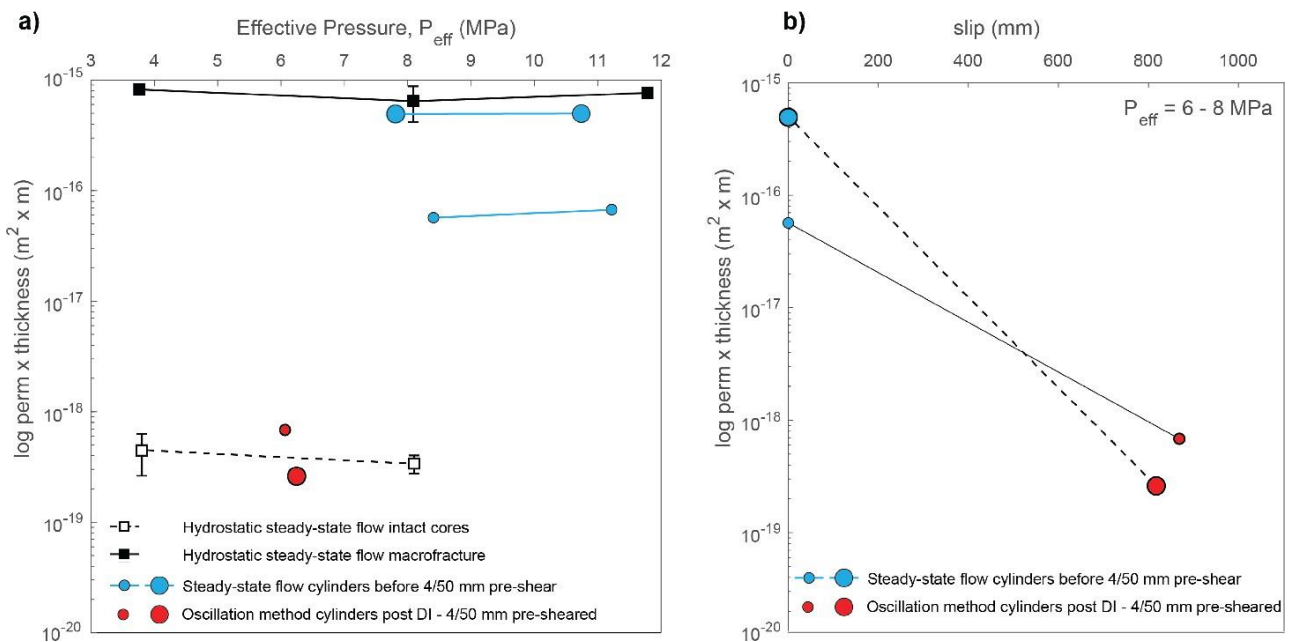

Figure 4.8: **(a)** Compilation of transmissivity measurements (= permeability per unit thickness) under hydrostatic conditions through the permeameter on intact cores (black full squares) and on basalt macrofractures (i.e., saw-cut cylinders, black empty squares) via the steady-state flow method; transmissivity measurements under uniaxial loading conditions on basalt hollow cylinders mounted on SHIVA apparatus, using the steady-state flow technique (light-blue circles) before the pre-shear, and the oscillation fluid pressure method (red circles) after the onset of the main instability (MI). The smaller circles represent the faults pre-sheared for 4 mm, whereas the larger circles depict the faults pre-slid for 50 mm displacement. Intact core permeability is equivalent to the transmissivity of 1 m thick basalt layer. **(b)** evolution in fault transmissivity of the hollow cylinders before and at the end of the test at Pe = 6 – 8 MPa.
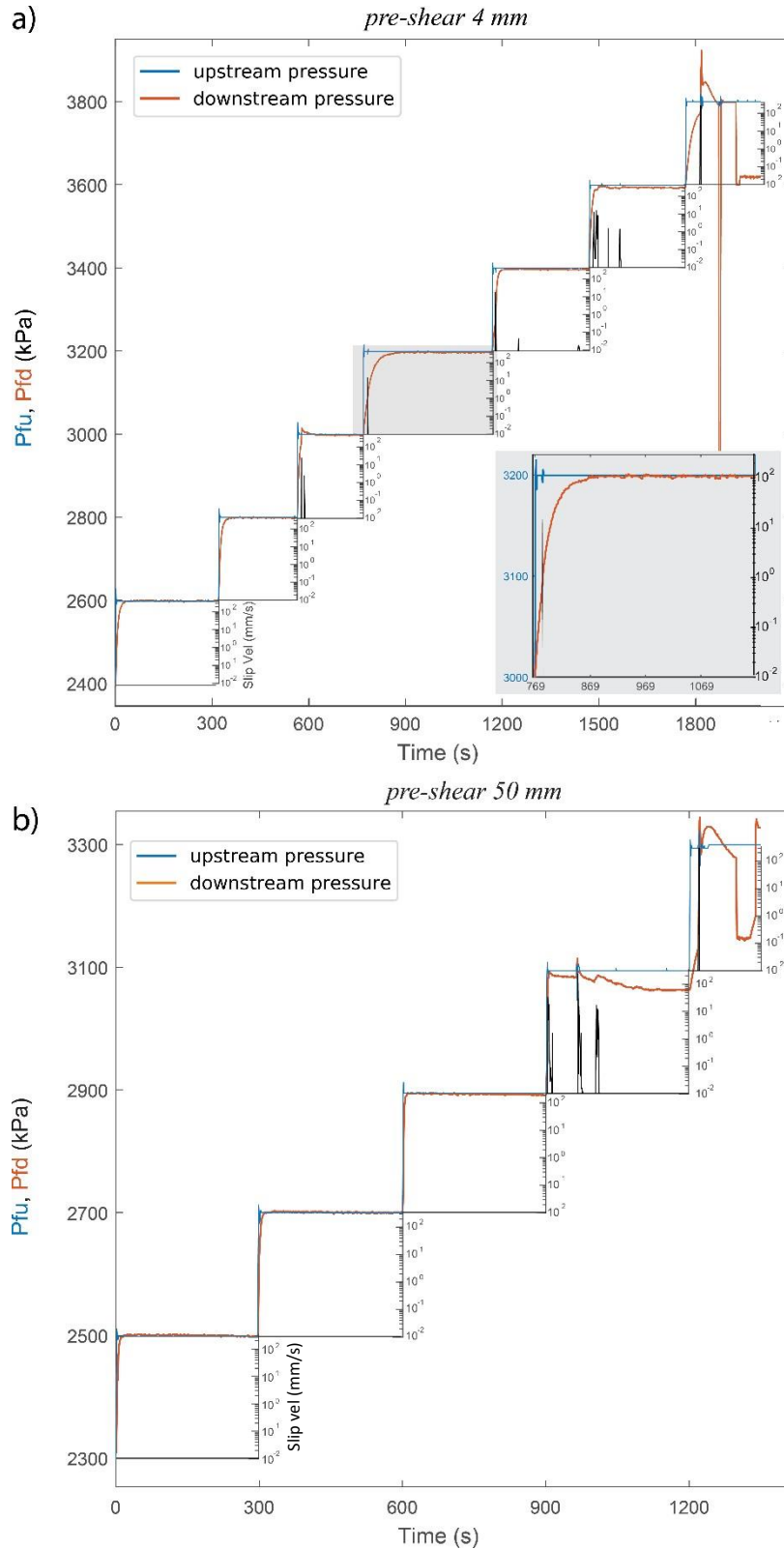
Figure 4.9. Time series showing the fluid injection curves during pressurization at 0.2 MPa/300s for tests pre-sheared for 4 mm **(a)** and 50 mm **(b)**.The blue curve depicts the stepwise fluid pressure increases imposed at the upstream injection side. Orange curves are the response recorded at the downstream side upon the Pf steps, showing the typical diffusion curves that flatten off when the pressure difference between the upstream and downstream side depicted in Figure 4.1, becomes null. Grey in color inset: details of a fluid pressure step increase pointing out the equilibration characteristics of fluid pressure between the upstream and the downstream ISCO syringe pump.
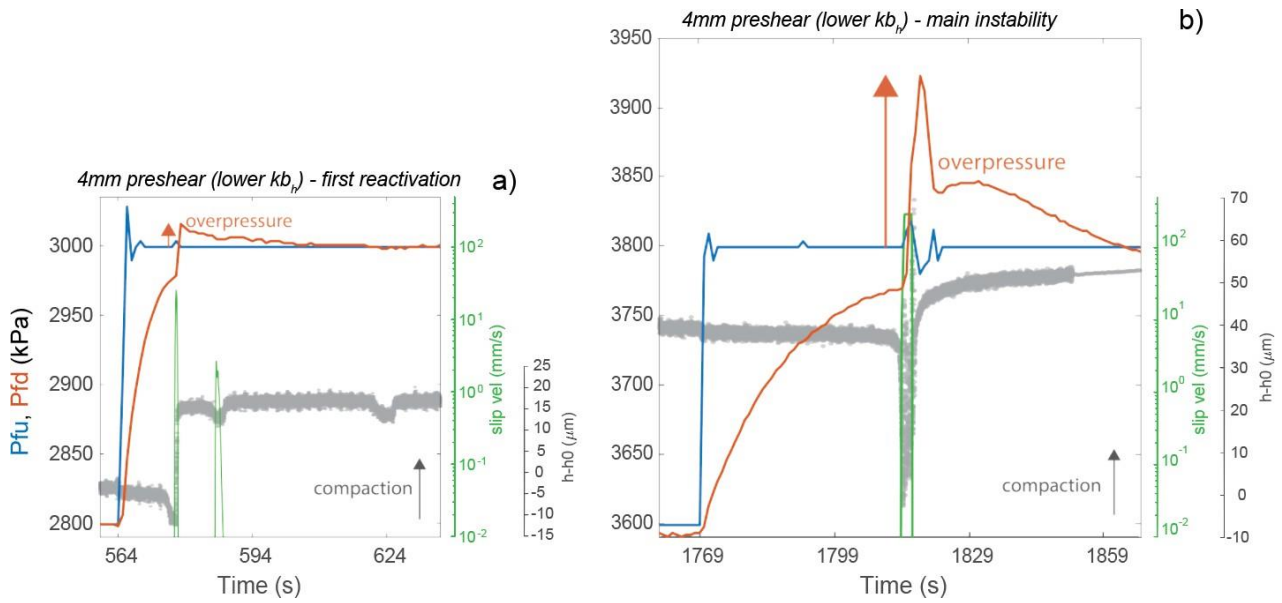
Figure 4.10: Coupled hydraulic and mechanical deformation response in the lower transmissivity and smaller displacement accumulated pre-shear case, following a fluid pressure step increase that led to the onset of the first reactivation event **(a)** and the main instability **(b)**.
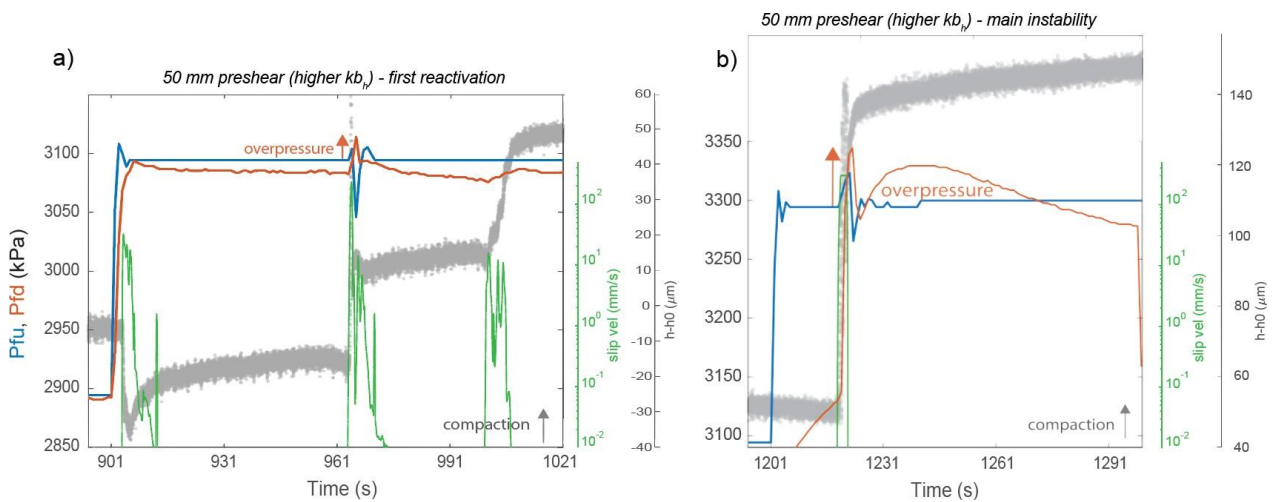
Figure 4.11: Coupled hydraulic and mechanical deformation response affecting the pair sample with higher transmissivity and larger accumulated displacement pre-shear, in response to a fluid pressure step increase that led to the onset of the first reactivation event **(a)** and the dynamic instability **(b)**.

To track changes in hydraulic properties that we observed before and after creep tests (Figure 4.8a), we investigated the change in hydraulic properties during the pressure stepwise increases preceding the main instability by measuring the diffusion time it took for fluid pressure to equilibrate from the outer injection (upstream) to the inner hole (downstream). Change in equilibration times is a proxy for the transport properties evolution along the fault, being inversely related to fault transmissivity. Figure 4.9 shows the fluid pressure

equilibration curves in response to instantaneous fluid pressure increases of ~ 0.2 MPa/300 s (blue curves) for the two experiment types. During the creep experiments, as soon as fluid is injected radially upstream fluid pressure diffuses across the faults with an inverse exponential profile, exhibiting decreasing difference between upstream, P_{fu} and downstream, P_{fd} pressure over time (e.g., inset in Figure 4.9a). In some cases, when the faults become critically stressed, we document the onset of fluid overpressures transients accompanying frictional sliding that perturb the inverse exponential curve generally describing the fluid pressure equilibration with time within the fault (orange arrows in Figures 4.10, 4.11). We define fluid overpressure as the excess in fluid pressure compared to the imposed upstream fluid pressure level, which in our tests was recorded by the downstream fluid pressure transducer closely located to the B valve of Figure 4.1.

For the 4mm test, we find that during the early stages of injection until the first slip event, a sudden Pf increase entails a rapid diffusion of fluid through the fault, with an equilibration time lag t_e ranging from 31 to 44 s. Afterwards, complete equilibrium requires longer times, up to 120 s (Table 4.1d; Figure 4.9a). During the first slip episode, we document the development of a downstream fluid overpressure of ~ 15 kPa accompanying the slip activation (orange arrow, Figure 4.10a), followed by a transient overpressure dissipation time of ~ 15 s. Whereas, an excess in fluid overpressure of ~ 125 kPa is measured during the MI, with longer dissipation time (i.e., ~ 50 s, Figure 4.10b) required to drain excess downstream pressure compared to the first slip event (Figure 4.10a). The increase in dissipation times of fluid overpressure further corroborates the decrease in hydraulic transmissivity during shearing that was quantified through the oscillation pore fluid pressure technique (Figure 4.8). It should be stressed that the recorded fluid overpressure represents the lower limit of the transient fluid pressure increase along the fault, since all the pressure transducers are located outside the slipping zone.

By contrast, the test pre-sheared for 50 mm does not exhibit any appreciable evolution of equilibration times during instantaneous Pf builds-up, and shorter t_e when compared to the test pre-sheared for 4 mm, in the range of 12 to 22 s (Table 4.1d; Figure 4.9b). Those values imply higher hydraulic transmissivity since the beginning of the

pressurization protocol. During such fluid pressure upsteps the fault is in good approximation clamped in place (i.e., slip ~ const = 50 mm; Table 4.1d) until the initiation of the ~ 230 mm/s sliding event preceding MI, recording a fluid overpressure of ~ 20 kPa and short (< 10 s) dissipation times similarly to the 4 mm test (Figure 4.9b; 4.11a). During the MI we document a downstream fluid overpressure of smaller magnitude (i.e., ~ 50 kPa), yet comparable dissipation times (i.e., ~ 50 s) to the 4 mm test (Figure 4.11b vs. Figure 4.10b).

4.4 DISCUSSION

4.4.1 Effect of shear-enhanced fault compaction on the fault slip behavior during fluid pressurization

We have tested in the laboratory the friction response to fluid pressurization leading to dynamic instability of simulated basalt fault interfaces, by developing constant shear stress injection tests in pair samples exhibiting different starting permeability and accumulated slip. Injection of pressurized fluid is expected to produce both a mechanical and a chemical effect on fault weakening (e.g., *Rohmer et al.*, 2016; *Samuelson and Spiers*, 2012). In our tests, the comparable λ and the time relative to the injection initiation required for the occurrence of the first slip event, i.e., $\lambda = 0.29$ after t ~ 580 s and $\lambda = 0.33$ after t ~ 900 s respectively for the 4 mm and 50 mm case (Figures 4.5 a,b and 4.6a,b), suggest a negligible physicochemical effect of fluid-rock/gouge interaction on fault stability. Therefore, in this work only the mechanical effects of pore fluids are taken into account. Overall, we show that the mechanical weakening effect induced by fluid pressurization can overcome the frictional variations predicted in the context of rate- and state- dependent (RS) friction laws. In fact, laboratory data on the RS-dependent frictional properties of the fault rocks tested in these experiments (*Giacomel et al.*, under review), show that under water-saturated conditions, bare surfaces exhibit rate strengthening behavior with increasing sliding velocity, which should foster aseismic creep. However, as we reach the stress state for fault reactivation, each fluid pressure upstep is characterized by transient weakening resulting in accelerated slip events, shortly followed by fault deceleration and arrest, that precede the onset of the main instability (MI) (Figure 4.5). Although the physical mechanism responsible for the wide peak slip-rate range characterizing such slip events (i.e., $V = 20 - 230$ mm/s) is still elusive, we observe that all these events are associated with fault compaction during slip (= shear enhanced compaction). We interpret this abrupt compaction as the result of crushing and collapse of asperity contacts, which are extremely effective dissipation mechanisms of mechanical energy (e.g., *Mandl et al.*, 1977). The crushing and collapse of asperities modify fault surfaces due to frictional wear debris production, which in turn affects the hydraulic properties of the fault zone and dramatically decreases its transmissivity (Eq. (4.6), methods).

The decrease in fault transmissivity associated with shear-enhanced compaction promotes the development of fluid overpressure transients (Figures 4.10, 4.11). This phenomenon has been generally attributed to either fault thermal pressurization or fluid pressure increase by shear compaction, or a combination of both. Whereas thermal pressurization is still matter of debate and cannot be supported here by in-situ temperature measurements, pressure increase by shear compaction has been extensively described in previous experimental (e.g, *Scuderi et al.*, 2015; *French et al.*, 2016; *Proctor et al.*, 2020; *Brantut*, 2020) and theoretical studies (e.g., *Faulkner et al.*, 2018), and can be discussed with our experimental evidences. Fluid overpressure transients represent the poroelastic response to pore volume decreases during shear-enhanced compaction, producing an enhanced mechanical weakening that facilitates the initiation of MI by locally decreasing the effective normal stress acting on the fault. Notably, hydromechanical evidences support the idea that compaction weakening entails significantly larger fluid overpressures during MI in lower transmissivity faults (Figure 4.10b vs. 4.11b), hence exerting a first-order control on the nucleation of earthquake slip especially in low permeability fault rocks (*Proctor et al.*, 2020).

To summarize, our main finding suggests that at the critical stress state for fault reactivation, transient fluid overpressure during fluid pressure stimulation enhances fault weakening that facilitates the onset of seismic slip events (MI). Transient fluid overpressure *a)* occurs due to shear-enhanced compaction that reduces the hydraulic transmissivity, promoting the passage from drained to locally undrained hydrological conditions, and *b)* becomes more pronounced in faults with lower initial hydraulic transmissivity. These fluid overpressure transients produce fault weakening that overcome the rate-strengthening behavior observed for bare rock surfaces on basalts (*Giacomel et al.*, under review). The results presented in this work show relevant changes in the hydraulic properties of faults during deformation and this is a first attempt to monitor such changes continuously during the low to high velocity experiments. Moreover, these results suggest a potential coupled hydromechanical control on frictional properties of basalts bare surfaces that deserves more

investigations. Unfortunately, these main findings are retrieved from just two experiments and the above achievements need to be supported by additional experimental data.

4.4.2 Implications for induced seismicity

In the framework of shallow depth human-induced seismicity, unravelling the physical processes controlling basalt fault slip mode upon fluid pressurization is of paramount importance for seismic risk assessment and mitigation during reservoir stimulation. Our mechanical data show that fluid pressurization gives rise to complex fault motion ranging from aseismic to seismic behavior, with no clear intermediate slip behavior, i.e., slow slip, whose detection would require seismic velocity monitoring during the friction tests. We demonstrate that permeability and structural heterogeneities strongly influence the hydromechanical properties of basaltic fault zones, thus the way stress is transferred from the fluid pressure increase. When upscaled to fluid-injection sites, heterogeneous hydromechanical properties due to fluid pressure, potentially creates heterogeneous distribution of the stress field and control the evolution of seismicity (e.g., *De Barros et al.,* 2016), especially in fracture-dominated systems where optimally and non-optimally oriented fault/fracture sets coexist (*Gischig*, 2015). Due to this, structural and permeability heterogeneities should be considered during seismic monitoring. Unconventional constant shear stress tests conducted in this study, highlight the strategic role of pore fluid pressure diffusion on the stability of sliding, as well as the spatio-temporal correlation between fluid injection and earthquake nucleation jointly with the well-documented mechanism of decreasing effective normal stresses on pre-existing faults. These observations have been also documented at the field scale on the Húsmúli wastewater injection site in basalts (Iceland) (e.g., *Halldorsson et al.*, 2012; *Juncu et al.*, 2018; *Snæbjörnsdóttir et al.*, 2020).

Our main findings suggest that during fluid pressure accumulation within basaltic reservoirs, shear-enhanced compaction along pre-existing faults produces a significant reduction in fault transmissivity promoting the development of fluid overpressure transients that might be larger than the fluid pressure level injected. These overpressure transients

can facilitate seismic slip along a vast gamut of faults including those characterized by a velocity strengthening behavior.

Furthermore, hydromechanical findings from our study coupled with data from Húsmúli site strengthen the idea that, to address the human-induced seismicity issue, injection operations should be aimed at decreasing the entity and duration of fluid pressure transient increases in the injection site, hence reducing fluid pressure heterogeneity along the fault (*Passèlegue et al*., 2018). Achieving this, would potentially produce the beneficial effect of constraining the rupture front propagation close to the pressure front besides decreasing the magnitude and seismicity rate as directly observed in the Húsmúli site, whereby limiting the injection rates reduced the seismic episodes with magnitude larger than 2 from 96 in 2011 to 1 in 2018 (*Aradóttir et al.*, 2018).

4.5 CONCLUSIONS

We have investigated experimentally the hydromechanical response and evolution of nearly critically stressed faults stimulated by fluid injection. We captured the influence of increasing fluid pressure on the loading path and slip behavior of experimental basalt fault interfaces, by designing conventional constant rate experiments and unconventional creep tests at constant shear stress on samples pair differing in the initial transmissivity and accumulated slip. Our conclusions of this preliminary study are:

1- At the critical stress for fault reactivation, shear-enhanced compaction can generate transient fluid overpressures larger than those generated in the up-stream, i.e. imposed by the operator. Transient fluid overpressures facilitated by fault compaction are fostered by the fault transmissivity decrease and promote the transition from drained to locally undrained conditions;

2- Shear-enhanced compaction under fluid injection conditions exerts a first-order control on frictional stability of basalt rocks: fluid overpressure transients locally decrease the effective normal stress acting on the fault, inducing mechanical weakening. These overpressure transients can promote seismic slip along a vast gamut of faults including those characterized by a velocity strengthening behavior, especially in low transmissivity faults, wherein fluid overpressure effect is more pronounced;

3- Collectively, our observations indicate that to mitigate the risks of induced seismicity in basalt sites, fluid pressure gradients around the injection area should be minimized during field-scale injection operations, implying that injection rates should be limited depending on the hydraulic diffusivity of the field area around the fault/fracture network.

REFERENCES

Aradóttir, E. S. & Hjálmarsson, E. CarbFix – public engagement and transparency. *Energy Procedia* **146**, 115–120 (2018).

Atkinson, G. M., Eaton, D. W., Ghofrani, H., Walker, D., Cheadle, B., Schultz, R., ... & Liu, Y. (2016). Hydraulic fracturing and seismicity in the Western Canada Sedimentary Basin. *Seismological research letters*, *87*(3), 631-647.

Bernabé, Y., Mok, U. & Evans, B. 2006. A note on the oscillating flow method for measuring rock permeability. International Journal of Rock Mechanics and Mining Sciences, 43, 311-316.

Blanpied, M. L., T. E. Tullis, and J. D. Weeks (1998), Effects of slip, slip rate, and shear heating on the friction of granite, *Journal of Geophysical Research B: Solid Earth*, *103*(1), 489-511.

Brantut, N. (2020). Dilatancy-induced fluid pressure drop during dynamic rupture: Direct experimental evidence and consequences for earthquake dynamics. *Earth and Planetary Science Letters*, *538*, 116179.

Byerlee, J. (1978). Friction of rocks. In *Rock friction and earthquake prediction* (pp. 615-626). Birkhäuser, Basel.

Cappa, F., & Rutqvist, J. (2011). Modeling of coupled deformation and permeability evolution during fault reactivation induced by deep underground injection of CO2. *International Journal of Greenhouse Gas Control*, *5*(2), 336-346.

Cappa, F., Scuderi, M. M., Collettini, C., Guglielmi, Y., & Avouac, J. P. (2019). Stabilization of fault slip by fluid injection in the laboratory and in situ. *Science advances*, *5*(3), eaau4065.

Collettini, C., G. Di Stefano, B. Carpenter, P. Scarlato, T. Tesei, S. Mollo, F. Trippetta, C. Marone, G. Romeo, and L. Chiaraluce (2014), A novel and versatile apparatus for brittle rock deformation, *International Journal of Rock Mechanics and Mining Sciences*, *66*, 114-123, doi:10.1016/j.ijrmms.2013.12.005.

De Barros, L., Daniel, G., Guglielmi, Y., Rivet, D., Caron, H., Payre, X., et al. (2016). Fault structure, stress, or pressure control of the seismicity in shale? insights from a controlled experiment of fluid-induced fault reactivation. *Journal of Geophysical Research: Solid Earth*, *121*, 4506–4522. https://doi.org/10.1002/2015JB012633

Dieterich, J. H. (1979). Modeling of rock friction 1. Experimental results and constitutive equations. Journal of Geophysical Research, 84(B5), 2161–2168. https://doi.org/10.1029/JB084iB05p02161

Di Toro, G., Niemeijer, A., Tripoli, A., Nielsen, S., Di Felice, F., Scarlato, P., ... & Smith, S. (2010). From field geology to earthquake simulation: a new state-of-the-art tool to investigate rock friction during the seismic cycle (SHIVA). *Rendiconti Lincei*, *21*(1), 95-114.

Ellsworth, W. L. (2013). Injection-induced earthquakes. *Science*, *341*(6142).

Ellsworth, W. L., Giardini, D., Townend, J., Ge, S., & Shimamoto, T. (2019). Triggering of the Pohang, Korea, earthquake (Mw 5.5) by enhanced geothermal system stimulation. *Seismological Research Letters*, *90*(5), 1844-1858.

Faoro, I., Niemeijer, A., Marone, C., & Elsworth, D. (2009). Influence of shear and deviatoric stress on the evolution of permeability in fractured rock. Journal of Geophysical Research, 114, B01201. https://doi.org/10.1029/2007JB005372

Faulkner, D. R. (1997). *The role of clay-bearing fault gouges in controlling fluid pressures in fault zones: implications for fault mechanics*.

Faulkner, D. R., & Rutter, E. H. (2000). Comparisons of water and argon permeability in natural clay-bearing fault gouge under high pressure at 20° C. *Journal of Geophysical Research: Solid Earth*, *105*(B7), 16415-16426.

Faulkner, D. R., Jackson, C. A. L., Lunn, R. J., Schlische, R. W., Shipton, Z. K., Wibberley, C. A. J., & Withjack, M. O. (2010). A review of recent developments concerning the structure, mechanics and fluid flow properties of fault zones. *Journal of Structural Geology*, *32*(11), 1557-1575.

Faulkner, D. R., Sanchez-Roa, C., Boulton, C., & Den Hartog, S. A. M. (2018). Pore fluid pressure development in compacting fault gouge in theory, experiments, and nature. *Journal of Geophysical Research: Solid Earth*, *123*(1), 226-241.

Ferri, F., Di Toro, G., Hirose, T., Shimamoto, T., 2010. Evidence of thermal pressurization in high-velocity friction experiments on smectite-rich gouges. Terra Nova22, 347–353.

Fischer, G. J. (1987). Dilatancy and permeability in rock deformation.

Fischer, G. J. (1992). The determination of permeability and storage capacity: Pore pressure oscillation method. In *International Geophysics* (Vol. 51, pp. 187-211). Academic Press.

French, M. E., Zhu, W., & Banker, J. (2016). Fault slip controlled by stress path and fluid pressurization rate. *Geophysical Research Letters*, *43*(9), 4330-4339.

Giacomel, P., Ruggieri, R., Scuderi, M.M., Spagnuolo, E., Di Toro, G., and Collettini, C. Frictional strength, stability, and healing properties of basalt-built experimental faults. Submitted to *Tectonophysics* (August, 2020).

Giacomel, P., Spagnuolo, E., Nazzari, M., Marzoli, A., Passelègue, F., Youbi, N., & Di Toro, G. (2018). Frictional Instabilities and Carbonation of Basalts Triggered by Injection of Pressurized H2O-and CO2-Rich Fluids. *Geophysical research letters*, *45*(12), 6032-6041.

Gischig, V. S. (2015). Rupture propagation behavior and the largest possible earthquake induced by fluid injection into deep reservoirs. *Geophysical Research Letters*, *42*(18), 7420-7428.

Grigoli, F., Cesca, S., Priolo, E., Rinaldi, A. P., Clinton, J. F., Stabile, T. A., ... & Dahm, T. (2017). Current challenges in monitoring, discrimination, and management of induced seismicity related to underground industrial activities: A European perspective. *Reviews of Geophysics*, *55*(2), 310-340.

Guglielmi, Y., Cappa, F., Avouac, J. P., Henry, P., & Elsworth, D. (2015). Seismicity triggered by fluid injection–induced aseismic slip. *Science*, *348*(6240), 1224-1226.

Halldorsson, B., Olafsson, S., Snaebjörnsson, J. T., Sigurosson, S. U., Rupakhety, R., & Sigbjörnsson, R. (2012). On the effects of induced earthquakes due to fluid injection at hellisheidi geothermal power plant, Iceland. *Proc. 15th WCEE, Lissabon, Portugal*.

Healy, J., Rubey, W., Griggs, D., & Raleigh, C. (1968). The Denver earthquakes. *Science*, *161*(3848), 1301–1310.

Heap, M. J., Baud, P., Meredith, P. G., Vinciguerra, S., & Reuschlé, T. (2014). The permeability and elastic moduli of tuff from Campi Flegrei, Italy: Implications for ground deformation modelling. *Solid Earth*, *5*(1), 25– 44. https://doi.org/10.5194/se-5-25-2014

Horton, S. (2012). Disposal of hydrofracking waste fluid by injection into subsurface aquifers triggers earthquake swarm in central Arkansas with potential for damaging earthquake. *Seismological Research Letters*, *83*(2), 250-260.

Hubbert, M. K., & Rubey, W. W. (1959). Role of fluid pressure in mechanics of overthrust faulting I. Mechanics of fluid-filled porous solids and its application to overthrust faulting. *Geological Society of America Bulletin*, *70*(2), 115–166.

Ikari, M. J., Marone, C., & Saffer, D. M. (2011). On the relation between fault strength and frictional stability. *Geology*, *39*(1), 83-86.
IPCC Special Report (2018). Global Warming of 1.5 ∘C. Available online at: https://www.ipcc.ch/sr15/

Jaeger, J. C., and N. G. W. Cook (1979), *Fundamentals of Rock Mechanics*, Chapman and Hall, London, U. K.

Juncu, D., Árnadóttir, T., Geirsson, H., Guðmundsson, G. B., Lund, B., Gunnarsson, G., ... & Michalczewska, K. (2020). Injection-induced surface deformation and seismicity at the Hellisheidi geothermal field, Iceland. *Journal of Volcanology and Geothermal Research*, *391*, 106337.

Keranen, K. M., Savage, H. M., Abers, G. A., & Cochran, E. S. (2013). Potentially induced earthquakes in Oklahoma, USA: Links between wastewater injection and the 2011 Mw 5.7 earthquake sequence. *Geology*, *41*(6), 699-702.

Langenbruch, C., & Zoback, M. D. (2016). How will induced seismicity in Oklahoma respond to decreased saltwater injection rates?. *Science advances*, *2*(11), e1601542.

Lee, K. K., Ellsworth, W. L., Giardini, D., Townend, J., Ge, S., Shimamoto, T., ... & Chang, C. (2019). Managing injection-induced seismic risks. *Science*, *364*(6442), 730-732.

Mair, K., & Marone, C. (1999). Friction of simulated fault gouge for a wide range of velocities and normal stresses. *Journal of Geophysical Research: Solid Earth*, *104*(B12), 28899-28914.

Mandl, G., De Jong, L. N. J., & Maltha, A. (1977). Shear zones in granular materials. *Rock Mechanics*, *9*(2-3), 95–144. https://doi.org/10.1007/BF01237876

Marone, C. (1998). Laboratory-derived friction laws and their application to seismic faulting. Annual Review of Earth and Planetary Sciences, 26(1), 643–696. https://doi.org/10.1146/annurev.earth.26.1.643

Morrow, C. A., & Byerlee, J. D. (1989). Experimental studies of compaction and dilatancy during frictional sliding on faults containing gouge. *J. Struct. Geol*, *11*(7), 815-825.

Niemeijer, A., Di Toro, G., Nielsen, S., & Di Felice, F. (2011). Frictional melting of gabbro under extreme experimental conditions of normal stress, acceleration, and sliding velocity. *Journal of Geophysical Research: Solid Earth*, *116*(B7).

Nielsen, S., Spagnuolo, E., & Violay, M. (2012). Composite sample mount assembly (SAMOA): The ultimate sample preparation for rotary shear experiments. *INGV Rapporti Tecnici. ISSN*, 2039-741.

Ogwari, P. O., DeShon, H. R., & Hornbach, M. J. (2018). The Dallas-Fort Worth airport earthquake sequence: Seismicity beyond injection period. *Journal of Geophysical Research: Solid Earth*, *123*, 553–563. https://doi.org/10.1002/2017jb015003

Paterson, M. S., & Wong, T. F. (2005). *Experimental rock deformation-the brittle field*. Springer Science & Business Media.

Passelègue, F. X., Brantut, N., & Mitchell, T. M. (2018). Fault reactivation by fluid injection: Controls from stress state and injection rate. *Geophysical Research Letters*, *45*(23), 12-837.

Proctor, B., Lockner, D. A., Kilgore, B. D., Mitchell, T. M., & Beeler, N. M. (2020). Direct evidence for fluid pressure, dilatancy, and compaction affecting slip in isolated faults. *Geophysical Research Letters*, *47*(16), e2019GL086767.

Raleigh, C. B., Healy, J. H., & Bredehoeft, J. D. (1976). An experiment in earthquake control at Rangely, Colorado. *Science*, *191*(4233), 1230-1237.

Rohmer, J., Pluymakers, A., & Renard, F. (2016). Mechano-chemical interactions in sedimentary rocks in the context of CO2 storage: Weak acid, weak effects?. *Earth-Science Reviews*, *157*, 86-110.

Rothert, E., & Shapiro, S. A. (2007). Statistics of fracture strength and fluid-induced microseismicity. *Journal of Geophysical Research: Solid Earth*, *112*(B4).

Rubinstein, J. L., Ellsworth, W. L., McGarr, A., & Benz, H. M. (2014). The 2001–present induced earthquake sequence in the Raton basin of northern New Mexico and Southern Colorado. *Bulletin of the Seismological Society of America*, *104*, 2162–2181.

Ruina, A. (1983). Slip instability and state variable friction laws. Journal of Geophysical Research, 88(B12), 10,359–10,370. https://doi.org/10.1029/JB088iB12p10359

Rutter, E., & Hackston, A. (2017). On the effective stress law for rock-on-rock frictional sliding, and fault slip triggered by means of fluid injection. *Philosophical Transactions of the Royal Society A: Mathematical, Physical and Engineering Sciences*, *375*(2103), 20160001.

Rutter, E. H., & Mecklenburgh, J. (2018). Influence of normal and shear stress on the hydraulic transmissivity of thin cracks in a tight quartz sandstone, a granite, and a shale. *Journal of Geophysical Research: Solid Earth*, *123*(2), 1262-1285.

Samuelson, J., & Spiers, C. J. (2012). Fault friction and slip stability not affected by CO2 storage: Evidence from short-term laboratory experiments on North Sea reservoir sandstones and caprocks. *International Journal of Greenhouse Gas Control*, *11*, S78-S90.

Samuelson, J., Elsworth, D., & Marone, C. (2009). Shear-induced dilatancy of fluid-saturated faults: Experiment and theory. *Journal of Geophysical Research: Solid Earth*, *114*(B12).

Scholz, C. H. (2019). *The mechanics of earthquakes and faulting*. Cambridge university press.

Scuderi, M. M., & Collettini, C. (2018). Fluid injection and the mechanics of frictional stability of shale-bearing faults. *Journal of Geophysical Research: Solid Earth*, *123*(10), 8364-8384.

Scuderi, M. M., Carpenter, B. M., Johnson, P. A., & Marone, C. (2015). Poromechanics of stick-slip frictional sliding and strength recovery on tectonic faults. *Journal of Geophysical Research: Solid Earth*, *120*(10), 6895-6912.

Scuderi, M. M., Collettini, C., & Marone, C. (2017). Frictional stability and earthquake triggering during fluid pressure stimulation of an experimental fault. *Earth and Planetary Science Letters*, *477*, 84-96.

Segall, P., & Rice, J. R. (1995). Dilatancy, compaction, and slip instability of a fluid-infiltrated fault. *Journal of Geophysical Research: Solid Earth*, *100*(B11), 22155-22171.

Segall, P., Rubin, A. M., Bradley, A. M., & Rice, J. R. (2010). Dilatant strengthening as a mechanism for slow slip events. *Journal of Geophysical Research: Solid Earth*, *115*(B12).
Shimamoto T, Tsutsumi A (1994) A new rotary-shear high-speed frictional testing machine: its basic design and scope of research. Struct Geol 39:65–78 (in Japanese with English abstract)

Sibson, R.H., 1986. Earthquakes and rock deformation in crustal fault zones. Annu. Rev. Earth Planet. Sci.14, 149–175. http://dx.doi.org/10.1146/annurev.ea.14.050186.001053

Snæbjörnsdóttir, S. Ó., Sigfússon, B., Marieni, C., Goldberg, D., Gislason, S. R., & Oelkers, E. H. (2020). Carbon dioxide storage through mineral carbonation. *Nature Reviews Earth & Environment*, 1-13.

Snæbjörnsdóttir, S. Ó., Tómasdóttir, S., Sigfússon, B., Aradóttir, E. S., Gunnarsson, G., Niemi, A., ... & Franzson, H. (2018). The geology and hydrology of the CarbFix2 site, SW-Iceland. *Energy Procedia*, *146*, 146-157.

Spagnuolo, E., Violay, M., Nielsen, S., Cornelio, C., & Di Toro, G. (2018). Frictional instability under fluid stimulation: insights from load-con-trolled experiments on pre-existing faults.

Tanikawa, W., Sakaguchi, M., Tadai, O., & Hirose, T. (2010). Influence of fault slip rate on shear-induced permeability. Journal of Geophysical Research, 115, B07412. https://doi.org/10.1029/2009JB007013

Terzaghi, K. (1925). Erdbaumechanik auf bodenphysikalischer Grundlage.

Townend, J., & Zoback, M. D. (2000). How faulting keeps the crust strong. *Geology*, *28*(5), 399-402.

Trippetta, F., Carpenter, B. M., Mollo, S., Scuderi, M. M., Scarlato, P., & Collettini, C. (2017). Physical and transport property variations within carbonate-bearing fault zones: insights from the Monte Maggio Fault (Central Italy). *Geochemistry, Geophysics, Geosystems*, *18*(11), 4027-4042.

Vilarrasa Riaño, V., Carrera, J., Olivella, S., Rutqvist, J., & Laloui, L. (2019). Induced seismicity in geologic carbon storage. *Solid Earth*, *10*(ARTICLE), 871-892.

Violay, M., Di Toro, G., Nielsen, S., Spagnuolo, E., Burg, J.P., 2015. Thermo-mechanical pressurization of experimental faults in cohesive rocks during seismic slip. Earth Planet. Sci. Lett.429, 1–10.

Violay, M., Nielsen, S., Gibert, B., Spagnuolo, E., Cavallo, A., Azais, P., ... & Di Toro, G. (2014). Effect of water on the frictional behavior of cohesive rocks during earthquakes. *Geology*, *42*(1), 27-30.

Violay, M., Nielsen, S., Spagnuolo, E., Cinti, D., Di Toro, G., & Di Stefano, G. (2013). Pore fluid in experimental calcite-bearing faults: Abrupt weakening and geochemical signature of co-seismic processes. *Earth and planetary science letters*, *361*, 74-84.

Walsh III, F. R., & Zoback, M. D. (2016). Probabilistic assessment of potential fault slip related to injection-induced earthquakes: Application to north-central Oklahoma, USA. *Geology*, *44*(12), 991-994.

Weeks, J. D. (1993). Constitutive laws for high-velocity frictional sliding and their influence on stress drop during unstable slip. *Journal of Geophysical Research: Solid Earth*, *98*(B10), 17637-17648.

Witherspoon, P. A., Wang, J. S., Iwai, K., & Gale, J. E. (1980). Validity of cubic law for fluid flow in a deformable rock fracture. *Water resources research*, *16*(6), 1016-1024.

Zimmerman, R. W., & Bodvarsson, G. S. (1996). Hydraulic conductivity of rock fractures. *Transport in porous media*, *23*(1), 1-30.

Zoback, M. D., & Gorelick, S. M. (2012). Earthquake triggering and large-scale geologic storage of carbon dioxide. *Proceedings of the National Academy of Sciences*, *109*(26), 10164-10168.

5. Conclusions: main findings, suggestions for further research, and technical challenges

This thesis reports the results from laboratory investigations designed for determining the frictional behavior of simulated basalt-bearing faults, namely gouge and bare rock surfaces, which represent the two end members that can be found in basalt volcano-tectonic environments or in the vicinity of in-situ geoenergy storage sites. Regarding the natural or human-induced earthquake nucleation processes in basaltic rocks, I addressed the following societally relevant issues, i.e., (Chapter 2) how fault structure affects the friction stability under room-dry and water-saturated conditions; (Chapter 3) the role of the degree of alteration of rocks and the fluid chemistry on the onset of dynamic frictional instabilities; (Chapter 4) the controls of hydromechanical changes on the fault slip behavior during fluid pressurization.

In particular, my study illustrates the strategic contribution of basalt fault structure development on the evolution of rate-and-state friction constitutive properties: simulated gouge progressively switches to velocity weakening behavior following cataclasis, grain size reduction and shear localization that render faults more prone to host seismic ruptures; on the contrary, bare surfaces transition to rate-strengthening behavior due to dilatancy processes favored by gouge development, thereby limiting frictional instabilities and/or suppressing unstable fault slip. Short-term (~ 40-60 mins) creep experiments at constant shear stress on initially bare rock surfaces show that the state of alteration of basalts, quantified by the mean loss on ignition of the fault interfaces, as well as the chemistry of the injection fluids (i.e., distilled H_2O, Ar, CO_2 and CO_2-rich H_2O) do not exert a significant effect on triggering seismic slip events, which depends mainly on the mechanical effects of the pressurized fluids. In this regard, we have demonstrated that the occurrence of seismic slip events can be intimately related to the fluid pathways restriction across the fault during shear-enhanced compaction upon fluid pressurization, especially the lower the initial transmissivity of faults. Collectively, the heterogeneous hydromechanical properties during fluid injection coupled with the heterogeneous intrinsic frictional properties envisages a

heterogeneous seismicity distribution at the field scale. Such remarks emphasize the criticality to carefully characterize the stress field of the fault/fracture network surrounding the injection site before embarking in industrial-scale fluid injection projects, in order to keep the fluid pressure below the critical stress state for fault reactivation. Consequently, limiting the injection rates according to the storage site capacity is an effective strategy for reducing the seismicity rates in basaltic-dominated environments, as documented during the wastewater injection operations conducted in the Húsmúli field in Iceland (*Aradóttir* et al., 2018).

Based on the above considerations, this study has raised some unresolved issues, opening new roads for further research, as follows.

1) <u>Unravelling the short-living slip events preceding the runaway ruptures during the creep tests</u>

The fault short-living slip episodes observed in Chapter 4 preceding seismic slip, are characterized by slip acceleration with peak slip rates from ~ 20 to 230 mm /s for faults pre-sheared for 4 and 50 mm, respectively. This acceleration phase was followed by rapid deceleration and arrest. The mechanical processes responsible for the wide range of peak rates we document, as well as the deceleration phase are still poorly understood. Such slip characteristics might be explained in terms of the competition between the effect of fluid pressure on fault slip stability, when evaluated in the framework of the rate- and state-friction laws, and the mechanical weakening effect of fluid pressure during fault deformation, when assessed using a creep approach. In this regard, the hydromechanical properties are intimately related to the fault structure evolution during shearing upon fluid pressurization. For instance, previous works show that fault structure development within the fault during deformation can modify the way fluid diffuses through the fault, thereby affecting their hydromechanical properties, hence the observed fault slip behavior (e.g., *Scuderi and Collettini*, 2018).

To fill this knowledge gap, *(i)* additional velocity stepping experiments should be performed at pore fluid factors λ (=fluid pressure/normal stress ratio), encompassing the conditions reached during the creep tests of Chapter 3 and 4, since it has been

experimentally demonstrated that λ can affect the friction constitutive parameters (*Scuderi et al.*, 2016); *(ii)* collecting post-mortem microstructures would allow to develop a micromechanical model and thereby, better assess the fault slip behavior under fluid pressure conditions. Despite collecting microstructures in a rotary-shear apparatus would represent a challenge especially when initially bare rock surfaces are pressurized (e.g., *Giacomel et al.*, 2018), slowly depressurizing the fault with stepwise fluid pressure decreases accompanied by corresponding normal stress decreases to keep the effective normal stress constant, might help to limit the water flushing-out of the gouge layer produced during shearing, hence to better preserve the fault microstructure after sample unloading.

2) Friction experiments with pressurized CO_2-rich fluids

Mineral carbonation due to CO_2-rich H_2O – basalts interaction has been extensively studied, both at the outcrop scale (e.g., *Walker et al.*, 2012) and in pilot CO_2 storage projects (*Gislason and Oelkers*, 2014; *Matter et al.*, 2016). Newly formed micrometric carbonate patches were also detected after interaction of simulated basalt interfaces with CO_2-rich water during recent short-term laboratory friction tests (*Giacomel et al.*, 2018: Chapter 3), testifying the extremely efficient kinetic of mineral carbonation in such mafic rocks. This property is drawing increasing attention from oil companies, such as Petrobras (e.g., *Rockett et al.*, 2013) in the framework of the enhanced oil recovery. However, the frictional properties of basalts resulting from long-term fluid-rock interaction has been so far poorly investigated. Further tests involving shearing of *a)* carbonate gouge layers sandwiched between basalts bare surfaces; *b)* basalt fault planes already mineralized either naturally or in the laboratory, and *c)* gouge layers with variable proportions between basalts and carbonates, would be required to fill this knowledge gap.

3) Propagation phase of injection-induced earthquakes

This thesis was entirely focused on the frictional properties of basalt faults, notably the earthquake nucleation phase. In the context of human-induced seismicity due to underground fluid injection, seismic monitoring is a viable method to record short-living

microseismic pulses associated with fluid injection, as done for instance in the Groeningen gas field (*van Thienen-Visser, K., & Breunese, J. N.* ,2015). Inverse modeling allows to retrieve the vast gamut of earthquake-like velocity functions possibly related to such events, which in turn can be experimentally reproduced through the rotary-shear apparatus SHIVA (*Harbord et al.*, 2019a). These tests would help to better understand the dynamic weakening and seismic slip propagation following the earthquake nucleation phase and therefore refine the seismic risk assessment in basalt-hosted geo-energy storage sites.

To conclude, the creep experiments from Chapter 4 have raised a few technical challenges that need to be addressed to produce high-quality data required for significant scientific advancement, as listed below:

- The flawed control of the electromechanical piston employed for the application of the normal load, that in turn determines significant oscillations in shear stress (~ 0.5 MPa);
- The oscillation of the LVDT shortening with displacement, with the periodicity dictated by the hollow cylinder mean radius that might mask the actual fault compaction/dilation. Addressing this issue requires either positioning the LVDT closer to the sample chamber, which is a rather challenging solution in the horizontal SHIVA's setup, or installing a set of capacity gap sensors close to the slip surface (*Harbord et al.*, 2019b);
- The possible attenuation of fluid pressure changes following fault dilation/compaction due to the direct connectivity of the fluid pressure control system to the fault zone. This problem can be solved by installing a pressure transducer close to the fault slip interface as in *Proctor et al.* (2020).

REFERENCES

Giacomel, P., Spagnuolo, E., Nazzari, M., Marzoli, A., Passelegue, F., Youbi, N., & Di Toro, G. (2018). Frictional Instabilities and Carbonation of Basalts Triggered by Injection of Pressurized H_2O-and CO_2-Rich Fluids. *Geophysical research letters*, *45*(12), 6032-6041.

Gislason, S. R., & Oelkers, E. H. (2014). Carbon storage in basalt. *Science*, *344*(6182), 373-374.

Harbord, C., Spagnuolo, E., & Di Toro, G. (2019). Scaling of the dynamic slip weakening distance with acceleration during laboratory earthquake-like slip events. *AGUFM*, *2019*, MR23E-0166.

Harbord, C., Spagnuolo, E., Tisato, N., Stefano, G. D., & Toro, G. D. (2019, January). A new module designed to study seismic attenuation in large displacement experimental faults. In *Geophysical Research Abstracts* (Vol. 21).

Juncu, D., Árnadóttir, T., Geirsson, H., Guðmundsson, G. B., Lund, B., Gunnarsson, G., ... & Michalczewska, K. (2020). Injection-induced surface deformation and seismicity at the Hellisheidi geothermal field, Iceland. *Journal of Volcanology and Geothermal Research*, *391*, 106337.

Matter, J. M., Stute, M., Snæbjörnsdottir, S. Ó., Oelkers, E. H., Gislason, S. R., Aradottir, E. S., ... & Axelsson, G. (2016). Rapid carbon mineralization for permanent disposal of anthropogenic carbon dioxide emissions. *Science*, *352*(6291), 1312-1314.

Proctor, B., Lockner, D. A., Kilgore, B. D., Mitchell, T. M., & Beeler, N. M. (2020). Direct evidence for fluid pressure, dilatancy, and compaction affecting slip in isolated faults. *Geophysical Research Letters*, *47*(16), e2019GL086767.

Rockett, G. C., Ketzer, J. M. M., Ramírez, A., & Van den Broek, M. (2013). CO2 Storage Capacity of Campos Basin's Oil Fields, Brazil. *Energy Procedia*, *37*, 5124-5133.

Scuderi, M. M., & Collettini, C. (2016). The role of fluid pressure in induced vs. triggered seismicity: Insights from rock deformation experiments on carbonates. *Scientific reports*, *6*(1), 1-9.

Scuderi, M. M., & Collettini, C. (2018). Fluid injection and the mechanics of frictional stability of shale-bearing faults. *Journal of Geophysical Research: Solid Earth*, *123*(10), 8364-8384.

van Thienen-Visser, K., & Breunese, J. N. (2015). Induced seismicity of the Groningen gas field: History and recent developments. *The Leading Edge*, *34*(6), 664-671.

Walker, R. J., Holdsworth, R. E., Imber, J., & Ellis, D. (2012). Fault-zone evolution in layered basalt sequences: A case study from the Faroe Islands, NE Atlantic margin. *Bulletin*, *124*(7-8), 1382-1393.

APPENDIX 1. Geometrical model

Technical correction to the applied normal stress for rotary-shear experiments on hollow cylinders in the presence of pressurized fluids

A series of friction experiments were conducted on basalt hollow cylinders pair samples at constant displacement rate V = 10 μm/s and pore fluid factor λ = Pf/σ_n ranging from 0 to 0.39. The experiment at λ = 0 was carried out under dry-vacuum conditions in order to get the steady-state sliding friction coefficient μ devoid of any other environmental parameters that might affect the frictional strength of basalt faults (e.g., room humidity, the fluid chemistry and the fluid pressure). Shear steady-state values τ_{ss} were plotted against the effective normal stress, which is defined as σ_n' = σ_n − α Pf, assuming α = 1 (*Terzaghi*, 1925). Our data reveal an inverse relationship between the steady-state friction coefficient μ and λ: for a given effective normal stress, τ_{ss} decreases considerably at increasing λ, with μ ranging from 0.65 at λ = 0 to 0.32 at λ = 0.39 (Figure S1.1a).
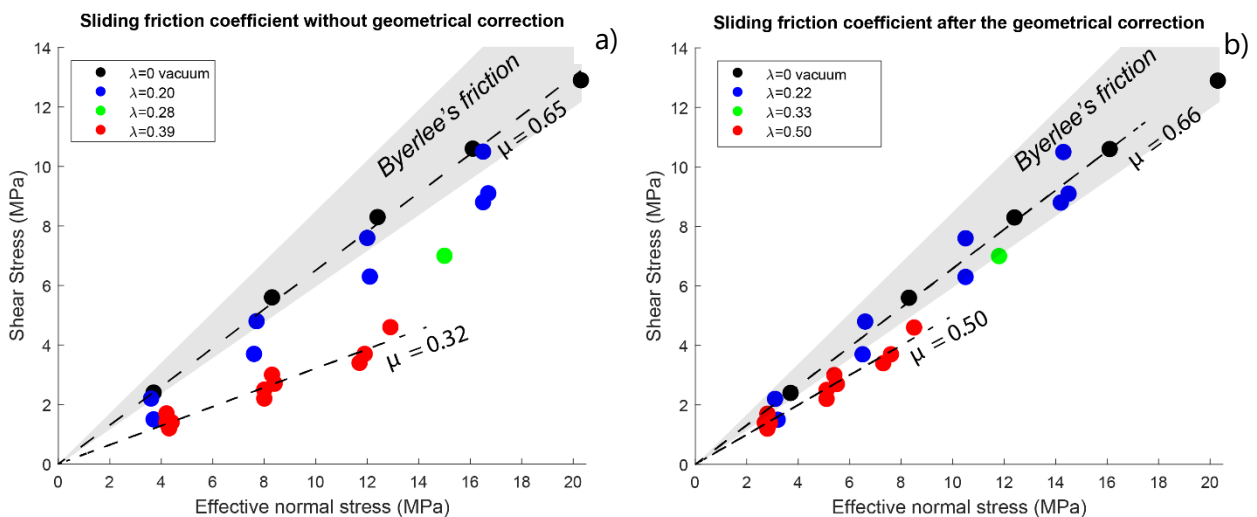
Figure S1.1. Mohr-Coulomb frictional sliding criteria of simulated basalt faults sheared under vacuum and with pressurized distilled water at different pore fluid factors λ, **(a)** before the geometrical correction and **(b)** after applying the geometrical model.

This trend seems to contradict the Mohr-Coulomb criterion for fault reactivation as the steady-state friction coefficient should not be affected by any pore fluid pressure variations at a given applied normal stress (i.e., the pore fluid factor), as indicated by:

Eq. (S1.1) $\qquad\qquad\qquad\qquad \tau = \mu\,(\sigma_n - Pf) = \mu\,(\sigma_n\,(1-\lambda))$

assuming a cohesionless fault.

Here we demonstrate using an experimentally-derived geometrical model that the frictional strength dependence with λ observed in Figure S1.1a is apparent. In fact, such relation can be attributed to the sample configuration that causes the normal stress acting on the bare surfaces to decrease to a greater extent than predicted by the effective stress law (*Terzaghi*, 1925), due to an additional mechanical effect of the fluid pressure on the void of the pair sample, as discussed below.

Geometrical model

A simple representation of the geometrical model that accounts for the additional mechanical effect of pore fluids is illustrated in Figure S1.2. When an axial load is applied on the fault, the force is completely distributed along the frictional interface A_R in absence of pressurizing fluid, resulting in:

Eq. (S1.2) $$\sigma_n = N_R/A_R = N/A_R$$

where N_R is the constraint reaction force acting on the hollow cylinder at equilibrium as a direct consequence of the axial load. N_R is characterized by the same magnitude, but opposite direction compared to N.

However, in the case the experimental fault is subjected to fluid pressurization, part of the axial load is sustained by fluid pressure acting hydrostatically in the hollow of the pair cylinders (light blue void of Figure S1.2). Therefore, the new equilibrium force equation is the following:
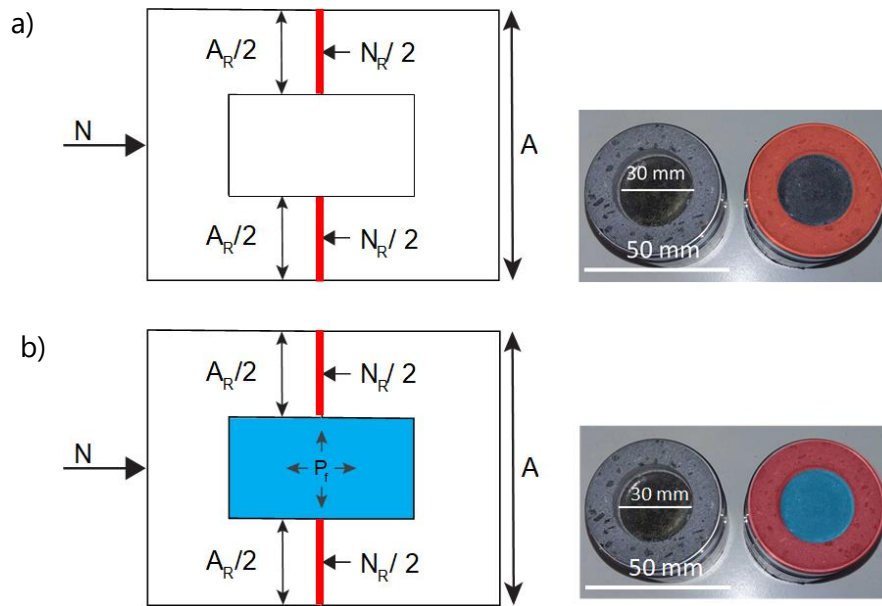
Eq. (S1.3) $$N = N_R + Pf\,(A − A_R)$$

which implies:

Eq. (S1.4) $$\sigma_n = N/A_R − Pf\,(A/A_R -1) = N/A_R − Pf\,\xi$$

where A denotes the total sectional area (Figure S1.2) and ξ the geometrical corrective factor.
This means that, during fluid pressurization, the corrected effective normal stress acting on juxtaposed hollow cylinders would amount to:

Eq. (S1.5) $$\sigma'_n = N/A_R − Pf\,\xi − Pf = N/A_R − Pf\,(\xi +1)$$

Figure S1.2. Longitudinal section of two juxtaposed hollow cylinders simulating a fault defined by rock-on-rock contacts. The picture highlights the forces acting across the frictional interface **(a)** without and **(b)** in the presence of pressurized fluids.

When the model is applied to the rotary-shear apparatus SHIVA, the ratio A/A_R amounts to 1.5625 in the configuration involving hollow cylinders 30/50 mm internal/external diameter.

Notably, after the application of the geometrical model, we observe that *i)* our friction data broadly fall close to the Byerlee's friction field, as anticipated for frictionally strong faults like basalts, with μ spanning from 0.50 to 0.66 (Figure S1.1b) and *ii)* the pore fluid factor value departs from the apparent value calculated prior to the application of the geometrical model, especially at higher fluid pressures (Figure S1.1a vs. S1.1b).

Tectonophysics

Supporting Information for

Frictional strength, stability, and healing properties of basalt-built experimental faults

by

Piercarlo Giacomel[1*], Roberta Ruggieri[1], Marco M. Scuderi[1], Elena Spagnuolo[2], Giulio Di Toro[2,3], and Cristiano Collettini[1,2]

[1] Dipartimento di Scienze della Terra, Sapienza Università di Roma, Piaz. Aldo Moro 5, Rome

[2] Istituto Nazionale di Geofisica e Vulcanologia, Via di Vigna Murata 605, Rome, Italy

[3] Dipartimento di Geoscienze, Università degli Studi di Padova, Via G. Gradenigo 6, Padua, Italy

Contents of this file

Table S2.1 and S2.2

Figures S2.1 to S2.7

Introduction

This supporting material contains two tables and seven figures.

- Table S1 List of experiments and summary of experimental conditions
- Table S2 Summary of the velocity stepping and slide-hold-slide tests
- Figure S1: Bulk-rock chemical analysis of the starting protolith
- Figure S2: Bulk XRPD analysis of the starting protolith
- Figure S3: SEM analysis of the starting protolith
- Figure S4: Volume weighted particle size distribution of the pre-tested powders
- Figure S5: Method used to work out the volumetric strain changes upon the velocity step and slide-hold-slide tests
- Figure S6: Microstructures of the deformed gouges under the optical microscope
- Figure S7: Macrostructures of the deformed bare surfaces at room-dry conditions

EXPERIMENT NAME	APPARATUS	ROCK TYPE	ENVIRONMENTAL CONDITIONS	RUN-IN (RI) SLIP (mm)	σ_n (MPa)	τ RI (MPa)	μ_{ss}	Sequence of Velocity Steps (μm/s)	Sequence of hold times (s)	Total shear strain (-)/ slip (mm)
b817	BRAVA	Simulated Gouge	Room-dry	6	5	3.14	0.63	0.1-0.3-1-3-10-30-100-300	30-100-300-1000-3000	3.8/14.1
b818	BRAVA	Simulated Gouge	Room-dry	6	10	6.17	0.62	0.1-0.3-1-3-10-30-100-300	30-100-300-1000-3000	4.3/14.2
b819	BRAVA	Simulated Gouge	Room-dry	6	20	12.54	0.63	0.1-0.3-1-3-10-30-100-300	30-100-300-1000-3000	4.3/14.1
b820	BRAVA	Simulated Gouge	Room-dry	6	30	18.78	0.63	0.1-0.3-1-3-10-30-100-300	30-100-300-1000-3000	4.2/15.1
b821	BRAVA	Simulated Gouge	Water-saturated	7	5	3.15	0.63	0.1-0.3-1-3-10-30-100-300	30-100-300-1000-3000	4.2/15.1
b822	BRAVA	Simulated Gouge	Water-saturated	7	10	6.09	0.61	0.1-0.3-1-3-10-30-100-300	30-100-300-1000-3000	4.7/15.1
b823	BRAVA	Simulated Gouge	Water-saturated	7	20	12.42	0.62	0.1-0.3-1-3-10-30-100-300	30-100-300-1000-3000	4.7/15.1
b824	BRAVA	Simulated Gouge	Water-saturated	7	30	18.69	0.62	0.1-0.3-1-3-10-30-100-300	30-100-300-1000-3000	4.5/15.1
b840	BRAVA	Bare surfaces (slabs)	Room-dry	3	5	3.78	0.76	0.1-0.3-1-3-10-30-100-300	30-100-300-1000-3000	-/10.6
b844	BRAVA	Bare surfaces (slabs)	Room-dry	3	7.5	5.83	0.78	0.1-0.3-1-3-10-30-100-300	30-100-300-1000-3000	-/10.7
b841	BRAVA	Bare surfaces (slabs)	Room-dry	3	10	7.72	0.77	0.1-0.3-1-3-10-30-100-300	30-100-300-1000-3000	-/10.6
b842	BRAVA	Bare surfaces (slabs)	Water-saturated	3	5	3.61	0.72	0.1-0.3-1-3-10-30-100-300	30-100-300-1000-3000	-/10.7
b843	BRAVA	Bare surfaces (slabs)	Water-saturated	3	10	7.44	0.74	0.1-0.3-1-3-10-30-100-300	30-100-300-1000-3000	-/10.6
s1658	SHIVA	Bare surfaces (cylinders)	Room-dry	4 - 56	3.93 - 4.21	2.27 - 2.71	0.58 - 0.64	-	120	-/56
s1624	SHIVA	Bare surfaces (cylinders)	Room-dry	4 - 56	7.92 - 7.89	5.18 - 5.44	0.65 - 0.69	-	-	-/56
s1626	SHIVA	Bare surfaces (cylinders)	Room-dry	4 - 56	7.92 - 7.83	5.06 - 5.60	0.64 - 0.72	-	120	-/56

s1657	SHIVA	Bare surfaces (cylinders)	Room-dry	4 - 56	12.25 - 12.29	8.22 - 9.08	0.67 - 0.74	-	120	-/56
s1627	SHIVA	Bare surfaces (cylinders)	Water-saturated	4 - 56	7.94 - 7.87	5.00 - 5.60	0.63 - 0.71	-	-	-/56
s1662	SHIVA	Bare surfaces (cylinders)	Water-saturated	4 - 56	3.83 - 3.63	1.97 - 2.13	0.51 - 0.59	-	120	-/56
s1633	SHIVA	Bare surfaces (cylinders)	Water-saturated	4 - 56	7.94 - 7.86	4.67 - 5.38	0.59 - 0.68	-	120	-/56
s1661	SHIVA	Bare surfaces (cylinders)	Water-saturated	4 - 56	12.10 - 12.04	7.24 - 8.64	0.60 - 0.72	-	120	-/56

Table S2.1. List of experiments and summary of experimental conditions. All experiments were sheared run-in at a sliding velocity of 10 μm/s. Acronyms and symbols: RI = "run-in" phase; σ_n = normal stress; τ = shear stress; μ_{SS} = coefficient of stable sliding friction at steady state.

EXPERIMENT NAME	Apparatus	Environmental conditions	σ_n (MPa)	(a-b) range from 1 to 300 μm/s	slip (mm)/strain (-) interval vel steps	Healing Rate, ß	slip (mm)/strain (-) interval slide-hold-slides
b817	BRAVA	room-dry	5	-0.000099 to 0.000622	7.1-10.7/1.8-2.8	0.0055	11.6-14.1/3.0-3.8
b818	BRAVA	room-dry	10	0.000076 to -0.002009	7.2-10.8/2.0-3.2	0.0063	11.7-14.2/3.5-4.3
b819	BRAVA	room-dry	20	-0.000019 to -0.000983	7.1-10.7/2.0-3.2	0.0056	11.6-14.1/3.5-4.3
b820	BRAVA	room-dry	30	0.000408 to 0.000021	8.1-11.7/2.1-3.1	0.0051	12.6-15.1/3.4-4.2
b821	BRAVA	DI-water	5	0.000254 to 0.001988	8.1-11.7/2.1-3.1	0.0091	12.6-15.1/3.4-4.2
b822	BRAVA	DI-water	10	0.000216 to -0.001368	8.1-11.7/2.3-3.5	0.0124	12.6-15.1/3.8-4.7
b823	BRAVA	DI-water	20	0.000878 to -0.000333	8.1-11.7/2.3-3.5	0.0127	12.6-15.1/3.8-4.7
b824	BRAVA	DI-water	30	0.000787 to -0.000377	8.0-11.6/2.2-3.3	0.0128	12.6-15.1/3.6-4.5
b840	BRAVA	room-dry	5	-0.007459 to 0.005931	3.6-7.2/-	0.0241	8.1-10.6/-
b841	BRAVA	room-dry	10	-0.005408 to 0.006239	3.6-7.2/-	0.0236	8.2-10.7/-
b842	BRAVA	DI-water	5	-0.01196 to 0.000691	3.5-7.1/-	0.0211	8.1-10.6/-
b843	BRAVA	DI-water	10	-0.009932 to 0.002392	3.6-7.2/-	0.0244	8.2-10.7/-
b844	BRAVA	room-dry	7.5	-0.000278 to 0.007392	3.6-7.2/-	0.0265	8.1-10.6/-

Table S2.2. Summary of the velocity stepping and slide-hold-slide tests. Acronyms and symbols: σ_n = normal stress.

Label	SiO$_2$	TiO$_2$	Al$_2$O$_3$	Fe$_2$O$_3$	MnO	MgO	CaO	Na$_2$O	K$_2$O	P$_2$O$_5$	Tot without LOI	FeO $_{perman.}$	*LOI 110 °C*	LOI 980 °C $_{perman}$	LOI Tot $_{perman}$	Tot + LOI
Etna	47.78	1.72	16.62	12.34	0.19	6.33	9.7	3.77	1.58	0.59	100.62	-	0	-0.51	-0.51	100.11
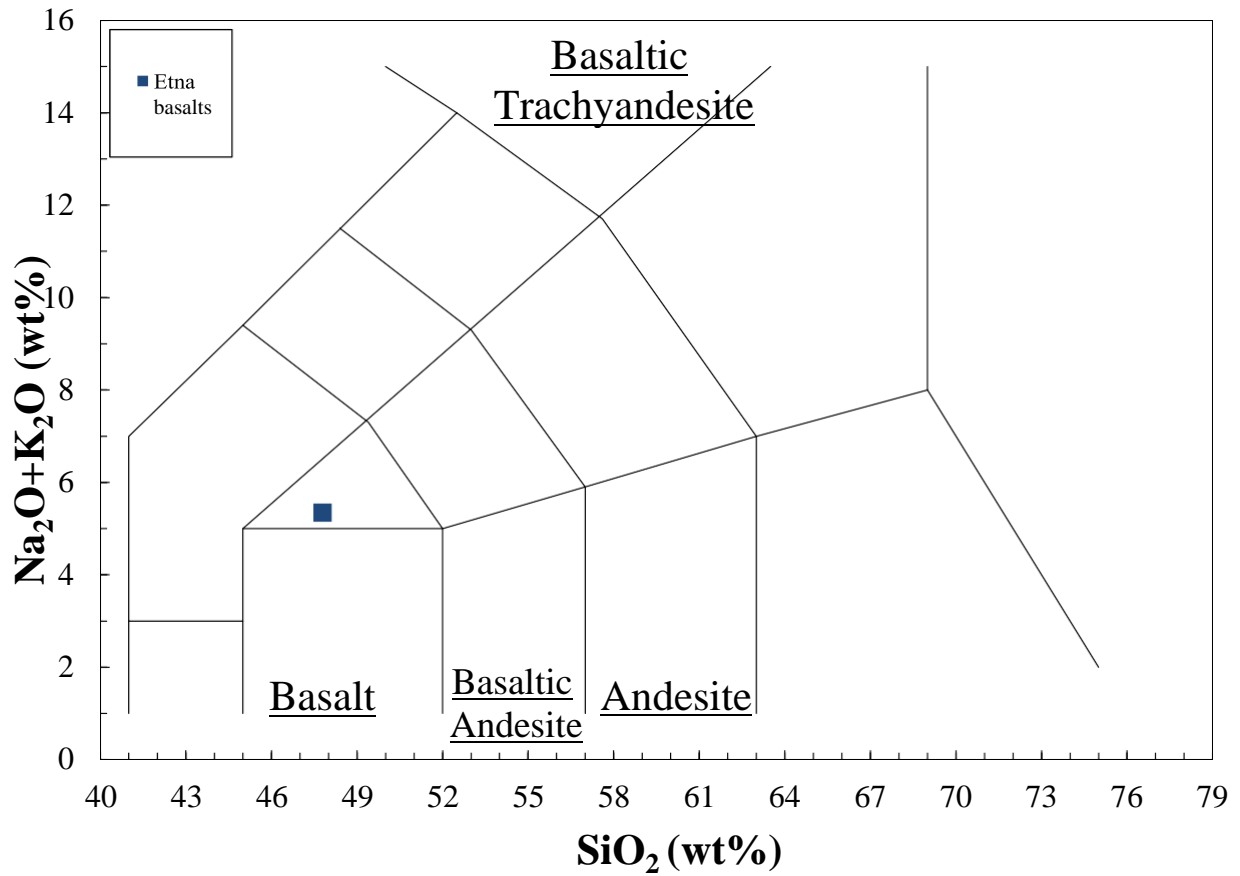
Figure S2.1. Bulk-rock chemical analysis of a representative basalt from Mount Etna employed in our tests. Below is reported the Total alkali- silica (TAS) diagram, in which the analyzed basalt lays in the field of trachybasalts.
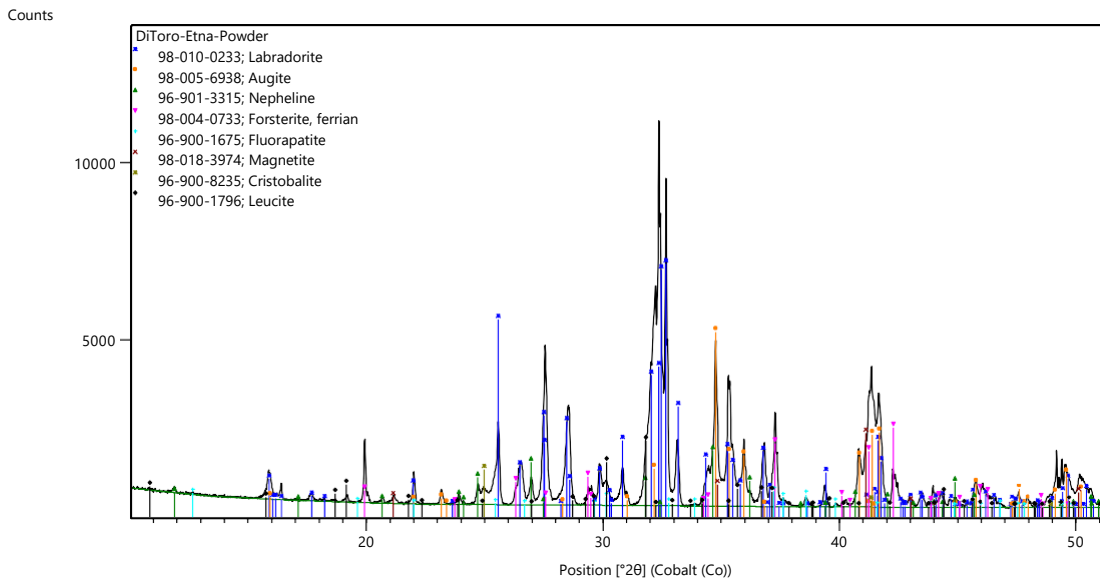
Figure S2.2. Bulk XRPD pattern of starting undeformed basalt. The primary constituents are olivine, plagioclase, augite, and magnetite.
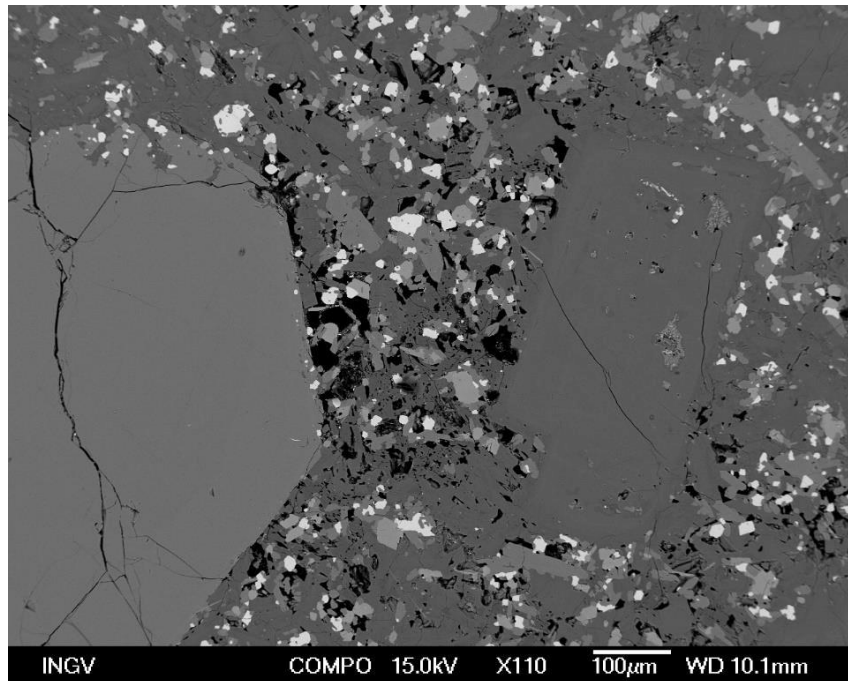
Figure S2.3. Backscatter scanning electron microscope image taken under the energy dispersive spectroscopy-equipped field emission scanning election microscope (EDS-FESEM), installed at the INGV, Rome (Italy). The image shows a portion of an undeformed basalt bare surface from Mt. Etna, belonging to the same batch of basalts employed in our tests. Specifically, the picture highlights the typical porphyric texture of these basalts, with two mm-size phenocrysts embedded in a fully crystallized micrometric groundmass.
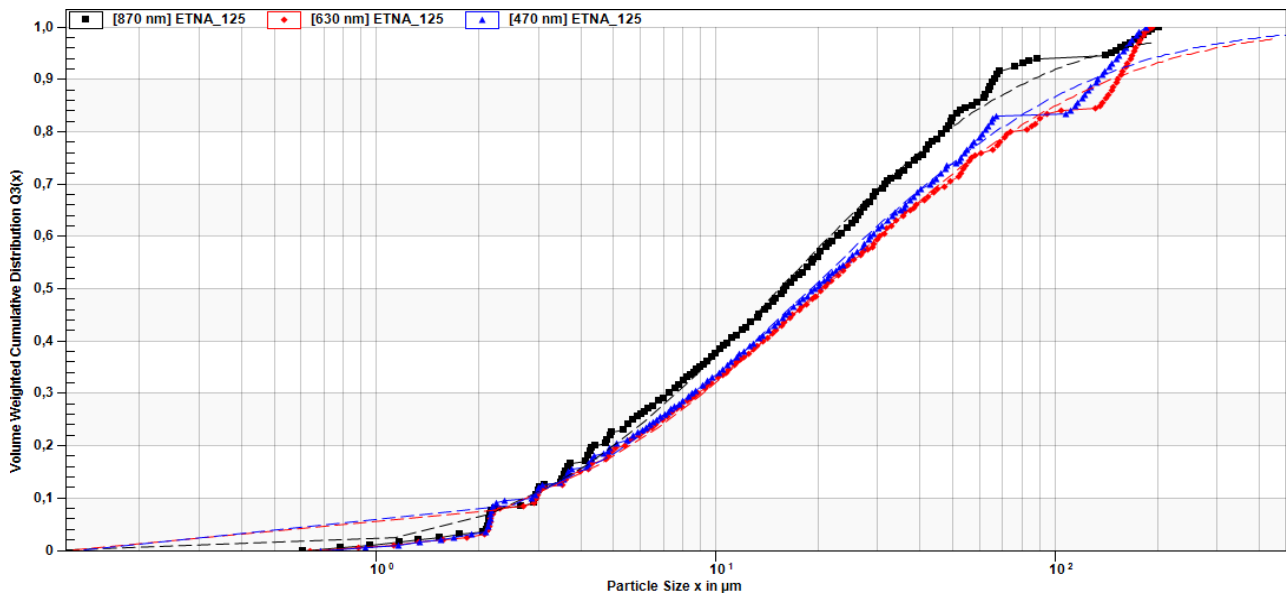
Figure S2.4. Volume weighted particle size distribution of the pre-tested Etna basalt powder. Particle sizing was obtained by multiwavelength (λ = 470, 630 and 870 nm) photo-sedimentation via a Separation Analyzer LUMiReader, installed at INGV, Rome.

a) 100-300 [μm/s]

b)

c)
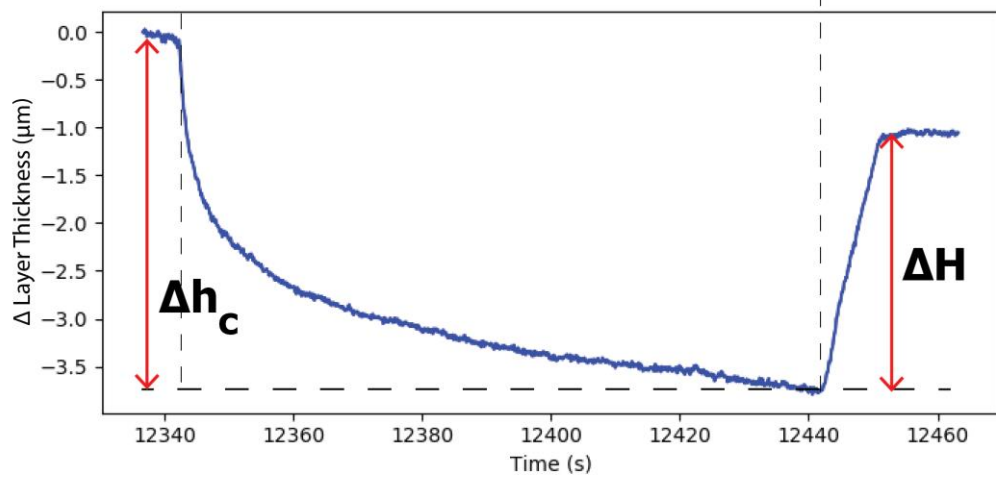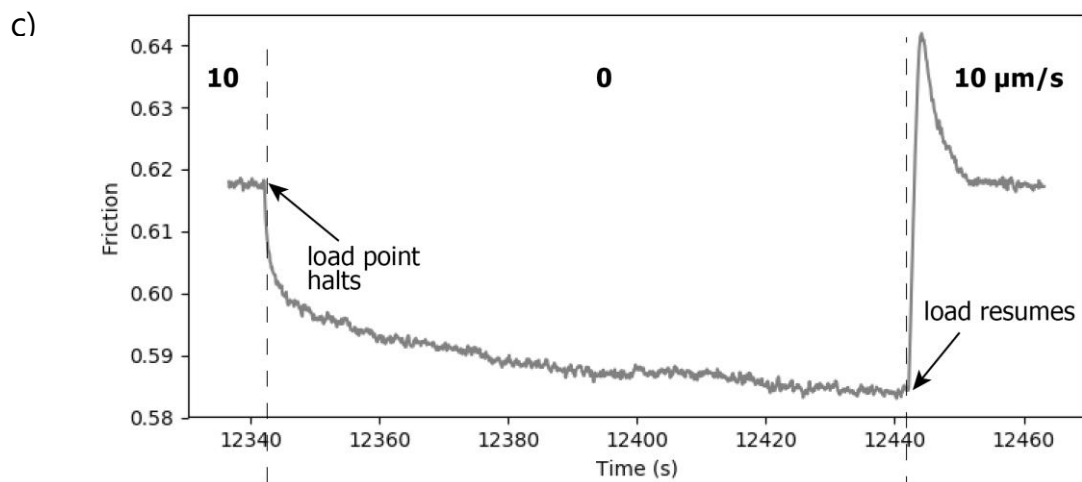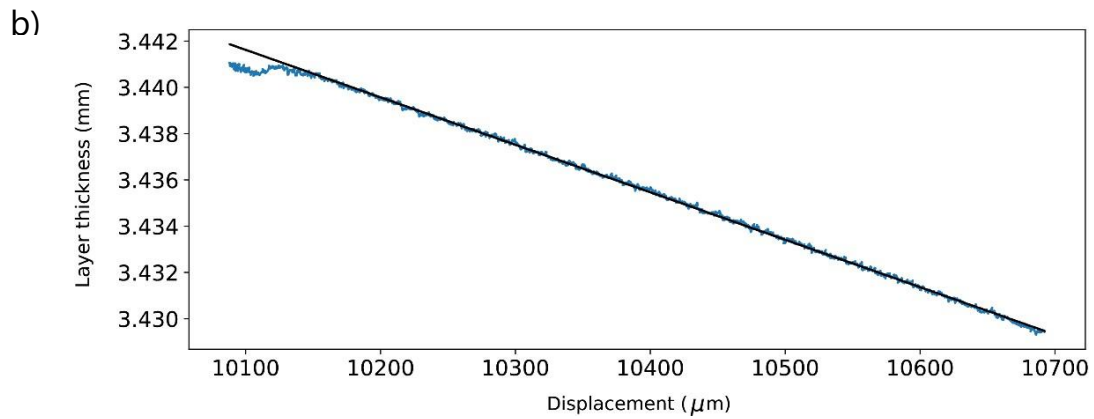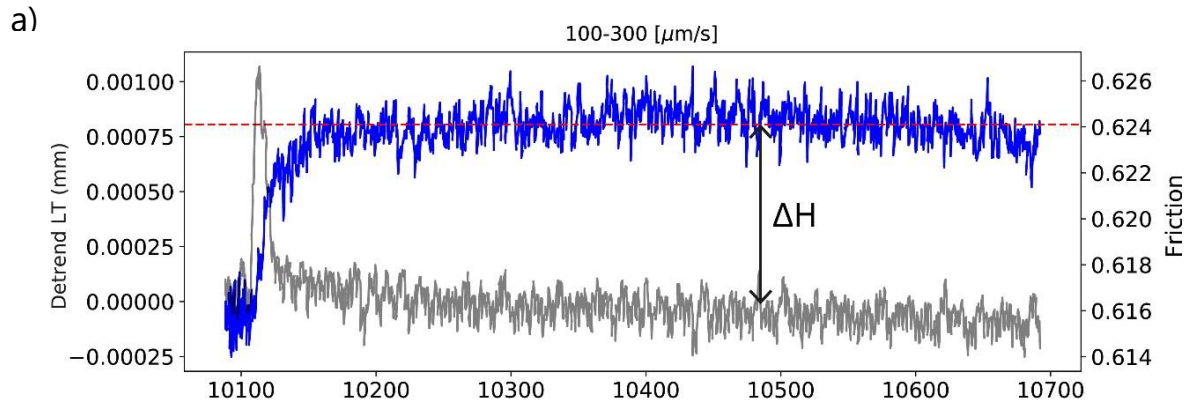
Figure S2.5. (a) Enlargement of a velocity step (gray line) and accompanying gouge layer dilation (blue line) recorded by the horizontal LVDT. The dashed red horizontal line represents the steady-state dilation upon the step increase in velocity averaged over the displacement cumulated during the velocity segment. The collection of ΔH is then plotted in Figure 6. (b) Raw layer thickness data for the analyzed velocity step depicted in Figure S5a. The black straight line is the trend originated by geometrical thinning throughout the test that is to be removed ahead of the dilation analysis. (c) Slide-hold slide test with the associated volumetric response of the gouge layer, obtained after detrending the data, following the same approach as during the velocity steps. Δh_c indicates the volumetric compaction in response to the hold phase, whereas ΔH is the dilation after loading resumes.
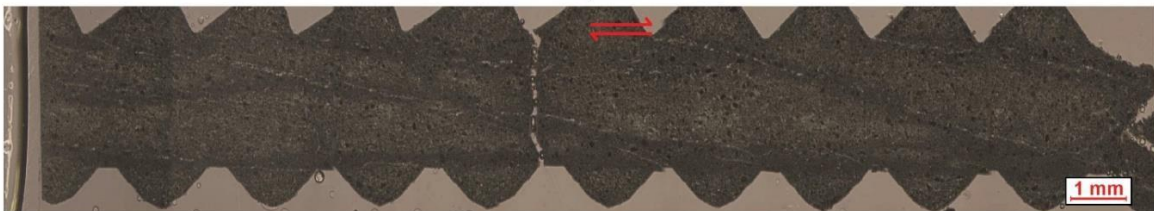
b817: σ_n = 5 MPa (dry)

b821: σ_n = 5 MPa (wet)

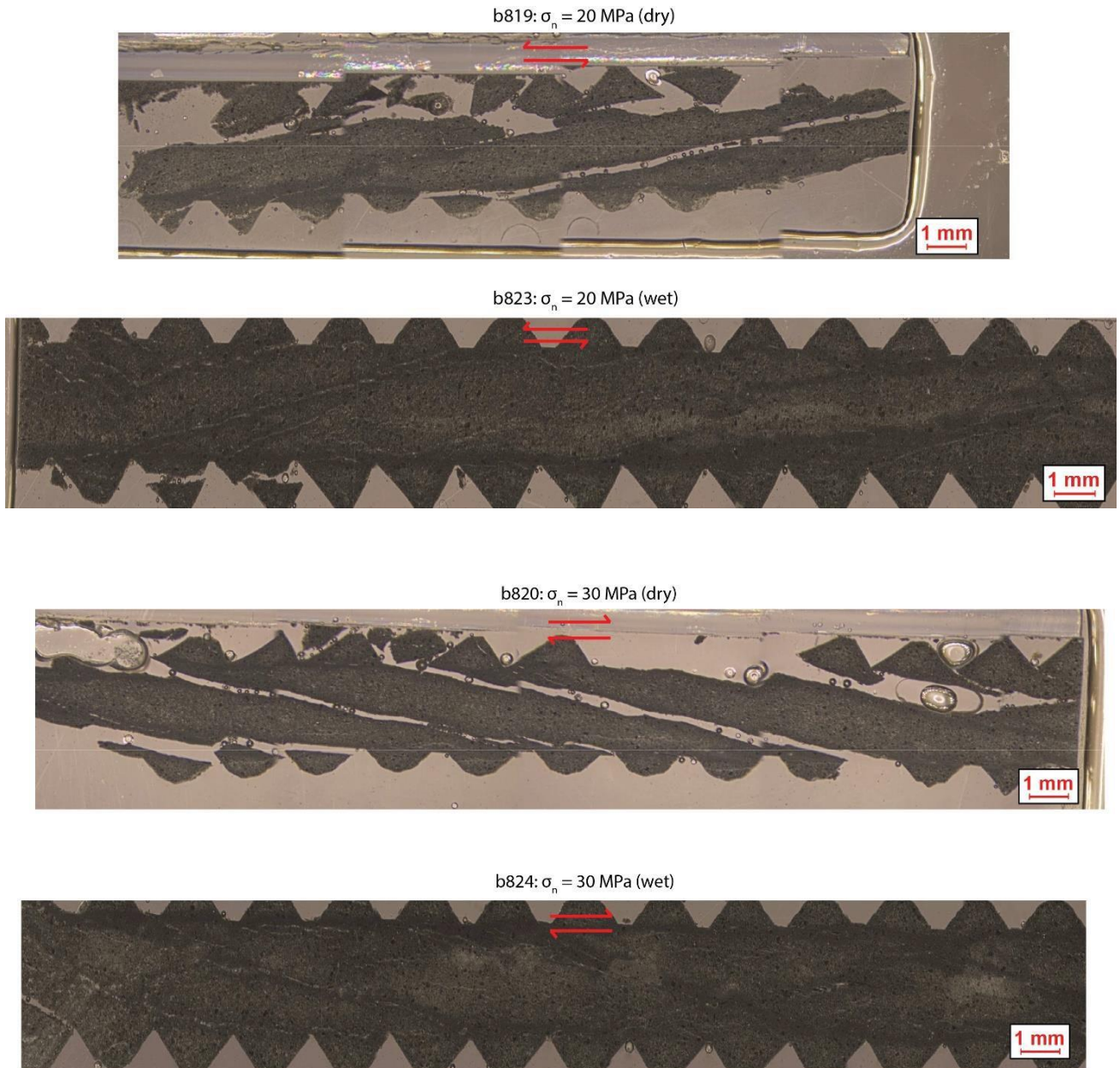b818: σ_n = 10 MPa (dry)

b822: σ_n = 10 MPa (wet)

b819: σ_n = 20 MPa (dry)

b823: σ_n = 20 MPa (wet)

b820: σ_n = 30 MPa (dry)
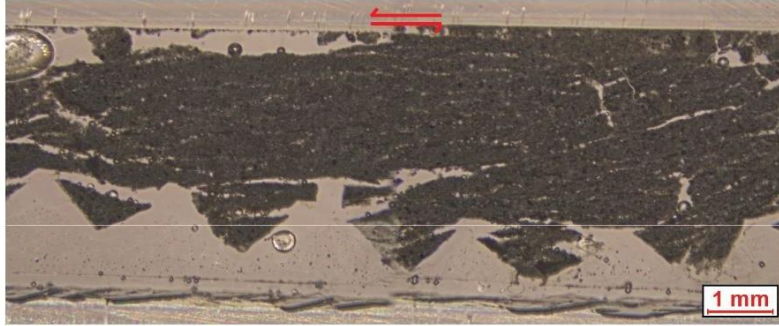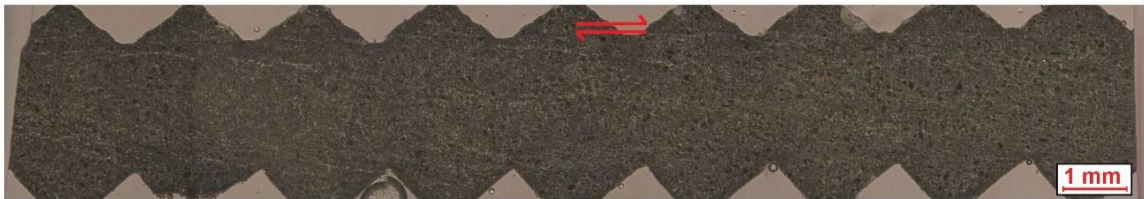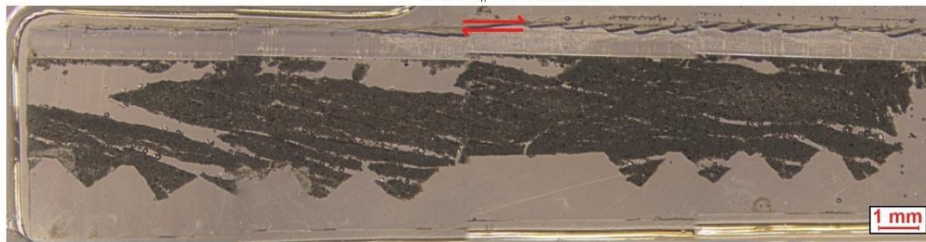
b824: σ_n = 30 MPa (wet)

Figure S2.6: Compilation of pictures taken under the optical microscope of post-tested gouge layers. The arrows indicate the direction of shear. The specimens were deformed under room-dry and water-saturated conditions at 5 to 30 MPa normal stress.

a)

ROOM-DRY

b840: 5 MPa   *b844: 7.5 MPa*   *b841: 10 MPa*

40 mm

80 mm

Increasing normal stress
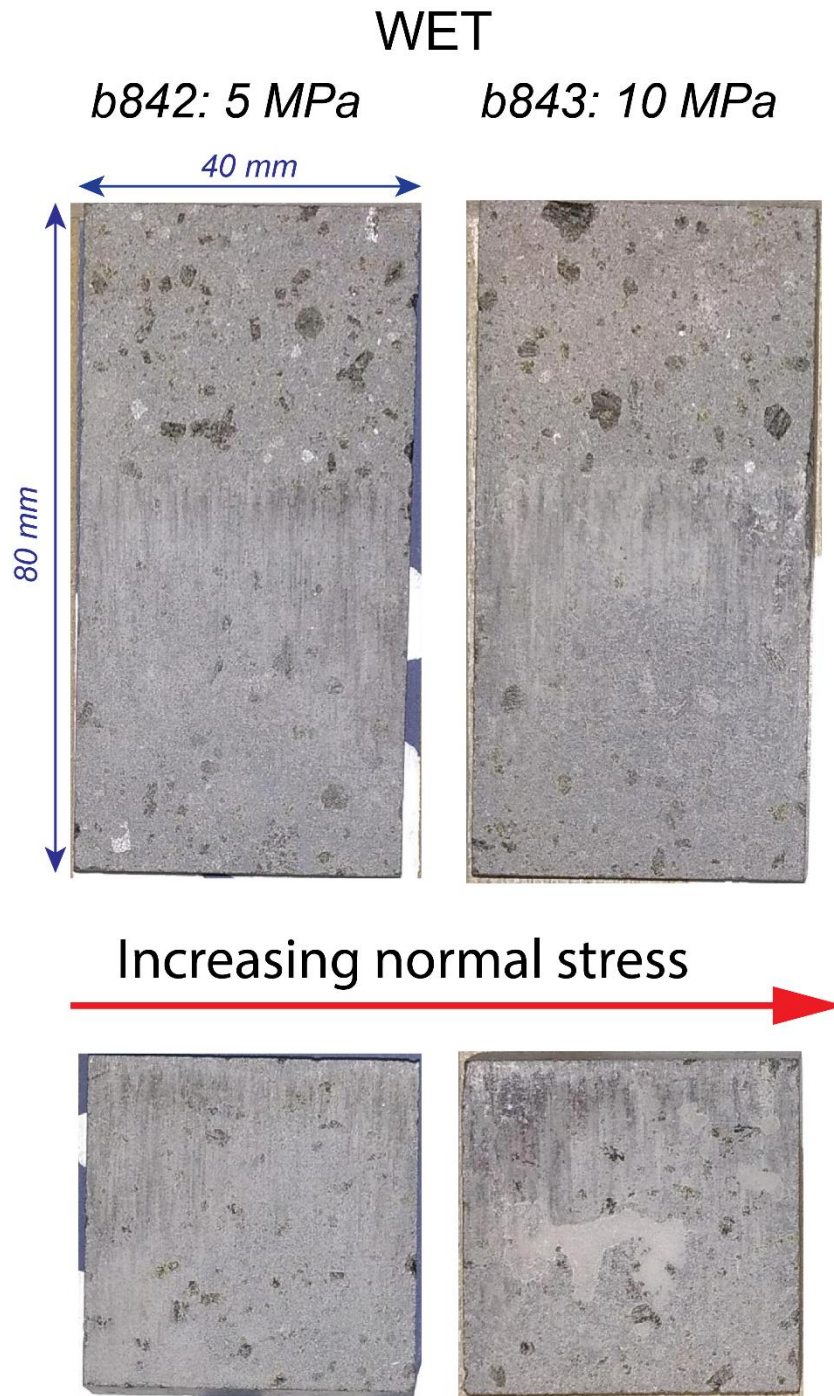
Figure S2.7. Macroscopic deformation structures from 5 to 10 MPa normal stress under (a) room-dry conditions and (b) wet conditions, testifying the increase of the amount of wear debris produced during shearing at higher normal stresses.

Frictional instabilities and carbonation of basalts triggered by injection of pressurized H₂O- and CO₂- rich fluids

Piercarlo Giacomel[1*†], Elena Spagnuolo[2], Manuela Nazzari[2,3], Andrea Marzoli[1],

François Passelegue[4], Nasrrddine Youbi[5,6] and Giulio Di Toro[1,2]

[1] Dipartimento di Geoscienze, Università degli Studi di Padova, Via G. Gradenigo 6, Padua, Italy

[2] Istituto Nazionale di Geofisica e Vulcanologia, Via di Vigna Murata 605, Rome, Italy

[3] Dipartimento di Scienze della Terra, Sapienza Università di Roma, Piaz. Aldo Moro 5, Rome, Italy

[4] EPFL ENAC IIC LEMR, GC D1 401 (Bâtiment GC), Station 18, CH-1015 Lausanne, Switzerland

[5] Geology Department, Faculty of Sciences-Semlalia, Cadi Ayyad University, Marrakech, Morocco

[6] Instituto Dom Luiz, Faculdade de Ciências, Universidade de Lisboa, 1749-016 Lisboa, Portugal.

[*]Corresponding author: Piercarlo Giacomel (piercarlo.giacomel@uniroma1.it)

[†] Now at Dipartimento di Scienze della Terra, Sapienza Università di Roma, Piaz. Aldo Moro 5, Rome, Italy

Contents of this file

Figures S3.1 to S3.6

Text S3.1

Captions for Tables S3.1 to S3.3

Additional Supporting Information

Tables S3.1 to S3.3

Introduction

This supporting material contains one text, six figures and three captions for tables. Figure S3.1 and S3.2 depict two thin sections and bulk mineralogical qualitative analysis (XRPD) of an unaltered and an altered basalt (bulk chemical XRF analysis are listed in Table S3.1). Figure S3.3 determines the threshold value that divides basalts into unaltered and hydrothermally altered. Figure S3.4 describes the pressurizing system of the rotary apparatus SHIVA and Text S3.1 thoroughly explains the different experimental configurations required to perform experiments with distilled H_2O, pure CO_2/Ar and H_2O+CO_2 mixtures. Figure S3.5 depicts the evolution of the pH with fluid pressure and temperature (post-experiment geochemical analysis of water are displayed in Table S3.3). Finally, temperature of the slipping zone during the tests was numerically modeled and displayed in Figure S3.6.
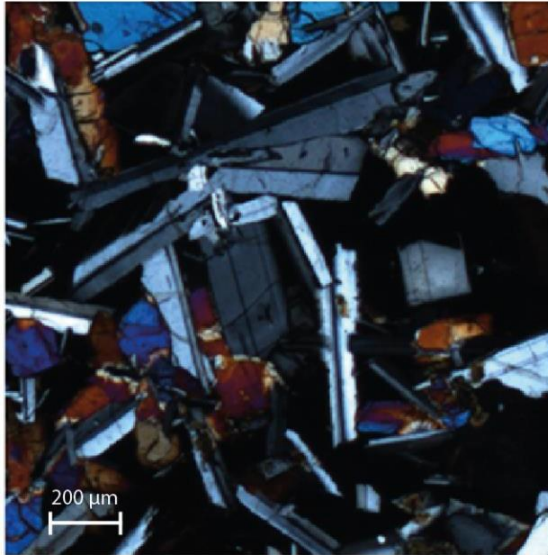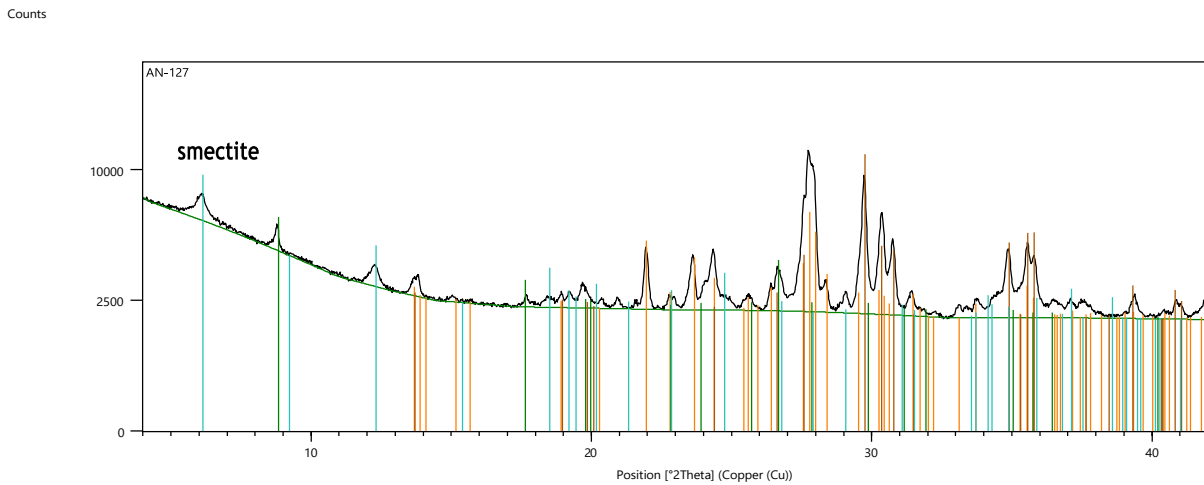
a) Unaltered basalt   b) Altered basalt: pervasive alteration
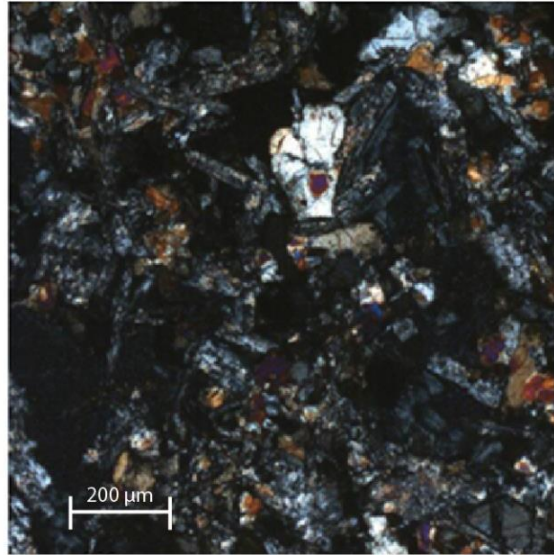
Figure S3.1. Photomicrographs of two representative basalts used in this study, under cross- polarized light. (a) Unaltered basalt with doleritic microtexture with little evidence of alteration: the amount of secondary (alteration) minerals is less than 5 % in volume; (b) doleritic basalt showing pervasive alteration (sericitization = muscovite + illite + paragonite) after plagioclase.
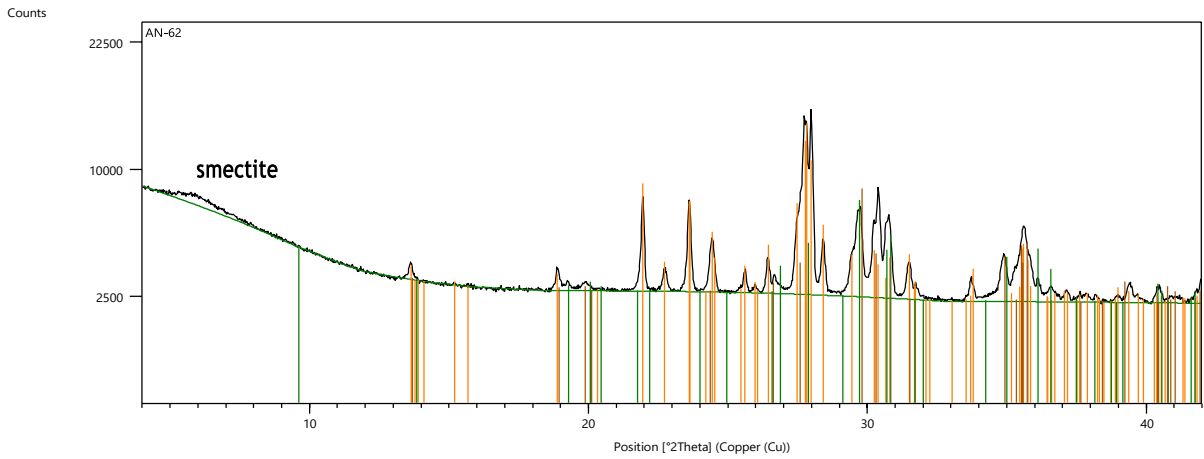
Figure S3.2. Bulk XRPD patterns of starting undeformed (a) unaltered basalt and (b) altered basalt. While primary constituents in (a) are plagioclase, augite and pigeonite, with traces of smectites, (b) contains also chlorite and illite as breakdown products of the primary minerals. The more intense smectite peak at low 2Θ reveals a greater amount of this phase in altered compared to unaltered basalts.
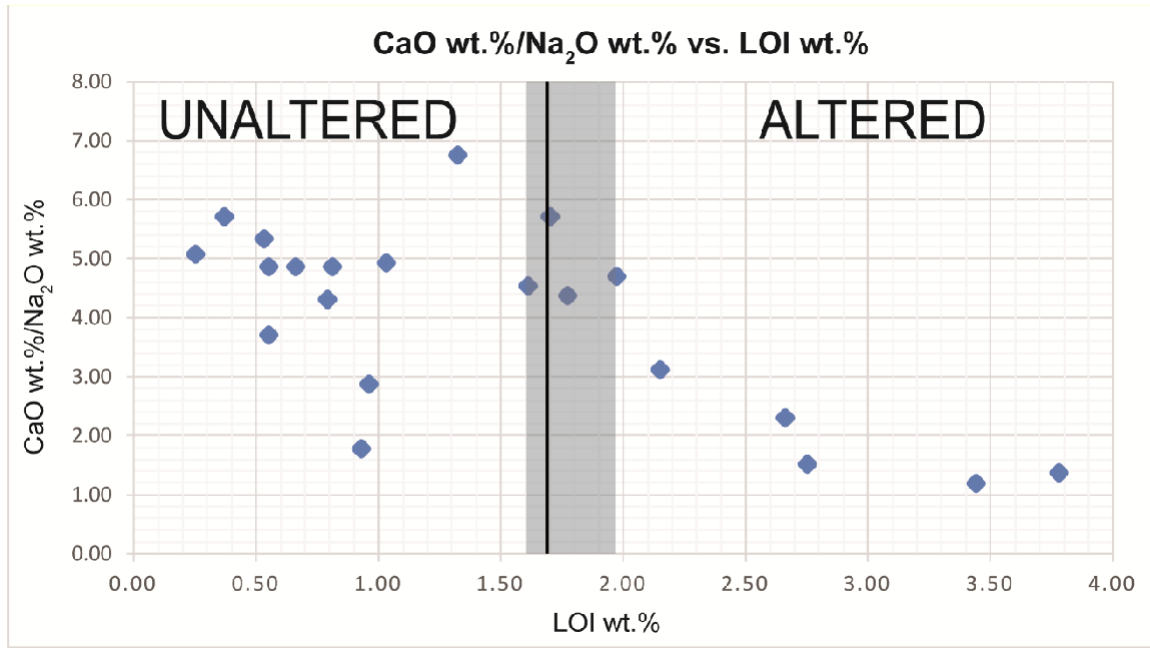
Figure S3.3. Determination of the threshold value that divides the population of basaltic rocks employed in this study into two categories: altered and unaltered. Samples with LOI higher than 1.6 – 2 wt.%, have a distinctly lower CaO/Na2O ratio compared to samples with LOI wt. < 1.6 %. Basaltic samples with LOI > 1.6 – 2 wt. % lost Ca and acquired Na as a result of chemical reactions with hydrothermal fluids. The LOI interval depicted in grey represents the transition zone that separates unaltered from altered basalts in our case study. For our purposes, within the above interval, we arbitrarily chose LOI = 1.7 wt% as a threshold value. Therefore, at LOI > 1.7 wt.% one can reasonably state that chemical analyses of the rocks evidenced clear effects of hydrothermal alteration.
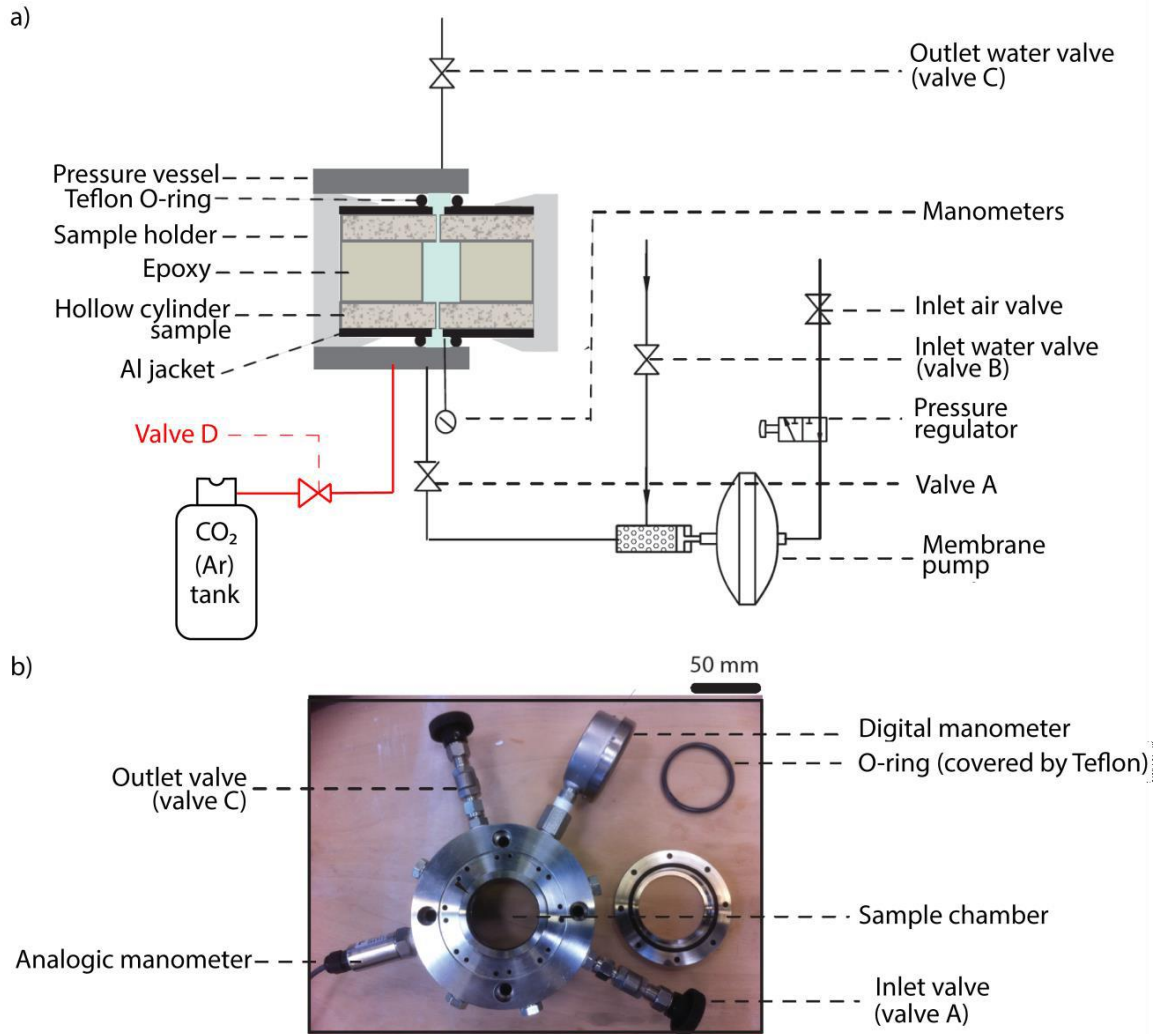
Figure S3.4. Experimental configuration a) Experimental pressurizing system, modified after Violay et al., (2013). It consists of (1) liquid fluid pressure vessel, (2) membrane pump, (3) pressure multiplier, (4) pressure regulator, (5) valves and pipes. CO_2 (Argon) tank is used during the experiments involving pure CO_2 (Argon) and H_2O+CO_2 mixtures. Valve D (red) is a pressure - reducing valve which allows CO_2 injection into the vessel at a lower pressure than the CO_2 vapor pressure in equilibrium with its liquid phase, b) Photograph of the fluid pressure vessel (*Violay et al.*, 2013).

Text S3.1. Description of the different SHIVA pressurizing configurations (Figure S3.4) employed during the tests involving injection of distilled H_2O, pure CO_2/Argon and H_2O+CO_2 fluid mixtures, respectively.

To perform experiments in the presence of fluids, *SHIVA* was equipped with a pressurizing system which comprises (1) a pore fluid pressure vessel, (2) a membrane pump with a 30 cm^3 fluid capacity, (3) a pressure multiplier that imposes a fluid pressure Pf up to 15 MPa, (4) a pressure regulator and (5) valves and pipes (*Violay et al.*, 2013). Fluid pressure experiments were performed under drained conditions to guarantee constant fluid pressure Pf throughout the tests. Experiments were conducted under the following conditions: a) water-flooded lab-faults pressurized with distilled water; b) room humidity lab-faults pressurized with pure CO_2/Argon; c) water-flooded lab-faults pressurized with

pure CO_2, (Figure S3.3), as described below. For those experiments in which bare rock fault surfaces were water-flooded (case a and c), air was removed from the fluid pressure vessel through an air bleeding system (using the manometer employed to pressurize the system with distilled H_2O).

a)   Water-flooded lab-faults pressurized with <u>distilled water</u>

A typical experiment sheared in the presence of pressurized distilled water consists in the following experimental procedure: *(1)* valves A,B,C were opened and the pressure vessel water-flooded to wet the lab-scale fault surfaces; *(2)* valve C was closed to avoid fluid leakage, whereas valve A was kept open (drained conditions) such that fluid expansion was accommodated by the movement of the membrane pump, ensuring a constant Pf value during the fluid pressure steps; *(3)* σ_n was applied to bring samples into contact and *(4)* pressurized water was injected into the pressure vessel. After the experiment, the inlet valve A was closed, the sample slowly unloaded and the water in the pressure vessel collected for chemical analysis. In this configuration, the maximum volume available for fluid injection is $\sim$ 125 cm^3, which includes the volume of the membrane pump (30 cm^3), the capacity of the pressure vessel ($\sim$5 cm^3, depending on sample permeability and the volume of epoxy filling the hollow-cylinder pair sample), and of the connection pipes;

b)   Room humidity lab-faults pressurized with <u>pure CO_2 /Argon</u>

A typical experiment sheared with pressurized pure CO_2/Argon consists in the following experimental procedure: *(1)* σ_n was applied to bring samples into contact and *(2)* valve D was opened (drained conditions) to pump pressurized fluid into the pressure vessel;

c)   Water-flooded lab-faults pressurized <u>with H_2O and CO_2 mixtures</u>

In these type of tests basalt-built fault surfaces were first wetted with distilled H_2O and then pressurized with pure CO_2, as follows: *(1)* valves A,B,C were opened and the pressure vessel water-flooded to wet the slip surfaces of the lab-scale faults; *(2)* valve A and C were closed to prevent fluid from leaking out during the tests and to keep the H2O volume constant over the experiments; *(3)* σ_n was applied to bring the samples into contact; *(4)* valve D was opened (drained conditions) to pump pressurized CO_2 into the pressure vessel) After the experiment, the sample was slowly unloaded to collect water for chemical analysis. In this configuration the maximum available volume for the fluid injection was $\sim$ 10 cm^3, depending on sample permeability and the volume of epoxy filing the hollow cylinder pair sample.

References:

Violay, M., S. Nielsen, E. Spagnuolo, D. Cinti, G. Di Toro, and G. Di Stefano (2013), Pore fluid in experimental calcite-bearing faults: Abrupt weakening and geochemical signature of co-seismic processes, *Earth Planet Sc Lett*, *361*, 74-84, doi:10.1016/j.epsl.2012.11.021.
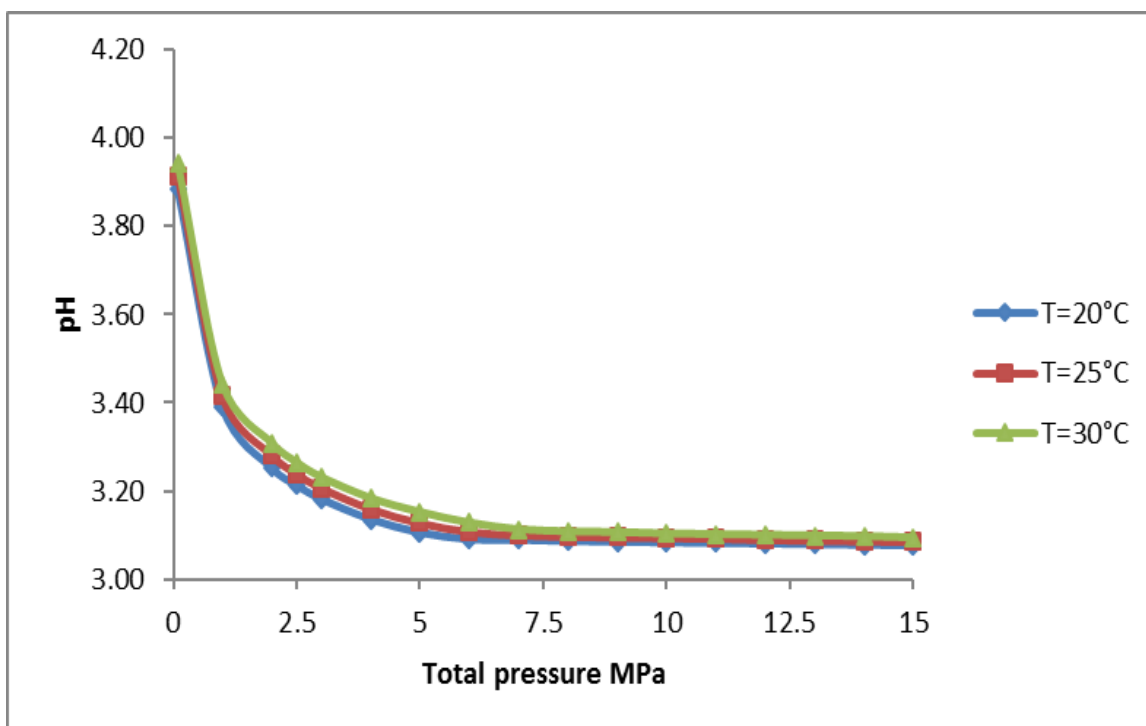
Figure S3.5. pH evolution of H_2O+CO_2 mixtures from 0.1 to 15 MPa (fluid pressure) and from 20 to 30 °C estimated starting from the solubility model of CO_2 in water reported in Diamond and Akinfiev, 2003.

References:

Diamond, L. W., & Akinfiev, N. N. (2003). Solubility of CO2 in water from− 1.5 to 100 C and from 0.1 to 100 MPa: evaluation of literature data and thermodynamic modelling. *Fluid phase equilibria*, *208*(1-2), 265-290
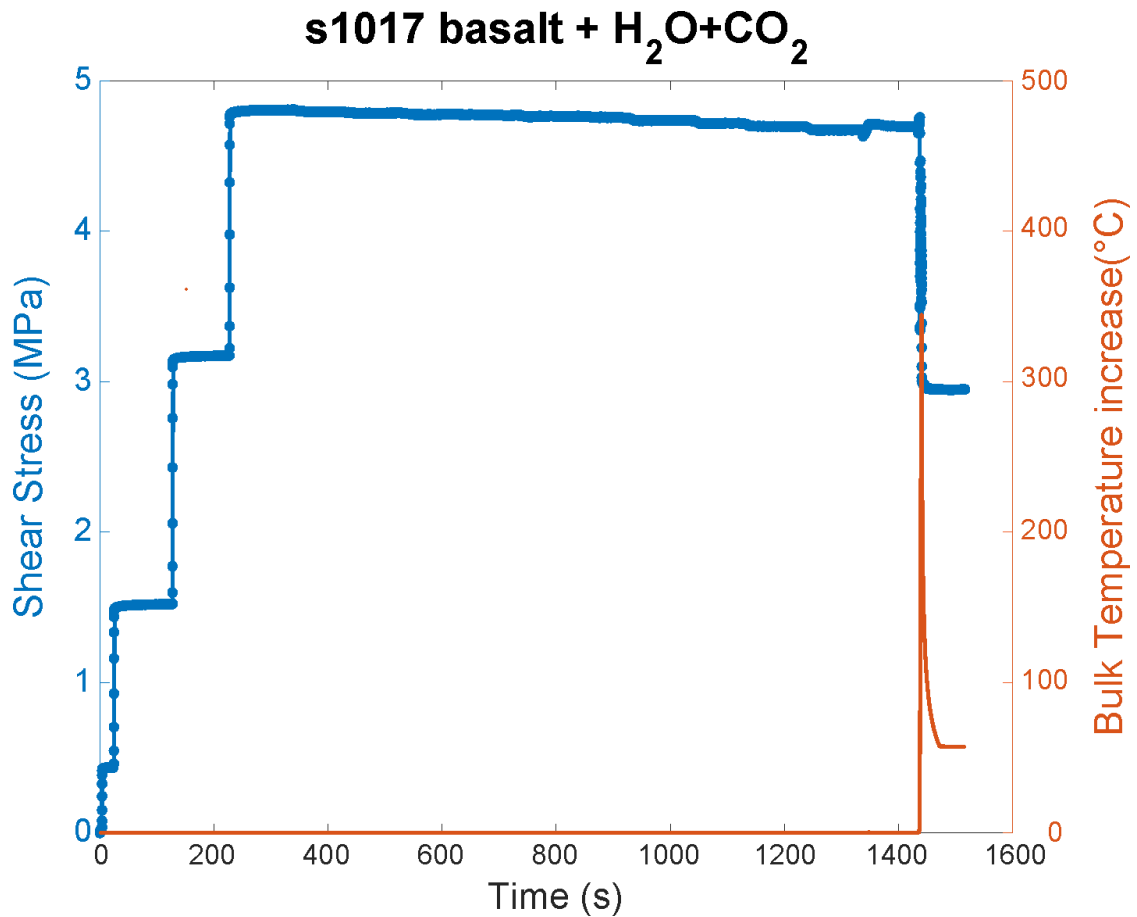
Figure S3.6. Numerical solution (Eq. A1 in Nielsen et al., (2008)) to the 1-D heat diffusion equation of Carlslaw and Jaeger (1959) to calculate the maximum temperature increase along the basaltic slip surface during the tests. This equation assumes that the total heat is converted into temperature increase, without accounting for energy dissipation as work on lab-faults, due to processes like grain comminution and crystal plasticity that buffer temperature build-up.

References:

Carslaw, H., and J. Jaeger (1959), *Heat in solids*, Clarendon Press, Oxford.

Nielsen, S., Di Toro, G., Hirose, T., & Shimamoto, T. (2008). Frictional melt and seismic slip. *Journal of Geophysical Research: Solid Earth*, *113*(B1).

Violay, M., S. Nielsen, E. Spagnuolo, D. Cinti, G. Di Toro, and G. Di Stefano (2013), Pore fluid in experimental calcite-bearing faults: Abrupt weakening and geochemical signature of co-seismic processes, *Earth Planet Sc Lett*, *361*, 74-84, doi:10.1016/j.epsl.2012.11.021.

Samples	AN 116	NEW 37	AN 127	NEW 50	AN 18	AN 310	AL 8	AL 12	HB 49	AN 174 B
Magmatic Province	CAMP	CAMP	CAMP	CAMP	CAMP	CAMP	CAMP	CAMP	CAMP	CAMP
Unit	Argana	Newark	Argana	Newark	Argana	Argana	Algarve	Algarve	Talcott	Argana
Experiment name	s1016	s1016	s1020	s1020 s1053	s1180 s1184	s1180 s1184	s1182	s1182	s1371, s1376 s1380	s1371, s1322 s1377
Major Elements concentrations (wt. %)										
SiO2	50.73	52.24	50.34	52.41	52.23	51.75	51.50	52.11	50.85	51.81
TiO2	1.30	1.13	1.34	0.93	1.19	1.22	1.13	1.08	1.13	1.36
Al2O3	13.59	14.20	13.97	13.41	14.40	14.18	14.59	14.56	13.76	13.98
Fe2O3	10.98	11.49	11.47	13.72	11.09	11.53	11.40	10.99	11.15	10.43
MnO	0.14	0.17	0.15	0.22	0.18	0.17	0.13	0.13	0.18	0.14
MgO	8.32	7.65	7.84	6.74	7.20	6.76	7.71	8.02	7.38	7.42
CaO	7.41	10.87	8.25	9.60	10.23	10.3	10.17	9.26	6.37	9.89
Na2O	3.22	2.14	2.64	2.59	2.11	2.09	2.09	2.15	4.65	2.11
K2O	1.91	0.66	1.99	0.48	0.40	0.54	0.70	0.67	0.72	0.92
P2O5	0.15	0.15	0.16	0.13	0.15	0.14	0.12	0.12	0.13	0.17
L.O.I. 1000°C	**2.66**	**0.25**	**2.15**	**0.55**	**0.55**	**1.03**	**0.66**	**0.79**	**3.78**	**1.97**
Total	100.47	100.95	100.35	100.78	99.78	99.71	100.24	99.91	100.10	100.26

Samples	AN 48	HB 1	AN 140	AN 62	NEW 70	CR 2	AN 102	AN 300	AN 118	NEW 51
Magmatic Province	CAMP	CAMP	CAMP	CAMP	CAMP	COLUMBIA RIVER	CAMP	CAMP	CAMP	CAMP
Unit	Argana	Deerlfield	Argana	Argana	Newark	/	Argana	Argana	Argana	Newark
Experiment name	s1379 s1375	s1379, s1374 s1382, s1377	s1021	s1021 s1018	s1053	s1055	s1374 s1378	s1375, s1381 s1378, s1181	s1018	s1181
Major Elements concentrations (wt. %)										
SiO_2	51.34	49.87	50.46	51.14	52.10	53.76	51.21	51.43	51.83	52.45
TiO_2	1.43	1.03	0.99	1.31	1.17	2.63	1.29	1.09	1.31	1.00
Al_2O_3	13.84	13.73	14.75	13.78	14.35	13.20	13.66	14.29	14.14	12.53
Fe_2O_3	10.51	13.67	10.97	11.44	11.56	13.97	11.35	11.51	11.43	13.93
MnO	0.11	0.30	0.18	0.20	0.21	0.18	0.17	0.18	0.16	0.22
MgO	8.38	6.50	8.11	8.13	7.63	2.58	8.21	7.40	8.09	6.20
CaO	8.93	5.78	11.80	10.80	11.13	5.87	9.18	10.34	6.88	8.64
Na_2O	1.97	4.84	1.75	1.89	1.95	3.31	2.10	1.94	4.53	3.01
K_2O	0.55	0.67	0.21	0.31	0.42	2.67	1.05	0.94	0.54	1.08
P_2O_5	0.18	0.12	0.11	0.13	0.16	0.98	0.16	0.13	0.14	0.13
L.O.I. 1000°C	**1.61**	**3.44**	**1.32**	**0.37**	**1.70**	**0.93**	**1.77**	**0.53**	**2.75**	**0.96**
Total	98.90	99.95	100.70	99.58	102.38	99.15	100.21	99.79	99.05	100.15

Table S3.1. Bulk X-Ray Fluorescence of pre-experiment basaltic powders**.**

Experiment	Basaltic couple (stat./rot.)	Magmatic province	LOI wt. % (stat./rot.)	σ_n MI (MPa)	P_f MI (MPa)	T MI (MPa)	Fluid type
s1016	AN 116 / NEW 37	CAMP	**2.66**/0.25	14.6	4.9	4.77	CO_2
s1020	AN 127 / NEW 50	CAMP	**2.15**/0.55	14.2	4.8	4.68	CO_2
s1180	AN 18 / AN 310	CAMP	0.55/**1.03**	14.6	4.9	4.68	CO_2
s1182	AL 8 / AL 12	CAMP	0.66/**0.79**	15.0	5.0	4.41	CO_2
s1371	HB 49/ AN 174 B	CAMP	**3.78**/1.97	14.6	5.0	4.52	CO_2
s1379	AN 48/ HB 1	CAMP	1.61/**3.44**	9.5	1.9	4.53	CO_2
s1021*	AN 140 / AN 62	CAMP	**1.32**/0.37	14.5	4.9	4.65	DI H_2O
s1053	NEW 70 / NEW 50	CAMP	**1.70**/0.55	15.1	5.0	4.48	DI H_2O
s1055*	CR 2 / CR 2	COLUMBIA RIVER	0.93/0.93	14.5	5.0	4.47	DI H_2O
s1374	HB 1 / AN 102	CAMP	**3.44**/1.77	14.0	4.3	4.42	DI H_2O
s1375	AN 48 / AN 300	CAMP	**1.61**/0.53	9.3	1.6	4.60	DI H_2O
s1376	HB 49 / HB 49	CAMP	3.78/3.78	9.5	1.6	4.72	DI H_2O
s1380	HB 49 / HB 49	CAMP	3.78/3.78	19.4	7.6	4.18	DI H_2O
s1381	AN 300 / AN 300	CAMP	0.53/0.53	19.4	7.5	4.66	DI H_2O
s1382	HB 1 / AN 174 B	CAMP	**3.44**/1.97	19.2	7.4	4.50	DI H_2O
s1018*	AN 118 / AN 62	CAMP	**2.75**/0.37	14.8	4.7	4.86	DI H_2O+CO_2
s1184*	AN 310 / AN 18	CAMP	**1.03**/0.55	14.4	4.9	4.68	DI H_2O+CO_2
s1377	AN 174B / HB 1	CAMP	1.97/**3.44**	9.5	1.7	4.63	DI H_2O+CO_2
s1378	AN 102 / AN 300	CAMP	**1.77**/0.53	9.5	1.8	4.53	DI H_2O+CO_2
s1181	NEW 51 / AN 300	CAMP	**0.96**/0.53	14.6	4.7	4.55	Ar

Table S2. List of Experiments, Basalt Samples, Conditions and Key Data[a]

Table S3.2. List of Experiments, Basalt Samples, Conditions and Key Data[a]

[a]Symbols: Stat./rot. denotes the stationary and the rotary side, respectively, of the rotary shear apparatus, SHIVA; LOI wt.% denotes loss on ignition in weight %; σ_n MI denotes normal stress recorded at the main instability; P_f MI denotes fluid pressure at the main instability; τ MI denotes shear stress recorded at the main instability; DI H_2O denotes distilled water. * Post experiment fluids were analyzed with the Ion-Chromatographer. In bold, the LOI of the most altered samples constituting the lab- faults, is displayed.

			Cation concentration (mg/l)										LOI wt.% at 1000°C			
		post-experiment FLUID SAMPLES											Pre - experiment			Post-experiment (BASALTIC SAMPLES)
Experiment	**Chemical composition of fluid samples**	*Volume collected (ml)*	F^-	Cl^-	Br^-	NO_3^-	SO_4^{2-}	Na^+	K^+	NH_4^+	Mg^{2+}	Ca^{2+}	max LOI wt%	min LOI wt%	**Average LOI wt%**	**Tot cumulated slip (m)**
s1018	H_2O+CO_2 mixture	22	/	1.8	< 0.01	2.3	0.64	9.9	5.8	2.4	8.7	55	2.75	0.37	1.56	0.26
s1021	distilled H_2O	18	0.15	1.1	< 0.01	2.7	2.8	3.8	3.7	4.8	2.8	33	1.32	0.37	0.85	2.30
s1055	distilled H_2O	14.5	0.14	1.6	< 0.01	0.83	6.0	7.4	4.7	0.75	3.9	59	0.93	0.93	0.93	1.00
s1184	H_2O+CO_2 mixture	13	0.28	1.6	< 0.01	0.73	3.4	4.3	2.9	5.5	12	44	1.03	0.55	0.79	0.74

Table S3.3. Chemical analysis of the post experiment water samples and comparison between cation enrichment, cumulated fault slip and loss on ignition of the starting basalts. See paragraph 4.2 for discussion.
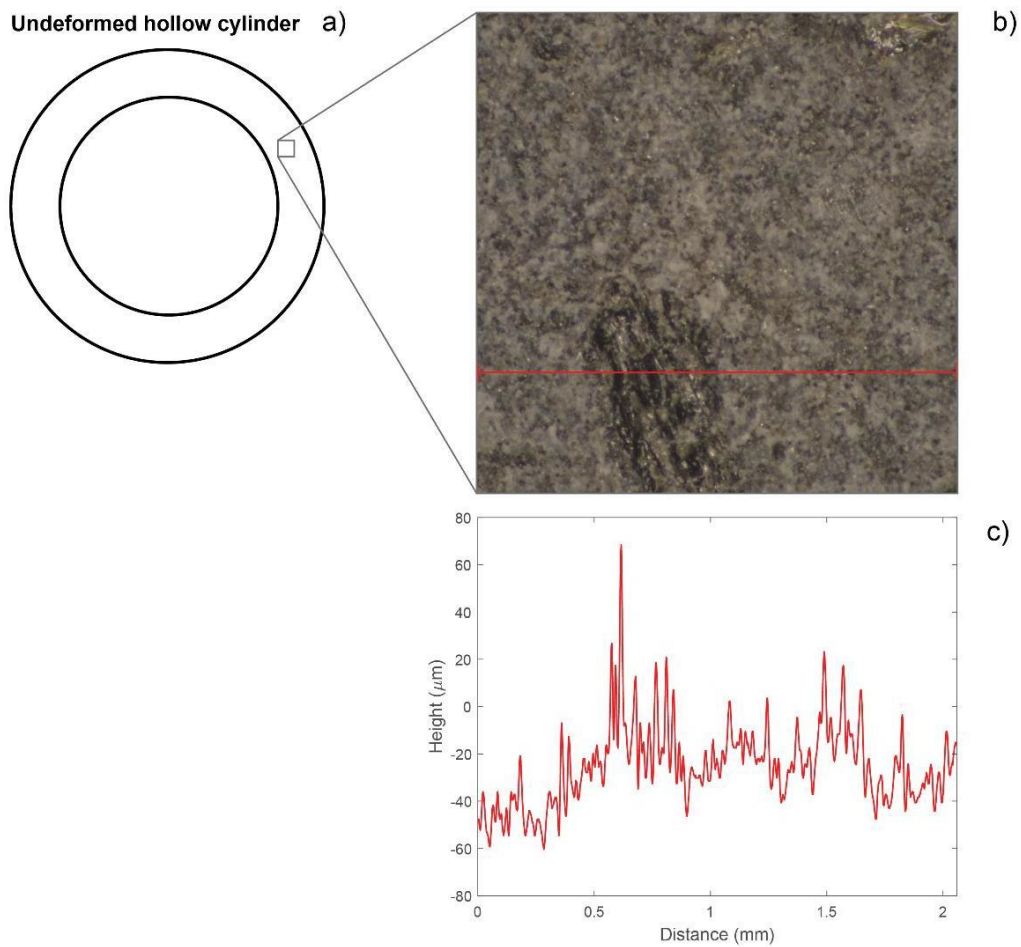
Figure S4.1: (**a**) Cartoon of the top view of a hollow cylinder from the same batch as the samples used in this study, highlighting the 2mm x 2mm patch analyzed with optical profilometer DeltaPix installed at INGV (Rome). (**b**) Optical image of the selected patch. The red line represents the trace where the analysis has been carried out. (**c**) Surface roughness profile ~ 2mm long of the selected patch from an undeformed hollow cylinder. Noteworthy is the greater roughness characterizing the basalt phenocrystals compared to the groundmass. Initial bulk surface roughness is therefore affected by the proportion between phenocrysts and matrix in the sample.